CAPITAL UNIVERSITY OF SCIENCE AND TECHNOLOGY, ISLAMABAD

Phase Modulation Detection in Radar Waveforms for Identification of Threat Signals

by

Sidra Ghayour Bhatti

A dissertation submitted in partial fulfillment for the degree of Doctor of Philosophy

in the

Faculty of Engineering
Department of Electrical Engineering

2023

Phase Modulation Detection in Radar Waveforms for Identification of Threat Signals

By

Sidra Ghayour Bhatti

(DEE193001)

Dr. Sajjad Hussain, Associate Professor

James Watt School of Engineering, Glasgow, UK

(Foreign Evaluator 1)

Dr. Waheed U. Bajwa, Professor

Rutgers School of Engineering, New Jersey, USA

(Foreign Evaluator 2)

Dr. Imtiaz Ahmad Taj

(Research Supervisor)

Dr. Noor Muhammad Khan

(Head, Department of Electrical Engineering)

Dr. Imtiaz Ahmad Taj

(Dean, Faculty of Engineering)

DEPARTMENT OF ELECTRICAL ENGINEERING

CAPITAL UNIVERSITY OF SCIENCE AND TECHNOLOGY

ISLAMABAD

2023

I would like to dedicate this dissertation to my loving parents, siblings, husband, and daughters.

CAPITAL UNIVERSITY OF SCIENCE & TECHNOLOGY
ISLAMABAD

Expressway, Kahuta Road, Zone-V, Islamabad
Phone:+92-51-111-555-666 Fax: +92-51-4486705
Email: info@cust.edu.pk Website: https://www.cust.edu.pk

CERTIFICATE OF APPROVAL

This is to certify that the research work presented in the dissertation, entitled "**Phase Modulation Detection in Radar Waveforms for Identification of Threat Signals**" was conducted under the supervision of **Dr. Imtiaz Ahmed Taj**. No part of this dissertation has been submitted anywhere else for any other degree. This dissertation is submitted to the **Department of Electrical Engineering, Capital University of Science and Technology** in partial fulfillment of the requirements for the degree of Doctor in Philosophy in the field of **Electrical Engineering.** The open defence of the dissertation was conducted on **October 19, 2023**.

Student Name : Sidra Ghayour Bhatti (DEE193001)

The Examination Committee unanimously agrees to award PhD degree in the mentioned field.

Examination Committee :

(a) External Examiner 1: Dr. Abdul Khaliq
Professor
SS-CASE IT, Islamabad

(b) External Examiner 2: Dr. Tahir Zaidi
Professor
CEME, NUST, Islamabad

(c) Internal Examiner : Dr. Noor Muhammad Khan
Professor
CUST, Islamabad

Supervisor Name : Dr. Imtiaz Ahmad Taj
Professor
CUST, Islamabad

Name of HoD : Dr. Noor Muhammad Khan
Professor
CUST, Islamabad

Name of Dean : Dr. Imtiaz Ahmad Taj
Professor
CUST, Islamabad

AUTHOR'S DECLARATION

I, **Sidra Ghayour Bhatti (Registration No. DEE193001)**, hereby state that my dissertation titled, "**Phase Modulation Detection in Radar Waveforms for Identification of Threat Signals**" is my own work and has not been submitted previously by me for taking any degree from Capital University of Science and Technology, Islamabad or anywhere else in the country/ world.

At any time, if my statement is found to be incorrect even after my graduation, the University has the right to withdraw my PhD Degree.

(Sidra Ghayour Bhatti)

Dated: 19th October, 2023

Registration No : DEE193001

PLAGIARISM UNDERTAKING

I solemnly declare that research work presented in the dissertation titled "**Phase Modulation Detection in Radar Waveforms for Identification of Threat Signals**" is solely my research work with no significant contribution from any other person. Small contribution/ help wherever taken has been duly acknowledged and that complete dissertation has been written by me.

I understand the zero-tolerance policy of the HEC and Capital University of Science and Technology towards plagiarism. Therefore, I as an author of the above titled dissertation declare that no portion of my dissertation has been plagiarized and any material used as reference is properly referred/ cited.

I undertake that if I am found guilty of any formal plagiarism in the above titled dissertation even after award of PhD Degree, the University reserves the right to withdraw/ revoke my PhD degree and that HEC and the University have the right to publish my name on the HEC/ University Website on which names of students are placed who submitted plagiarized dissertation.

(Sidra Ghayour Bhatti)

Dated: 19th October, 2023

Registration No : DEE193001

List of Publications

It is certified that following publication(s) have been made out of the research work that has been carried out for this dissertation:-

1. **S. G. Bhatti** and A. I. Bhatti, "BiLSTM Based Phase Modulation Detection of Radar Emitters," 2021 CIE International Conference on Radar (Radar), Haikou, Hainan, China, 2021, pp. 3272-3276.

2. **S. G. Bhatti** and A. I. Bhatti, "Radar signals intrapulse modulation recognition using phase-based STFT and BiLSTM", IEEE Access, vol. 10, pp. 80184–80194, 2022.

(Sidra Ghayour Bhatti)
Registration No:DEE193001

Acknowledgement

First and foremost, I want to express my gratitude to Almighty Allah, WHO gifted me with both strength and intellect. I was able to persevere through the challenging circumstances to finish my dissertation due to the patience and persistence granted to me by Allah.

It has been an honor and a privilege to work with my ex-supervisor, Dr. Aamer Iqbal Bhatti, and I want to express my deepest gratitude to him especially. I am also grateful to my supervisor, Dr. Imtiaz Ahmad Taj for his outstanding mentoring all through the process. I would like to express my sincere gratitude and warm regards to Dr. Mansoor Ahmed (Vice Chancellor, CUST) and Dr. Noor Muhammad Khan (HoD Electrical Engineering) for their assistance in facilitating the administrative aspects of this research project. I also want to convey my appreciation to the Capital University of Science and Technology (CUST), Islamabad, for providing me with the opportunity to acquire my Ph.D. degree. My wish to attend the prestigious institution has turned out to be true. My gratitude is especially directed at Engr. Khalid Mahmood (Director of Graduate Studies), for his prompt assistance and guidance. Furthermore, I would like to thank the CASPR Dynamics team. My seniors: Mr. Abrar Hashmi, Mr. Usman Zafar, Mr. Zohaib Latif, Mr. Faheem Manzoor, Ms. Aqsa Hussain, Mr. Farhan, Mr. Yasir Naeem, Mr. Azmat Saeed, Mr. Ahmad Mughal, and Mr. Faheem Gulzar deserve a special thanks for their insightful comments and ideas that helped me to clarify various concepts. Last but not least, I would like to extend my heartfelt thanks to my parents and siblings for their unwavering support and encouragement throughout my Ph.D. I owe special gratitude to my caring and supportive husband for his emotional support and encouragement during this challenging Ph.D. journey.

(Sidra Ghayour Bhatti)

Abstract

The prevalence of Low Probability of Intercept (LPI) radars in Electronic Warfare (EW) system has made the recognition of phase-coded radar waveforms crucial. LPI radar Waveform Recognition Technology (LWRT) deployed at the Radar Warning Receiver (RWR) is gaining attention as radar types diversify and the electromagnetic environment becomes more complex. The recognition of phase-coded waveforms at a low Signal-to-Noise ratio (SNR) is still challenging. This research suggests an Automatic Modulation Classification System (AMCS) to recognize LPI radar waveforms and perform feature extraction in low SNR environments. A novel phase spectrum-based feature extraction method is proposed for identifying phase-coded waveforms. The EW receiver measures the deliberately introduced phase offsets in intercepted and modulated phase-coded waveform using Short Time Fourier Transform (STFT) to identify the emitter's phase coding scheme. This research focuses on analyzing the phase spectrum of STFT, instead of the amplitude spectrum for recognition of phase-coded signals. Selecting the optimal window size for STFT is critical to preserve phase offset of each sub-pulse within the phase-coded signal. The STFT is computed window-wise as it moves along the entire signal duration, providing outputs with computed phase values. The research utilizes 1D phase-based feature extraction by selecting the maximum window output and recording its phase-value for a feature vector. For 2D phase-based extraction, phase values are directly computed from the window output and stacked horizontally to form a feature matrix. The research proposes two architectures for AMCS: Bidirectional Long Short Term Memory (BiLSTM) and Deep Convolution Neural Network (DCNN). A BiLSTM network learns bidirectional, long-term relationships between time steps in a time sequence, and mostly outperforms the other Recurrent Neural Networks (RNNs) used to handle sequential data. A BiLSTM network with 1D phase-based feature vectors has achieved about 70% recognition accuracy at -8 dB SNR. The other architecture uses a DCNN with 2D phase-based features, achieving 89% recognition at -16 dB SNR. DCNNs perform well for image classification due to their ability to automatically

learn hierarchical features, exploit local correlations, and achieve translation invariance. Both approaches compete well with existing methods, requiring minimal pre-processing and offering efficient online recognition of phase-coded waveforms. The newly proposed feature extraction method has outperformed other techniques, demonstrating high recognition accuracies for phase-coded waveforms at low SNR situations. Additionally, it is found that Barker codes, even at low SNR levels, have acceptable recognition accuracy when utilizing both approaches; yet, they are rarely discussed in the literature.

Contents

List of Figures

List of Tables

Abbreviations

ARM	Anti-Radiation Missile
AWGN	Additive White Gaussian Noise
ABC	Artificial Bee Colony
ANN	Artificial Neural Network
BMD	Ballistic Missile Defense
BFSK	Binary Phase Shift Keying
BPPT	Back Propagation Through Time
BRNN	Bidirectional Recurrent Neural Network
BiLSTM	Bidirectional Long Short Term Memory
CPP	Cycle Per Phase
CD	Chromatic Dispersion
CWR	Continuous Wave Radar
CWFMR	Continuous Wave Frequency Modulated Radar
CWD	Choi William Distribution
CNN	Convolutional Neural Network
CWT	Continuous Wavelet Transform
DCNN	Deep Convolutional Neural Network
DOA	Direction of Arrival
DRSN	Deep Residual Shrinkage Network
DNN	Deep Neural Network
EW	Electronic Warfare
ESM	Electromagnetic Support Measures
ECM	Electromagnetic Countermeasures

ECCM	Electromagnetic Counter-Countermeasures
ES	Electronic Support
EA	Electronic Assault
EP	Electronic Protection
ERP	Effective Radiated Power
ELINT	Electronic Intelligent
EMD	Empirical Mode Decomposition
FrFT	Fractional Fourier Transform
FSST	Fourier based Synchrosqueezing Transform
FMCWR	Frequency Modulated Continuous Wave Radar
FFNN	Feed Forward Neural Network
GRU	Gated Recurrent Unit
HHT	Hilbert Haung Transform
IF	Intermediate Frequency
LSTM	Long Short Term Memory
LPI	Low Probability of Intercept
MFIJD	Multiple Feature Image Joint Decision
NLP	Natural Language Processing
OTH	Over the Horizon
OF	Optical Fiber
PRF	Pulse Repetition Frequency
PW	Pulse Width
PA	Pulse Amplitude
QFSK	Quadrature Phase Shift Keying
RADAR	RAdio Detection And Ranging
RF	Radio Frequency
RER	Radar Emitter Recognition
RWRs	Radar Warning Receivers
RDBN	Reinforced Deep Belief Network
RNN	Recurrent Neural Network
RA	Reassignment Method

RWR	Radar Warning Receiver
SVM	Support Vector Machine
STFT	Short Time Fourier Transform
SEI	Specific Emitter Identification
SAT	Sample Averaging Technique
SST	Synchrosqueezing Transform
SPWVD	Smooth Pseudo Wigner Ville Distribution
ST	Stockwell Transform
TFR	Time Frequency Representation
TWT	Traveling Wave Tubes
TOA	Time Of Arrival
TBPPT	Truncated Back Propagation Through Time
TDWR	Terminal Doppler Weather Radar
UCWR	Unmodulated Continuous Wave Radar
WVD	Wigner Ville Distribution
WT	Wavelet Transform

Symbols

σ	Sigmoid activation function
x_t	Current input at time (t)
h_t	Recurrent information at time (t)
y_t	Cell output at time (t)
h_{t-1}	Past recurrent information at time (t − 1)
f_t	Output of Forget gate at time (t)
W_f	Forget gate weights
b_f	Forget gate bias
i_t	Output of Input gate at time (t)
W_i	Input gate weights
b_i	Input gate bias
W_c	Cell state weights
b_c	Cell state bias
$\tilde{C}_t$	Update to cell state at time (t)
C_t	Cell state at time (t)
C_{t-1}	Cell state at time (t − 1)
o_t	Output of output gate at time (t)
W_o	Output gate weights
b_o	Output gate bias
h_t^f	Forward activations
h_t^b	Backward activations
R_t	R^{th} Convolutional kernel
$bias_R$	R^{th} Convolutional kernel bias

Out	Output of Output layer (OL)
h_{FL}	Input to the FC_1
h_{FC}	Output of FC_1
W_{FC}	Weight matrix between the FC_1 and FC_2
b_{Out}	Bias of OL
W_{Out}	Weights between FC_2 and OL
$\hat{y_p}$	Predicted probability of class p
$\hat{y}$	Vector of predicted probabilities of output classes
J	Cross entropy loss function

Chapter 1

Introduction

1.1 Background and Motivation

The term "RADAR" stands for RAdio Detection And Ranging. It is an electromagnetic device used to identify, detect, and track the targets at long distances. It works by sending electromagnetic radiation in the direction of targets and listens for the echoes that are reflected back. The targets may be automobiles, spacecraft, aircraft, ships, or even insects, birds, and rain. In addition to their size and shape, radar can determine the existence, range, and velocity of such objects. The capability of radar to identify distant objects in bad weather and precisely calculating their range, distinguishes it from optical and infrared sensing technologies. It often uses frequencies in the range of 400 MHz to 40 GHz [1].

Due to military demands, radars developed rapidly in the 1930s and 1940s. Additionally, radar has been used in several important civilian applications including planetary observation, space surveillance, air traffic control, weather monitoring, remote sensing, ship and aircraft navigation, etc. Modern radars work in collaboration with machine learning algorithms and are able to find out useful information in the presence of high noise levels. Initially, radar was developed as a device to warn about approaching hostile aircraft and to direct the weapons toward the

hostile target. The well-designed modern radar systems are capable of extracting more information about the target other than the range.

1.2 History of Radar

Scientist Nikola Tesla discovered in 1900 that when sound waves are produced, echoes can be observed [2]. Electromagnetic waves return in a similar manner as sound waves, the distance and velocity of an object can be estimated with their help. Heinrich Hertz conducted some experiments in the late 19^{th} century, and the findings showed that radio waves are reflected back from metallic objects [3]. After that, the systems based on the principle of electromagnetism began to emerge. German inventor Hulsmever was the first to apply electromagnetic principles to create a detection gadget that ships use to avoid collisions during foggy weather [4].

Sir Robert Watson, a British physicist, created the first radar device in 1935. By the end of 1939, England had established a network of radar stations to protect its coastline from any potential aerial attackers. Radars were also utilized in ships and planes during WW2. Japan was unable to successfully employ radar technology, which Germany had been using since 1940 [5].

John Randall and Harry Boot created the resonant cavity magnetron in 1940, which could produce radio pulses with a high frequency and high strength [6]. Lasers of extremely short wavelengths were used to operate this cavity. Radar systems were extensively employed in several fields after WW2, including navigation, guidance systems, meteorology, and others. Traveling Wave Tubes (TWT), which finally gave rise to phased array radars, were the main advancement after the post-war era. The development of entirely digital phased-array radars was spurred by developments in digital technology throughout the first decade of the twenty-first century. In the millimeter-wave region of the spectrum (usually 94 GHz), high-power transmitters with average powers 100–1,000 times greater than before became accessible for radar applications. With continued development of

electronics, systems with pulse durations measured in picoseconds became possible.

1.3 Fundamentals of Radar

A narrow electromagnetic energy beam is often sent into space from an antenna of radar. The focused antenna beam scans the desired area. When the beam hits a target, some of the energy is reflected back toward the radar system and a portion of it is intercepted. A single antenna is mostly used for both transmitting and receiving on a time-shared basis because the majority of radar systems don't transmit and receive at the same time. The desired reflected signals are extracted by a receiver connected to the antenna's output element, while the undesired signals are discarded. The echo from an aircraft, for instance, might be a signal of interest. The detection of the intended echo from the aircraft may be masked and interfered with the signals that are not of interest, such as rain or echoes from the ground. The unwanted reflections, or clutter, don't affect human sight the way they do radar sometimes. Radio Frequency (RF) energy is reflected by mountains, trees, houses, rain, birds, and chaff. The basic function of radar is shown in Fig. 1.1.

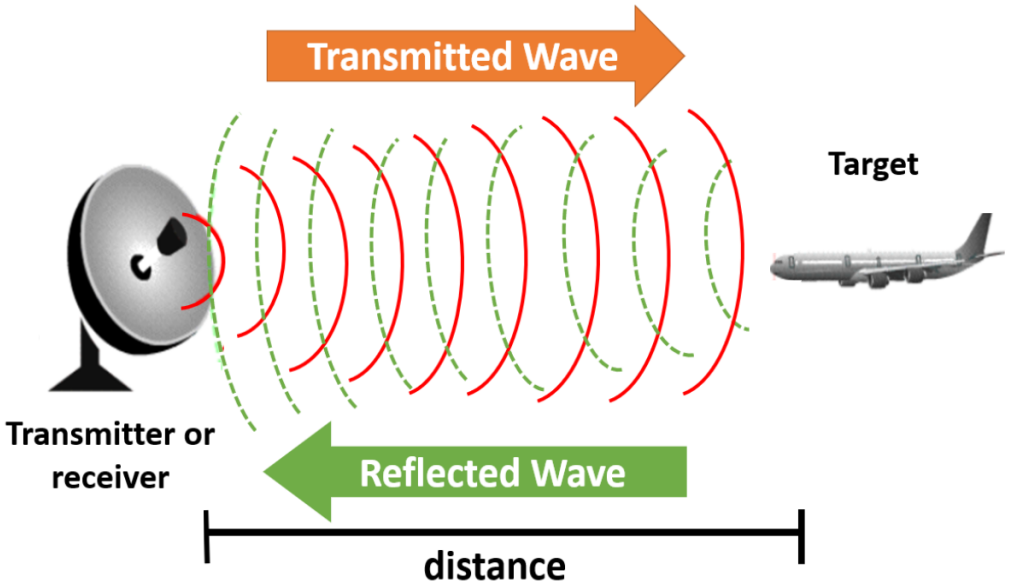

FIGURE 1.1: Basic Function of Radar System

Target discriminants as shown in Fig. 1.2 are used by radar systems to separate the desired target from the clutter. The range, velocity, and angle are the target discriminants. The range is calculated as the total time for the radar signal to travel from the source to the destination and back. The angular direction of a target is determined using the antenna's orientation at the time the echo signal is received. By determining the target's location at successive time intervals, the recent track of the target may be determined. A moving target shifts the frequency of the reflected signal by a specific amount known as the Doppler shift.

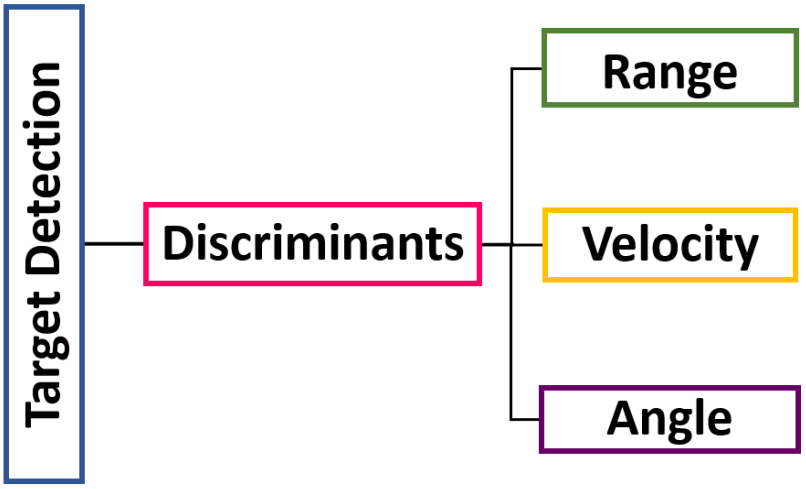

FIGURE 1.2: Radar Target Discriminants

1.4 Basic Components of Pulse Radar

Pulse radar transmits and receives signals through a single antenna by using a duplexer. Fig. 1.3 depicts the block diagram of a pulse radar. The blocks in blue represent the transmit path and green blocks show the path followed by the received signal. The functionality of each block of pulse radar is given below:

1.4.1 Antenna

The function of the antenna is to radiate energy in space. Antennas mainly used in radar systems include planar arrays, phased arrays that are steered electronically,

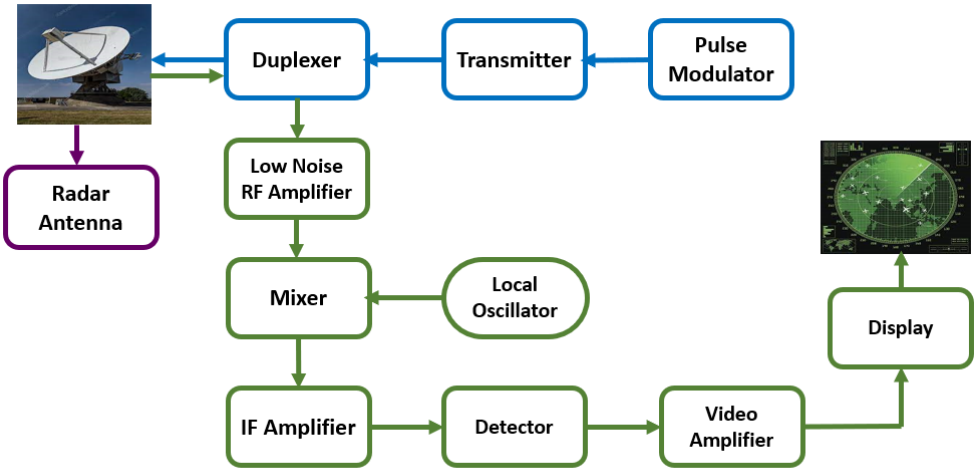

FIGURE 1.3: Basic Components of Pulse Radar

or parabolic reflectors. A horn antenna or other tiny antenna is placed at the parabola's focus in order to shine light onto the reflector's parabolic surface. The electromagnetic energy is reflected by this surface and then emitted as a confined beam.

1.4.2 Pulse Modulator

For radar activities, such as target identification, range, and tracking, the pulse modulator determines the pulse duration, pulse repetition frequency, and other parameters of the transmitted pulses.

1.4.3 Transmitter

A transmitter is built using semiconductors or vacuum tubes. It sends out the pulse-modulated signal, which consists of a series of repeated pulses. In addition to having the wide bandwidth and high power that are typical of radar applications, the transmitter of a radar system must also be effective, dependable, not too huge in size and weight, and simple to maintain. The transmitter must normally create low-noise, continuous transmissions to prevent interference signals from the

transmitter obscuring the detection of the slight Doppler frequency shift caused by weak moving objects.

1.4.4 Duplexer

An antenna is connected alternatively to the transmitter and receiving sections by a microwave switch called a duplexer. The pulse-modulated signal is sent by the antenna when it is connected to the transmitter by the duplexer. Similarly, when the antenna and low-noise Radio Frequency (RF) amplifier are connected by a duplexer, the signal picked up by the antenna is delivered to the amplifier.

1.4.5 Low Noise RF Amplifier

This device boosts the weak RF signal that the antenna receives. The amplifier's output is also linked to the mixer.

1.4.6 Local Oscillator

It generates a stable frequency signal. The mixer is connected to the local oscillator's output.

1.4.7 Mixer

The mixer can generate both the difference and sum of the applied frequencies. The variation in frequencies among them will be of the Intermediate Frequency (IF) type.

1.4.8 IF Amplifier

It amplifies the IF signal. The output Signal to Noise Ratio (SNR) is enhanced. It also determines the gain and effective bandwidth of the receiver. The IF amplifier's

job is to increase the weak signal's strength and SNR so that it can be processed and demodulated further, which will improve the receiver's overall performance.

1.4.9 Detector

It demodulates the signal that was collected from the IF amplifier's output.

1.4.10 Video Amplifier

This device amplifies the visual signal that the detector produces at its output.

1.4.11 Display

The amplified video signal is often displayed on a screen.

1.5 Types of Radar

Depending on their functionality and the types of signals they can operate with, radars can be categorized into the following categories:

1.5.1 Waveform Based Classification

Radars can be categorized according to the waveforms that they employ. Following is a list of some of the waveform-based categories:

1.5.1.1 Pulse Radar

A sequence of short, repeating pulses makes up the most prevalent kind of radar signal. Fig. 1.4 depicts a basic description of a sine-wave pulse that could be produced by a medium-range radar transmitter used for aircraft detection. The sine

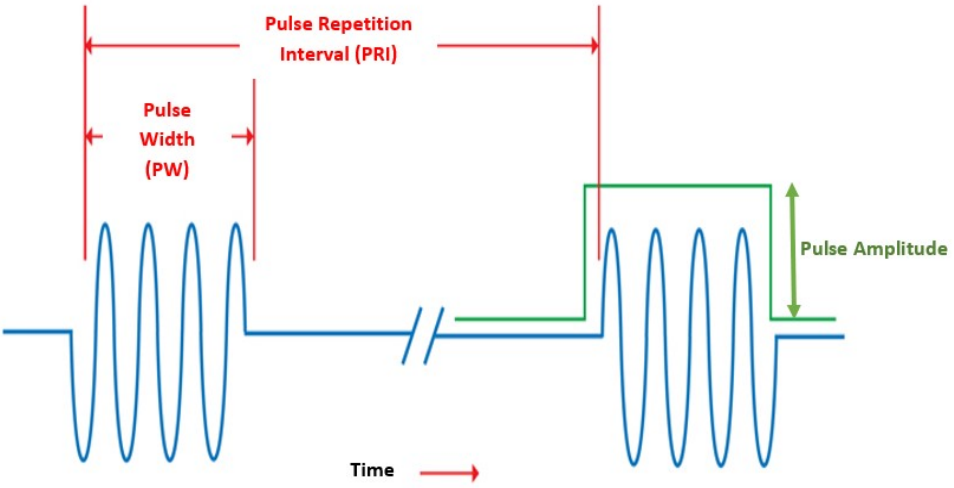

FIGURE 1.4: Pulse Radar

wave in the illustration depicts how the transmitter's output voltage changes over time. Referring to Fig. 1.4, the common radar parameters are described. Pulse Width (PW) has time units and is frequently represented in μs. The duration between pulses is known as rest time (RT). Pulse Repetition Time (PRT) has time units and is often measured in ms. PRT is the period of time between the beginnings of two successive pulses. The inverse of PRT, Pulse Repetition Frequency (PRF) is the number of pulses transmitted each second. Radio Frequency (RF) can be measured in GHz or MHz. Since a pulse radar does not continuously emit radiation, the average power is significantly less than the peak power. Instead of using the peak power, a radar system's capability is evaluated using the average power. Depending on the application, the average power of radar ranges from a few milliWatts (mW) to one or more megawatts (MW).

One picowatt (10^{-12} watt) is a possible limit for a weak echo signal coming from a target. In summary, a radar system's power levels can be both very high and very low as well. Radar waves travel through the atmosphere at a speed of about 300,000 km/s (the speed of light). The range of a target can be determined by calculating the time it takes for a radar signal to travel to and return from a target. The target's distance is equal to $cT/2$, where T is the radar's estimated round-trip time and c is the speed of light. The capability of radar to accurately determine a target's distance over long distances and in poor weather is its most

distinguishing characteristic. A simple pulse radar's range accuracy is a function of pulse width; the narrower the pulse, the higher the accuracy. However, large bandwidths in the transmitter and receiver are needed for short pulses.

1.5.1.2 Continuous Wave Radar

Continuous Wave Radar (CWR) is a type of radar that uses a continuous signal to operate. They employ the Doppler effect to recognize moving targets. The block diagram of CWR is shown in Fig. 1.5.

The two types of CWR are given as follows:

1. Unmodulated Continuous Wave Radar (UCWR)
2. Frequency Modulated Continuous Wave Radar (FMCWR)

1. Unmodulated Continuous Wave Radar (UCWR)

This type of radar uses a continuous signal to identify moving targets. It also goes by the name CW Doppler radar. Two antennas are needed for this radar. One of these two antennas is used for signal transmission, and the other antenna is utilized for signal reception. It does not measure the target's distance from the radar; it just measures the target's speed.

2. Frequency Modulated Continuous Wave Radar (FMCWR) This is a type of CW Doppler radar that employs frequency modulation. It is also known as Continuous Wave Frequency Modulated Radar (CWFMR). There are two antennas, one of which is used to transmit the signal and the other to receive it. Along with the target's speed, it also determines how far away the target is from the radar. Radars can also be categorized based on the tasks they perform. The following is a discussion of a few of them. Automotive collision avoidance systems and precise distance measurement benefit from the great range resolution and simultaneous measurement of target distance and velocity provided by CWFMR radar. Its uninterrupted waveform offers resilience to interference and efficient power usage.

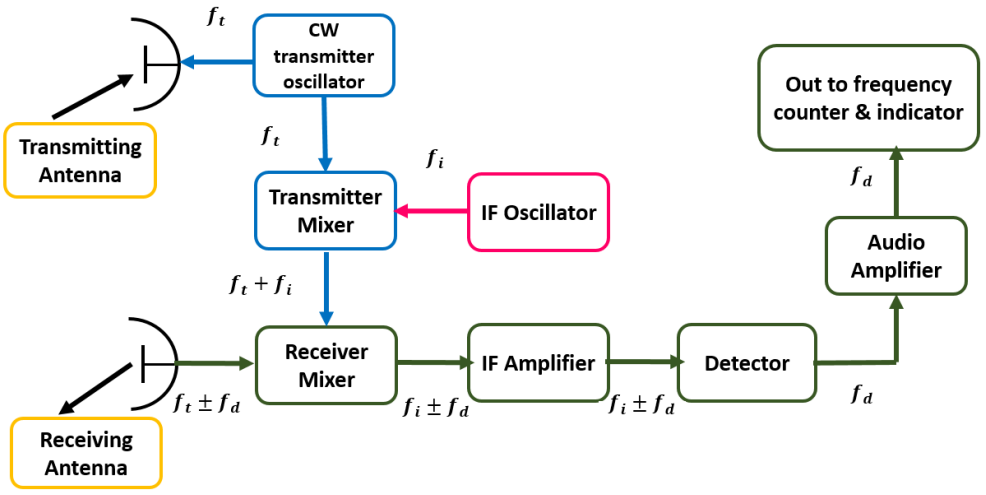

FIGURE 1.5: CW Doppler Radar with IF Amplification

1.5.2 Functionality Based Classification

Radars can be categorized based on the tasks they perform. Some of the categories defined based on functionality are listed below:

1.5.2.1 Airport Surveillance Radar

When an aircraft is within 75 to 110 km of its airport and above an altitude of 7,620 meters, airport surveillance radar systems can reliably detect and track it. More than 100 major airports across the United States have such systems installed. The ASR-9 is a radar that is designed to be operational for at least 99.9% of the time, which translates to as low as 10 hours of downtime each year.

1.5.2.2 Doppler Weather Radar

Radar has been used for many years to provide information about the intensity of rain and other types of precipitation. Numerous weather radars were developed by engineers, greatly expanding their capabilities by being able to measure the Doppler frequency shift in addition to the strength of the echo signal reflected by precipitation. The radial velocity of wind-blown precipitation is important and related to the doppler frequency shift. Downbursts, also known as microbursts,

are a significant weather risk to aircraft when they approach or depart from an airport. An airplane could be forced to the ground by this powerful downdraft's wind shear. The system type at or near airports that is specifically designed to find hazardous microbursts is known as Terminal Doppler Weather Radar (TDWR). It operates from 5.60 to 5.65 GHz (C band).

1.5.2.3 Airborne Combat Radar

In most cases, a combat aircraft is needed to attack surface targets on the ground or at sea in addition to intercepting hostile aircraft. Such an aircraft's radar must be capable of carrying out these specific military missions. Since each mission has unique criteria, this is challenging. Various radar waveforms are required depending on the ranges, precision, and speed at which the radar data must be collected, as well as the effect of the surrounding environment and the types of targets.

1.5.2.4 Satellite Surveillance Radar

The systems for tracking orbiting satellites and ballistic missiles are much larger than those used for tracking aircraft. Maximum ranges for these radars could be required to be between 3,700 to 5,600 km. Several hundred kW to one MW is the typical transmitter power of a Ballistic Missile Defense (BMD) radar, which is around 100 times more powerful than the typical transmitter power of radars used to detect aircraft. Radar systems for long-range ballistic missile detection and satellite monitoring commonly use lower frequencies (MHz).

1.5.2.5 Ground-Probing Radar

Usually, it is considered that radar waves are reflected from the ground's surface. However, lower-frequency radar energy can pass through the earth and bounce off buried things. At these frequencies, the propagation loss in the ground is relatively

substantial, but it is also low enough to allow for ranges of at least 3.3 to 33 feet (1 to 10 meters). This is sufficient for archaeological digs and for probing the subsurface soil to locate utility cables, pipelines, and tunnels. Since a bandwidth of 500 MHz is required for a 1-foot range resolution, broad bandwidth is often not possible at lower frequencies.

(a) Airborne Early Warning Radar [7]

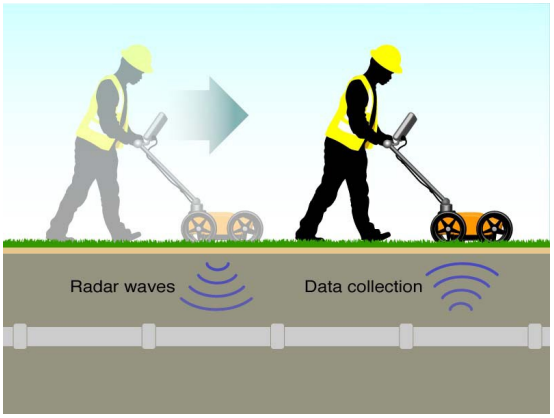

(b) Ground-Probing Radar [8]

1.5.2.6 Over-the-Horizon Radar

Radar applications often do not require frequencies lower than 100 MHz. The High Frequency (HF) band has the benefit that radio waves at these frequencies are refracted by the ionosphere, which allows them to travel far beyond the horizon before returning to the Earth's surface. This allows for target identification between 900 to 3,700 km. Since the earth's curvature restricts the range of ground-based microwave air surveillance radars, an Over-The-Horizon (OTH) radar may detect aircraft at distances up to ten times greater than those of those radars.

1.5.2.7 Tracking Radar

In order to determine a target's trajectory and estimate its future position, this type of radar continually tracks a single target in angle (azimuth and elevation) and range. The single-target tracking radar constantly updates the location of the target. A typical tracking radar might take ten measurements of the target's

location each second. Tracking radars are typically used for range instrumentation. The Air Force, Army, Navy, and NASA are the main organizations that employ tracking radars [9].

1.6 Factors Affecting Radar Performance

The following criterion can be used to assess the performance of the radar system:

1. The greatest distance at which it may see a target of a specific size.
2. The accuracy with which the target's distance and angle are measured.
3. The capability to distinguish one target apart from another.
4. The capability to identify the desired target echo in the presence of significant clutter echoes, unexpected interference from other friendly transmitters, or harmful radiations from hostile jamming.
5. The capability to recognize different types of targets.

This subsection talks about some of the key variables that influence radar performance.

1.6.1 Transmitter Power and Antenna Size

A radar system's maximum range is significantly influenced by the average transmitter power and antenna size. The typical normal power of many radar systems is 1 MW or more. There are many phased-array radars with a diameter of around 100 feet (30 meters), while some are much larger. Longer detection ranges and improved signal-to-noise ratios are made possible by higher transmitter power, but larger and more intricate antennas are also needed. Although smaller antennas are more useful for systems that are more compact, they frequently lead to decreased radar sensitivity and range. Optimizing radar system design for particular

applications requires striking the correct balance between transmitter power and antenna size.

1.6.2 Receiver Noise

The inevitable noise that appears at a radar receiver's input determines its sensitivity. At microwave radar frequencies, the noise that limits detectability is often created by the receiver rather than by external noise that enters the receiver through the antenna. The receiver is made to improve desired signals while reducing overall noise and other unwanted signals that inhibit detection. Additionally, the matched filter is used which increases the SNR ratio at the receiver output.

1.6.3 Target Size

It's not always the case that a target's size as seen by radar corresponds to its actual size. The radar cross-section, which is expressed in units of area, is a measurement of the target size as seen by radar (square meters). Two targets with the same physical cross-sectional area may have very different radar cross-sections or sizes.

1.6.4 Clutter

Echoes from the land, rain, snow, sea, hail, insects, birds, and meteors are fascinating to people who monitor and study the environment, but they are a hassle for people who wish to detect aircraft, missiles, ships, or other comparable targets. As a result, a large portion of radar design is focused on limiting the impacts of clutter without diminishing the echoes from desired targets.

1.6.5 Atmospheric Effects

The performance of radar can also be impacted by additional atmospheric phenomena. Radar waves are bent as they travel through the atmosphere due to the

Earth's atmosphere losing density with altitude. This typically extends the detection range at low angles. The formation of ducts in the atmosphere allows radar energy to be trapped, guided around the curvature of the Earth, and detected at distances beyond the normal horizon. When propagating through a clear blue sky or rain, the loss of radar energy due to atmospheric absorption is often minimal for the majority of microwave-operated systems.

1.6.6 Interference

Strong enough signals can enter a radar receiver and generate erroneous results if they originate from adjacent emitters like radars and other devices. Even though they may find it annoying, well-trained operators are not frequently misled by interference. However, interference cannot be ignored as easily by automatic detection and tracking systems. As a result, some method is typically needed to identify and remove interference pulses before they approach the radar's automatic detector and tracker.

1.7 Electronic Warfare (EW)

Electronic Warfare (EW) is the term used to describe any operation involving the use of electromagnetic spectrum to seize control of the spectrum, fight with an enemy, or resist such attacks. In order to ensure that friendly forces have unrestricted access to the electromagnetic spectrum and to deny the enemy an advantage over it, EW was invented. EW includes the entire RF spectrum as well as the infrared, optical, and ultraviolet spectrum. EW receivers are designed to detect, identify, and locate threats. The countermeasures are designed to reduce the effectiveness of those threats. EW is responsible for responding to the threat signals that are present in its environment [10]. As a result, since the advent of advanced EW in the early 1940s, some sort of processing has been required to decide when and how to use the appropriate countermeasures. Originally, the selection of appropriate countermeasures was entirely dependent on the ability of trained operators

to identify threat signals. Receivers collect RF signals because humans are unable to detect them immediately. The signals were then processed in some manner before being presented in a way that operators could interpret. It was essential to automatically detect and classify threats as the signal environment became more complicated, and radar-controlled weapons became more destructive. Numerous sensors and countermeasures are frequently included in fully integrated modern EW systems. These system resources must all be managed and coordinated [10]. In many nations over the past few years, the divisions of the EW field have been revised. The following definitions are currently accepted in NATO as shown in Fig. 1.6.

1.7.1 Electronic Support (ES)

In order to focus operations in the future and recognize threats immediately, Electronic Support (ES) or Electronic Support Measure (ESM) requires looking for, intercepting, identifying, and localizing sources of intentionally and unintentionally transmitted EM energy. Identifying the types and locations of the enemy's forces, or weapons is another use for the received signals, which is known as situation awareness. ES often collects a lot of signal data to facilitate less intensive processing with a high throughput rate. ES typically determines which of the recognized emitter types is present and where they are placed.

1.7.2 Electronic Attack (EA)

EA involves the use of EM energy, directed energy, or anti-radiation weapons to attack people, places of business, or components of machinery in an effort to reduce, neutralize, or eliminate an enemy's fighting ability. The effectiveness of military radar is intentionally reduced by hostile Electronic Countermeasures (ECM). ECM can include noise jamming, which enters the receiver through the antenna and increases the noise level at the receiver's input; false target generation, in which hostile jammers introduce additional signals into the radar receiver to try

and fool it into believing they are real target echoes; and chaff, an artificial cloud made up of numerous tiny metallic reflecting strips that produce strong signals.

1.7.3 Electronic Protection (EP)

The techniques and methods used for EP work to mitigate the consequences of an electronic attack (EA). The radar's EP or Electronic Counter Countermeasure (ECCM) technology prevents attempts to jam it by an EA system. Even though it is commonly known that anti-radiation and directed energy weapons are closely related to EW, they were not regarded as EW. They differ in that they are weapons.

1.7.4 Radar Warning Receiver (RWR)

ESM system plays a vital role in modern EW for investigating intercepted signals. Once the signal is detected at the Radar Warning Receivers (RWR), the classification is done based on intrapulse modulation schemes. Therefore, an automatic intrapulse modulation classification algorithm is required to distinguish among different emitters and to estimate their intrapulse parameters at the RWR [11].

RWR is the system that analyzes the intercepted signal and tries to find out information about the location and type of hostile emitter using wide coverage antennas so that a threat may be generated against it. The RWR sends this information in real-time to aircrew personnel so that they might make appropriate responses. For an Airborne RWR, the operational needs and mission-specific trade-offs ultimately determine whether to use a single antenna or several antennas. In order to balance factors such as cost, complexity, and performance, certain RWR systems could employ a combination of single and multiple antennas. The intended capabilities of the RWR system, the available technology, and the threat environment will all play a role in determining which antenna arrangement is best. Fig. 1.7 shows a top-level block diagram for an airborne RWR. The signals are

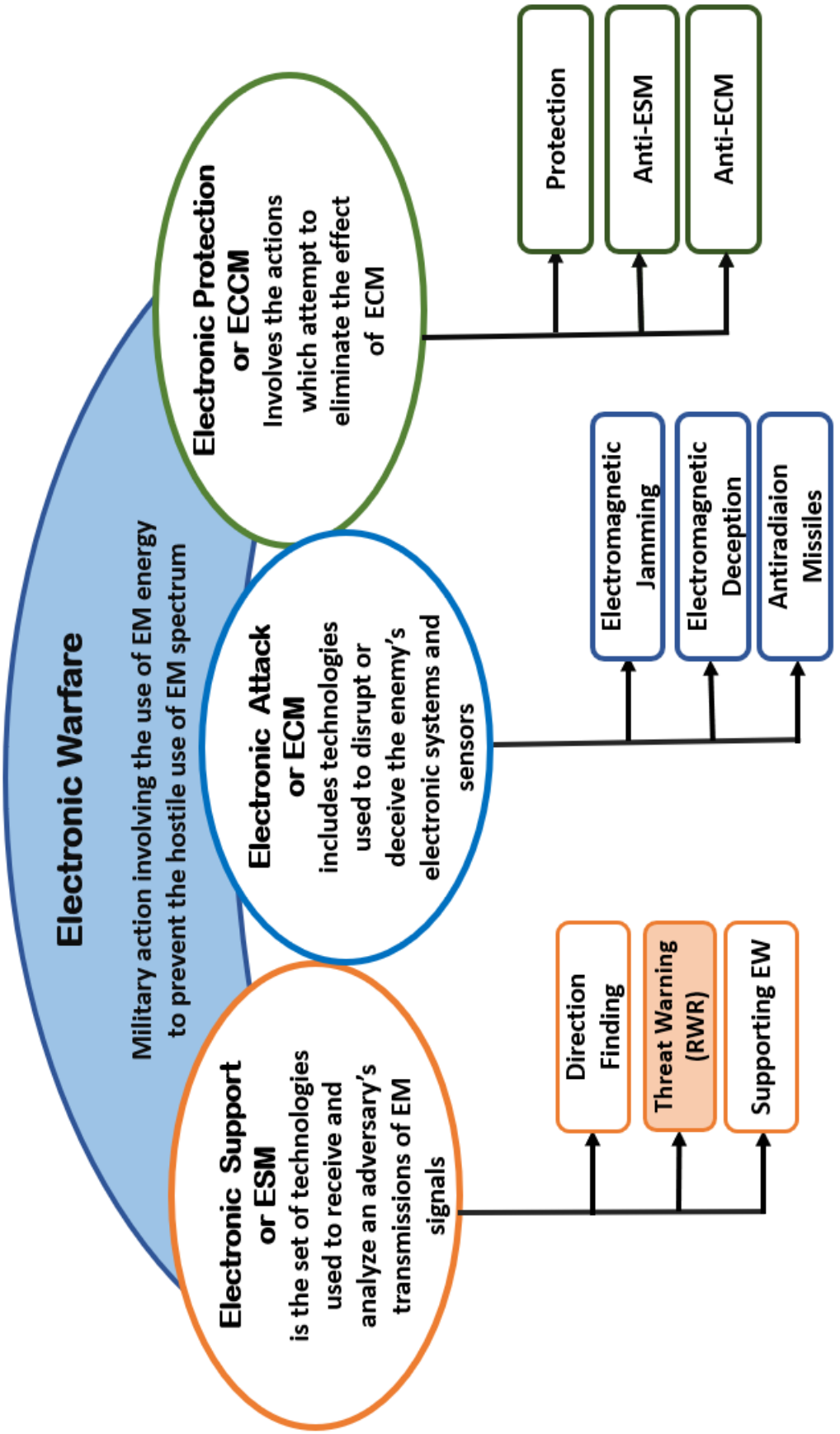

FIGURE 1.6: Components of Electronic Warfare

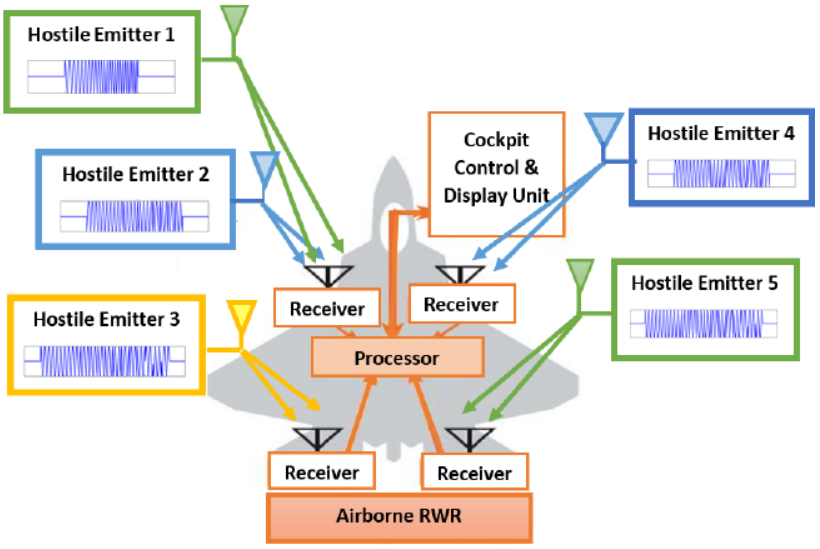

FIGURE 1.7: Signals Received at RWR by Multiple Threat Emitters

received at RWR from multiple threat emitters and are then analyzed to determine their intrapulse modulation schemes.

1.7.4.1 RF Threat Identification

Threat identification can be done with the help of modulation schemes used by threat emitters. These modulation schemes may include:

1. Frequency Shift Keying (BFSK/QFSK),
2. Linear Frequency Modulation (LFM),
3. Nonlinear Frequency Modulation (NLFM),
4. Phase Shift Keying (BPSK/QPSK), and
5. Polyphase Modulation (FRANK, P1, P2, P3, P4).

We are interested in emitter recognition using polyphase-coded modulation schemes. In Section 2.1.2, the literature survey of radar emitter recognition techniques that employ phase-coded signals is performed along with their shortcomings.

1.7.5 Low Probability of Intercept (LPI) Radars

The electromagnetic environment is quite complex for modern EW due to the strong impact of noise and the parameters of radar keep on changing over time. Most radars used in the naval battlefield today, such as those used for surveillance, reconnaissance, and target tracking, must deal with very strong and sophisticated threats intended to decrease the effectiveness of radars. Such threats include ES, EA systems, RWRs, and Anti-Radiation Missiles (ARMs). It is essential for the radars to conceal their emissions from modern threats and these radars are known as LPI radars. LPI signals have very wide bandwidth, properly managed transmit power, frequency-agile, advanced scanning patterns, and reduced side lobes. It is now challenging for conventional RWR to identify and parameterize the low-power and high-bandwidth LPI radars. In this research, we are supposed to be at RWR that will intercept the signals from multiple emitters (LPI) and it has to recognize the different emitters based on their intra-pulse modulation schemes. [12].

A common method for realizing LPI radar signals is to utilize some type of pulse compression technique to lower the radar's Effective Radiated Power (ERP). In practice, pulse compression based on intrapulse modulation produces a significant time-bandwidth output with high radar signal processing gain. Additionally, recent developments in optimization techniques have been used to create radar waveforms that can improve the performance of LPI radar systems. Several polyphase-coded waveforms, including Frank, P1, P2, P3, and P4, and frequency hopping are examples of LPI waveforms. In LPI radar, phase-coded waveforms are created by generating different phase patterns within a pulse. These radar signals fall under the category of non-stationary signals. In order to generate the polyphase-coded signal some parameters are significant including carrier frequency (Fc), no of phases within a pulse, and Cycles Per Phase (CPP). Higher frequency resolution is required to estimate the Fc and there is always a trade-off between time and frequency resolutions. LPI radar systems attempt to reduce the probability that a threat signal can be detected by an EW receiver in two different

ways. Initially, by carefully controlling the radiation and scan patterns and location of power transmission. Second, the radar waveform uses high-duty cycles or CW signals with advanced modulation techniques that span large bandwidths to lower the average power density. Compared to an intercept receiver, LPI radars are able to detect targets at a further distance [12]. The waveform is transmitted by spreading in wide-band noise. Advanced signal processing algorithms are then used to extract the LPI radar signal from wide-band noise. Due to the extraordinary properties of LPI radar waveforms, the conventional waveform recognition techniques using parameter matching from the database are unable to recognize such radars. Therefore, it is crucial to find a novel radar emitter recognition method at the hostile receiver side to improve the recognition accuracy of phase-coded waveforms at low SNR. In the following paragraphs, LPI radar waveforms are discussed in detail along with their formulas. Barker, Frank, P1, P2, P3, and P4 codes are among the phase-coded signals utilized in our research.

1.7.5.1 Barker Code

The binary phases that make up the Barker codes have a peak-to-peak side lobe ratio of M (Length of code). The side lobe level ratio for the longest length code is reported to be -22.3 dB, and Barker codes are not available for M>13. As a result of their low complexity, Barker-coded pulses frequently employ binary phase modulation. Only the lengths M =2, 3, 4, 5, 7, 11, and 13 are available for these codes, which only contain side lobes of unity magnitude [13]. Long-duration pulses can be modulated using polyphase modulation, which uses several phase values. As compared to bi-phase codes, polyphase codes produce lower-side lobes. The definition of polyphase-coded waveforms in mathematical form is presented in the next subsection.

1.7.5.2 Frank Code

Frank is a polyphase code having good non-periodic correlation properties. The phase history of the LFM pulse is used to develop the Frank code, which is a

perfect code. With this code, only perfect square length ($N = L^2$) is applicable. The phases of sub-pulses can be generated using the formula given in (1.1).

$$\phi_{m,n} = \frac{2\pi}{L}(m-1)(n-1), \tag{1.1}$$

where, $1 \leq m \leq L$ and $1 \leq n \leq L$. The middle of the Frank code has more phase increments than either of the ends [13].

1.7.5.3 P1 Code

The step approximation of an LFM signal yields the P1 and P2 codes. The length of code is ($N = L^2$), according to [13]. The phase value of the m^{th} sample of the n^{th} frequency step can be determined using (1.2) if m signifies a sample number in a given n^{th} frequency step.

$$\phi_{m,n} = -\frac{\pi}{L}[L-(2n-1)][(n-1)L+(m-1)], \tag{1.2}$$

where, m= 1, 2, 3, ..., L, n= 1, 2, 3..., L and N should be a perfect square length. For P1 code, the Peak side lobe level (PSL) is expressed by using the following formula:

$$PSL = 20log_{10}\left(\frac{1}{L\pi}\right). \tag{1.3}$$

1.7.5.4 P2 Code

Even values of L cause low-level auto-correlation side lobes, but the P2 code still works for perfect square lengths. The phase values for sub-pulses are calculated using the formula expressed below:

$$\phi_{m,n} = -\frac{\pi}{2L}[2m-1-L][2n-1-L], \tag{1.4}$$

where, m= 1, 2, 3, ..., L, n= 1, 2, 3, ..., L and L= 2, 4, 6, ... For both P1 and P2 codes, high phase increments are seen at the start and end of the code in

comparison to the center. P2 codes are developed from the step approximation of LFM pulse. The initial phase values for P2 are different, but it has the same phase increments as P1 [13].

1.7.5.5 P3 Code

The Zadoff-Chu codes, which are applicable for any length N_c, are used as a basis for the P3 and P4 codes [13]. The phase of the m^{th} sample of the P3 code can be calculated using the formula in (1.5).

$$\phi_m = -\frac{\pi}{N_c}\big(m-1\big)^2, \tag{1.5}$$

where, m=1, 2, ..., N_c, and N_c denotes the compression ratio.

1.7.5.6 P4 Code

The formula provided in [13] describes the phase values of a P4 code and is given below:

$$\phi_m = -\left[\frac{\pi(m-1)^2}{N_c}\right] - \pi(m-1), \tag{1.6}$$

where, m= 1, 2, ..., N_c. The largest phase increments in the center of code like the Frank code, distinguish the P3 code from the P4 code. P3 and P4 codes are more resistant to Doppler than other polyphase codes.

1.8 Motivation

LPI radars frequently employ phase-coded modulation schemes in their waveforms. Radar emitters (LPI) that use phase-coded waveforms can produce distinctive signatures that can be identified and categorized through specific emitter recognition algorithms. Moreover, the resistance to interference provided by phase-coded modulation also makes it challenging for RWRs to interfere with LPI radars without being aware of the precise phase-coding scheme. This serves as a motivational

factor behind this research effort to identify the specific phase-coding scheme used by the LPI radar to facilitate the RWR. According to the literature, extracting information from the magnitude spectrum of Time Frequency Representations (TFRs) is necessary for the identification of phase-coded LPI radar waveforms. Additionally, the recognition has been done in recent research studies with a minimum reported SNR of -10 dB. However, a novel phase spectrum-based method is required to enhance recognition accuracy even in low SNR settings ($<$ -10 dB).

1.9 Research Objectives

In light of the limitations and motivation discussed in the previous section, the aims and objectives of this research are as follows:

1. To propose a phase spectrum-based feature extraction method for enhancing the recognition of phase-coded waveforms at low SNR values ($<$ -10 dB).
2. To analyze the efficacy of the proposed phase-based features using different deep learning architectures.
3. To compare the recognition accuracies of phase-coded signals obtained at the output of two different deep learning architectures (BiLSTM and DCNN).

1.10 Organization of the Dissertation

The thesis comprises the following chapters:

Chapter 2 provides a review of the various radar emitter recognition methods that have been employed in the literature. In order to select the best option for the desired research, multiple TFRs and deep neural networks are compared on the basis of various parameters. In the next sections, the chapter includes the problem statement, the research methodology, and finally the contributions of this dissertation.

Chapter 3 explains the fundamentals of the recently proposed feature extraction technique based on the phase spectrum obtained from the Short Time Fourier Transform (STFT). The overall methodology and system overview of the proposed research work for both of the deep learning architectures (BiLSTM and DCNN) used in this research is also provided.

Chapter 4 provides the simulation parameters as well as the phase-coded waveform recognition results for both proposed architectures. Additionally, this chapter contains information on significant training parameters that were used to train both architectures. The two proposed emitter recognition methods are compared in order to determine which is better. On the basis of SNR, a comparison is also made with other state-of-art techniques utilized in the literature for emitter recognition.

The major findings of the research provided in this thesis are summarized in Section 5, along with a conclusion and some suggestions for potential future research.

1.11 Chapter Summary

This chapter covers the fundamentals of radar systems as well as their historical background. The classification of radar systems according to waveform types and functions is also discussed. The explanation of EW and its subcategories is followed by a discussion of LPI radar waveforms. The key objectives and motivation highlighted at the chapter's end, along with an overview of the entire thesis. In the next chapter, a literature survey of radar emitter recognition techniques is to be introduced; the gap derived and the proposed solution is also mentioned at the end of the chapter.

Chapter 2

Literature Review, Gap Analysis, and Proposed Solution

The literature review and research directives in radar emitter recognition technology are covered in Section 2.1 of this chapter. The literature review of time-frequency transforms and machine learning architectures are covered in Section 2.2 and 2.3 respectively in order to choose the best one for the radar emitter recognition at low SNR values. The gap analysis presented in Section 2.4 was achieved by the extensive literature review, which assisted in identifying the areas of concern in the previous studies. The chapter's next sections include the problem statement, proposed solution, and ultimately the contributions of the dissertation.

2.1 Existing Research Directives in Radar Emitter Recognition (RER) Technology

It is challenging to differentiate between the various threat signals present in a measured spectrum due to the complexity of today's radar environment. More radar types have evolved as a result of the rapid developments of radar technology. A Radar Emitter Recognition (RER) system that can operate effectively with a range of radar types is particularly difficult to create. The recognition of

intrapulse modulation schemes have been the focus of numerous studies conducted on RER techniques. The aim of automatic intrapulse modulation classification is to classify the intrapulse modulated and noise-embedded LPI radar signals. LPI radars are special radars that try and hide their signals from hostile receivers, such as RWRs [12, 13]. The peak Effective Radiated Power (ERP) of the radar is often decreased by utilizing pulse compression techniques in order to achieve LPI radar signals. Intrapulse modulation is a very helpful technique for pulse compression. It has a significant radar signal processing gain and a high bandwidth-time product. In order to widen the bandwidth, the transmitted pulse is either phase or frequency-modulated. The emitter recognition procedure is a crucial technique in the area of electronic countermeasures as initially it involves the preprocessing of the intercepted radar signal. The intrapulse modulation schemes utilized by intercepted signal is then determined using some specific algorithm.

2.1.1 Phases of Radar Emitter Recognition Technology

Radar emitter recognition (RER) technology development has undergone the following three phases as shown in Fig. 2.1

1. The conventional methods for identifying specific emitters are used in the first step. These approaches primarily employ a parameter-matching strategy to compare the parameters of the intercepted radar signals with the data already stored in the database. This method seems to be computationally less extensive but in order to cope with the varying parameters of LPI radar waveforms it becomes difficult to recognize the exact emitter [14].

2. The second stage seems to be matured as it makes use of radar intrapulse parameters combined with Neural Networks (NNs) to boost the accuracy and recognition performance as compared to the traditional approach. The Intrapulse parameters including Pulse Width (PW), Time Of Arrival (TOA), Pulse Amplitude (PA), Direction Of Arrival (DOA), and intrapulse modulation are fed as features to the NN for the classification [15]. Features

may be distorted due to noise and interference which may lead to degraded performance.

3. The third stage involves the Deep Neural Networks (DNNs) including Deep Belief Network (DBN), Feed Forward Neural Network (FFNN), Recurrent Neural Network (RNN), Long Short Term Memory (LSTM), and Convolutional Neural Network (CNN) using special pre-processing techniques to improve the recognition rates. The combination of DNNs like CNN-RNN, CNN-LSTM, and CNN-LSTM-DNN have shown very good recognition accuracies [16–18].

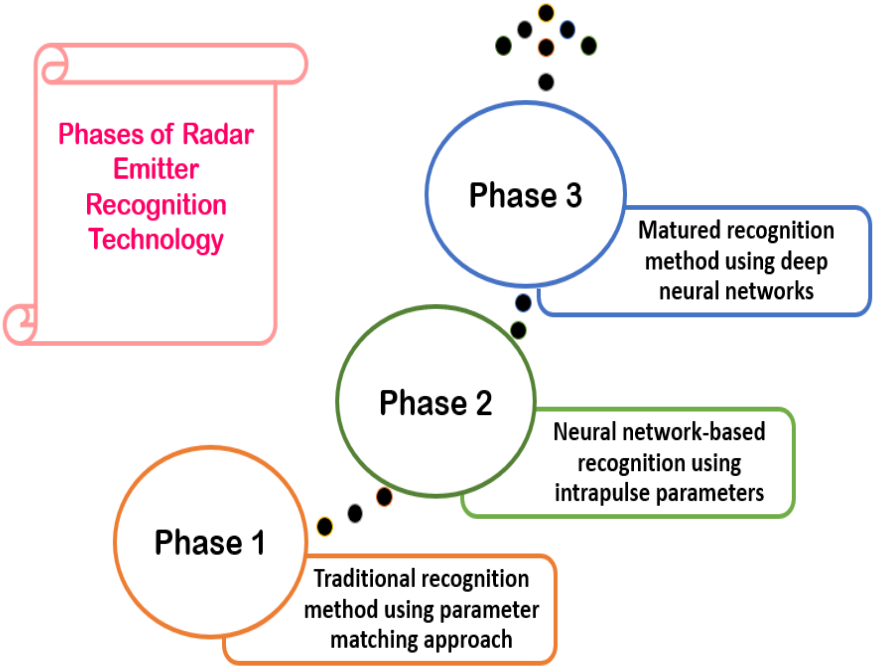

FIGURE 2.1: Phases of Radar Emitter Recognition Technology

2.1.2 Literature Survey of RER Methods

Real-time classification and detection of the intrapulse modulation schemes of intercepted signals from LPI radars are very crucial in EW systems. Therefore, such waveform recognition techniques have gained much attention over the past

few decades. In this section, some LPI radar waveform recognition techniques presented in the literature are discussed along with their shortcomings. For the classification and analysis of LPI radar waveforms, some signal processing methods are developed in [19]. Based on the kind of pulse compression techniques used for phase-coded waveforms, the classification of signals from different emitters is done. Fractional Fourier Transform (FrFT) is computed and further classification is performed. Even at the low SNR of -10 dB, overall recognition accuracy for the phase-coded waveforms is observed to be 87%. Moreover, the classification accuracy of the Barker code is not discussed in this work.

An automatic radar waveform identification system is investigated in [20] for detecting and tracking LPI radars. Twelve different types of radar signals, including polyphase codes, may be classified by the system. The CNN and Elman Neural Network (ENN), two relatively independent networks, are presented as a hybrid classifier. At an SNR of -2 dB, the experiments show a 94.5% successful recognition ratio. In the NN based approaches, training data is simulated based on different parameters and AWGN is added to the signals to make them more realistic in nature. A technique for recognizing eight different types of radar waveforms is investigated in [21]. The classifier is an artificial bee colony (ABC) algorithm optimized by Support Vector Machine (SVM). At SNR of -4 dB, the overall recognition rate is 92%, according to the simulation findings. A novel method for radar emitter recognition based upon intrapulse parameters is proposed using the variant of Short Time Fourier Transform (STFT) and Reinforced Deep Belief Network (RDBN) in [22]. In this method, 60% recognition accuracy is achieved at an SNR of -10 dB. When the SNR decreases, Linear Frequency Modulation (LFM) and Non-Linear Frequency Modulation (NLFM) get confused with other modulation schemes and their recognition accuracy is further reduced. In [23], a recognition technique based upon CNN is proposed for LPI radar waveforms. In order to reduce the computational cost, the Sample Averaging Technique (SAT) is also proposed as the intercept receiver has to process more samples to improve the detection. From the confusion matrix, it is clear that FRANK, P1, P3, and P4 signals can be detected with an accuracy of less than 90% that needs further improvement.

The overall accuracy is observed to be 90% at SNR= -10 dB. The performance accuracy of Barker codes is also not considered in this paper. Recurrent Neural Network (RNN) based recognition technique is proposed in [24] to perform denoising, classification, and deinterleaving of a pulse stream. RNN has the capability to mine temporal patterns in the given data by using the pulse streams belonging to certain classes and supervised learning is performed. The trained RNN is then used to categorize different classes present in the test streams and can also do predictions for the upcoming pulse streams. Only PW and Pulse Repetition Interval (PRI) are the parameters considered for the Specific Emitter Identification (SEI) process.

The hierarchical decision tree-based classification is proposed in [25] that seems to be appealing in real-time applications when the Optical Fiber (OF) channels are used to transmit the received LPI radar signals. Noise and distortion are added to signals that may reduce the classification accuracy. In the proposed method, classification accuracy is observed in the presence of Additive White Gaussian Noise (AWGN) and OF impairments (chromatic dispersion). The overall recognition accuracy for noiseless intercepted phase-coded waveforms is observed to be 100% at Optical SNR (OSNR)= 10 dB. The performance accuracy of Barker codes is also not considered in this paper. Moreover, the recognition accuracy of P1 and Frank code has improved from 0% to 100% after the CD correction factor which seems to be ambiguous. Waveform Classification method based on the Fourier-based Synchrosqueezing Transform (FSST) and CNN is proposed in [26]. FSST offers better performance over the extensively used Choi William Distribution (CWD) for identifying the phase-coded waveforms even at low SNR of -10 dB in the case of LPI Radars with an overall accuracy of 98.4%. However, the proposed method has a lower capability to distinguish between the LFM and Costas codes at low SNR values.

A novel network is proposed in [27] that combines a shallow CNN, Long Short-Term Memory (LSTM) network, and Deep Neural Network (DNN). This method can recognize six different radar emitter signals at the SNR ranging from -14 dB to 20 dB. Three different types of signals are given at the input of a combined

network for analysis including time, frequency, and auto-correlation domain. CNN is used for feature extraction and features are then fed to the LSTM network. Finally, DNN is used to give the classification results. The auto-correlation domain has the recognition accuracy of 90% at -6 dB as compared to other domains. The recognition accuracy of polyphase-coded waveforms is not discussed in this work. A novel emitter recognition method is proposed in which PW images are obtained and CNN is used for classification [28]. PW images are transformed from a time domain into 2D binary images that are fed to CNN. The proposed method outperforms the other techniques in literature to identify the uncertain modulations and varying PW in the intercepted radar signal. Only the pulse amplitudes are considered for the SEI process and phase-coded modulations are not discussed.

The combination of CNN and LSTM has also proved to be powerful in the literature for automatic emitter recognition techniques. CNN is capable of extracting spatial characteristics and LSTM can extract temporal characteristics in the pulse stream. CNN-LSTM can exploit spatial and temporal characteristics simultaneously. In [29], a novel recognition method for radar emitter signals is proposed using CNN-LSTM architecture along with STFT. The proposed algorithm can identify the eight different radar signals with an overall accuracy of 96.95% at the SNR of -2 dB. Only Barker and P2 codes are discussed in this research work. The Multiple Feature Images Joint Decision (MFIJD) model is proposed in [30] with two distinct feature extraction structures. It has been noted that Structure 2, which is based on the LSTM, has 83% overall recognition accuracy at SNR= -6 dB and 91% at SNR= -3 dB respectively. Finding the various intrapulse modulation methods that LPI radar waveforms employ has been a significant research challenge for many decades.

In [31], a unique CNN architecture for automatic modulation classification is proposed for SNR ranging from -4 dB to 20 dB. The suggested model makes use of an asymmetric convolution structure to decrease computational complexity. However, in this work, phase coded signals are not considered. Intrapulse modulation

classification method using intrapulse signatures and deep residual learning is proposed in [32] that can recognize eight types of radar waveforms with an overall accuracy of 94.1 % at -8 dB SNR. Frank codes are only considered in this work. In [33], 1D-CNN with the selective kernel is used to classify intrapulse modulation of eleven types of radar signals. Polyphase codes other than Frank codes are not taken into account in this work. Radar emitter recognition using a unique 1D Deep Residual Shrinkage Network (DRSN) is described in [34]. This analysis does not take phase-coded signal recognition accuracy into account. The end-to-end denoising and recognition of radar signals are proposed using a denoising network based on an inception method in [35]. The overall recognition accuracy is 89.25% at an SNR of -10 dB. Only Frank codes are considered in this work. [36] uses a transfer learning method using CNN to enhance the recognition accuracies of nine various kinds of radar waveforms. Initially, three intrapulse modulation types of radar signals that are easily collected and have enough samples are used to train a 1D CNN. Following that, nine different kinds of few-shot complex intrapulse modulation classification tasks in the target domain are used to employ the knowledge acquired by the convolutional layer. Other than the Frank code, the recognition of polyphase codes is not considered. In [37], a CNN-based intrapulse modulation recognition method is proposed using semi-supervised data. However, phase-coded signals are not considered in these researches except Frank code [35–37]. A recognition method using dual channel CNN and feature fusion is used in [38] to recognize twelve different types of LPI radar waveforms with 97% accuracy at SNR of -6 dB. In order to differentiate eight different types of intrapulse modulations of radar signals, a novel end-to-end sequence-based network that consists of a shallow CNN, a BiLSTM network strengthening with a self-attention mechanism, and a dense NN is created in [39]. The simulation results demonstrate the reliability and effectiveness of autocorrelation features. Additionally, the proposed network achieves more than 95% accuracy at -10 dB and roughly 61.25% accuracy at -20 dB. The situations with very low SNR have been taken into account in this research work, although polyphase-coded signals have not been considered in this study. The majority of state-of-the-art techniques, such as [40], exhibit lower

recognition accuracies for phase-coded signals exploiting the magnitude spectrum at low SNR values. In this study, we propose a phase spectrum-based method for feature extraction since phase should be a good candidate for the detection of phase-coded signals. The phase spectrum-based emitter recognition is performed in [16, 41] and the results are provided in Chapter 4 of the dissertation. Additionally, a tabular version of the literature survey of the different radar emitter recognition techniques is presented in Table 2.1.

In applications related to signal processing, the time domain representation is not always the ideal one. Mostly the eminent information of the signal is concealed within its frequency content. Time-Frequency Representation (TFR) is used in signal processing to investigate the time-varying signals as their spectral contents changes with time. In literature, there are several TFRs that are used to transform time domain radar waveform into 2D time-frequency images which are further given at the input of DNN for analysis. Different TFRs are used including STFT, CWD, Wigner Ville Distribution (WVD), cross WVD, FrFT to generate the time-frequency representation from which the parameters of polyphase coded signals are derived [42–54]. Literature survey of some time-frequency techniques is given in the next subsection.

2.2 Time Frequency Representations (TFRs)

A TFR is a 2D function that provides spectral and temporal information simultaneously for investigating non-stationary signals. Such information is unavailable if we use frequency or time representation separately. TFRs are widely used to identify, extract and classify the auto-components of a multi-component signal. Mostly the comparison of TFRs is done based on the capability of cross-term suppression, resolution, computational complexity, phase retrieval information, etc. It is crucial to choose the appropriate time-frequency transformation function for the data to be analyzed and to provide good resolution in both time and frequency. Choosing an appropriate TFR depends on the application being considered.

TABLE 2.1: Literature Survey of Deep Learning Techniques for Radar Emitter Recognition (RER)

SN	Years	Ref.	Techniques	Limitations
1	2017	[19]	WVD-FrFT	SNR=-10 dB (87% accuracy), Barker codes are not considered.
2	2017	[20]	CWD with CNN-ENN	SNR=-2 dB (94.5% accuracy).
3	2018	[21]	ABC-SVM	SNR=-4 dB (92% accuracy).
4	2018	[22]	STFT-RDBN	SNR=-10 dB (60% accuracy).
5	2018	[23]	SAT-CNN	SNR=-10 dB (90% accuracy), Barker codes are not considered.
6	2018	[24]	RNN	PW and PRI considered for emitter identification.
7	2019	[25]	Decision Tree	Optical SNR=10 dB (100% accuracy).
8	2019	[26]	FSST-CNN	SNR=-10 dB (98.4% accuracy).
9	2019	[27]	CNN-LSTM-DNN	Polyphase coded signals are not considered.
10	2020	[28]	PW images-CNN	Polyphase coded signals are not considered.
11	2020	[29]	STFT-CNN	Only Barker and P2 codes are discussed.
12	2020	[30]	MFJID	SNR =-6 dB (83% accuracy).
13	2020	[31]	CNN	SNR=-4 dB to 20 dB (phase coded signals not considered).
14	2021	[32]	Deep residual learning	Only Frank codes are considered.
15	2021	[34]	DRSN	Only Frank codes are considered.
16	2021	[39]	CNN-BILSTM-NN auto correlation features	SNR=-20 dB (61.25% accuracy), Phase coded signals are not considered.
17	2022	[35]	Denoising-guided disentangled network	Only Frank codes are considered.
18	2022	[36]	CNN and Transfer Learning	Only Frank codes are considered.
19	2022	[37]	CNN with feature fusion	SNR= -6 dB (97% accuracy).
20	2022	[55]	Power Spectral Analysis and deep learning	Only Barker and Frank codes are considered.
21	2022	[56]	De-noising encoder and X-net	Only Frank codes are considered.
22	2022	[57]	CWT and CNN	Only Frank codes are considered.

The recognition techniques for LPI radar waveforms have evolved in past few decades using feature extraction techniques to extract the useful features from intercepted radar signals and further classification is performed.

Different TFRs are used to transform the time domain waveform into a 2D time-frequency image that is further used for feature extraction. TFRs have proved to be useful in the successful identification and extraction of auto-components in a multi-component signal. Such TFRs may include STFT, Wavelet Transform (WT), Gabor Transform (GT), WVD, CWD, Reassignment Method (RM), Synchrosqueezed Transform (SST), etc. The recent radar waveform recognition methods use CWD or Fourier-based SST (FSST) as they have a good resolution of auto-components and cross-terms (noise or interference) are suppressed by using special kernels.

1. **Linear TFRs**

   Linear TFRs include STFT, WT, GT, etc. shown in Fig. 2.2. Such transforms obey the law of superposition. In linear TFR, auto-components have low resolution and they don't offer cross terms.

2. **Quadratic TFR**

   Quadratic TFRs fulfill the following criteria:

$$|x(t)|^2 = \int TFR_x(t,w)dw, \tag{2.1}$$

$$|X(w)|^2 = \int TFR_x(t,w)dt. \tag{2.2}$$

   Quadratic TFRs include WVD, Smooth Pseudo WVD (SPWVD), CWD etc., offer good resolution for auto-components but they suffer from cross-terms.

Linear and quadratic TFRs have their own pros and cons. There is no distinct transform that can fulfill all the requirements for any application. An analysis has been performed to highlight the strengths and weaknesses of these linear and

quadratic TFRs.

Two main goals for a desired TFR are:

1. Auto-components having high concentration.
2. Elimination of the cross-terms.

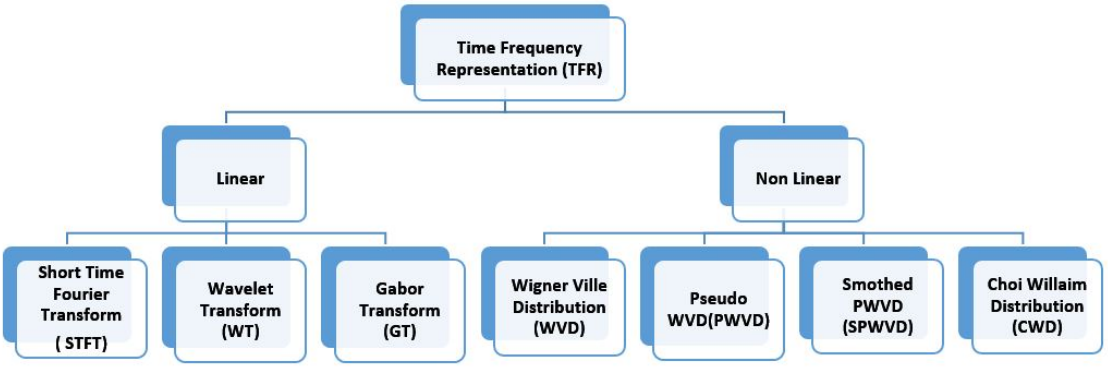

FIGURE 2.2: Time Frequency Representations (TFRs)

2.2.1 Literature Survey of Time-Frequency Representations (TFRs)

The literature survey of TFRs has been performed to analyze them based on different parameters and to choose the suitable one for our proposed method. These transformations are very helpful for studying non-stationary signals, which are found in vibration analysis, radar, and voice processing, among other fields.

2.2.1.1 Fourier Transform (FT)

The amplitude and frequency representation of a signal is obtained if the Fourier Transform (FT) of a time domain signal is computed. The benefit of Fourier analysis is that during transformation very less information is lost and the phase also remains preserved. In FT, perfect resolution in frequency is achieved as the kernel

function is a window of infinite length. The FT has many applications in various fields but it is not suitable for non-stationary signals as their spectral components vary over time [58].

2.2.1.2 Short Time Fourier Transform (STFT)

The Short Time Fourier Transform (STFT) is a windowed FT used to determine the phase and frequency information about local sections of a signal as it varies with time. The optimal width of the window must be chosen so that the signal is assumed to be stationary during that time. STFT is a widely used tool as it has simple interpretation and fast implementations. It enjoys benefits over the FT as it provides information about the time localization of spectral contents of a time-varying signal. STFT is also widely used in LPI radar waveform recognition methods to identify the intrapulse modulation parameters [22, 59–61].

2.2.1.3 Gabor Transform (GT)

The Gabor Transform (GT) is an STFT using the Gaussian function as a window. FT of a Gaussian function is also a Gaussian function but the window length is different. In the case of multi-component signal, blurring is observed by using GT and the extraction of closely spaced auto-components becomes difficult [62, 63].

2.2.1.4 Continuous Wavelet Transform (CWT)

It is also used in which Multi-Resolution Analysis (MRA) is performed. At high frequencies, MRA is designed to offer good time resolution but poor resolution in frequency, and vice versa in the case of low frequencies. The obvious drawback of CWT is that a signal can have long-lasting high-frequency components and low-frequency components of short duration as well. In such cases, STFT is a better

choice as compared to CWT [62–64]. Furthermore, it is impossible to read the amplitudes or spectral powers directly from the CWT spectrum due to variations in frequency resolution.

2.2.1.5 Wigner-Ville Distribution (WVD)

In the Wigner-Ville Distribution (WVD) auto-correlation method is used. WVD serves as a perfect signal analysis tool for mono-component signals and gives information about time and frequency localization. The main drawback of WVD is that in the case of a multi-component signal, it offers cross-terms (interference). A method to reduce cross terms is to suppress the oscillatory components by additional low-pass filtering in time and frequency. WVD is also used in LPI radar waveform recognition methods to obtain Time-Frequency (TF) images and further classification is done [19, 64–67].

2.2.1.6 Fractional Fourier Transform (FrFT)

It is used in many applications as a generalized version of FT. FrFT has recognized itself as an influential tool for investigating time-varying signals. If a multi-component signal is given, FrFT has the capability to segregate the signal components from the cross terms [68]. The rotation of the time-frequency plane is controlled by the parameter α having a value ranging from 0 to 2π. FrFT falls under the category of linear TFR. IT has shown to be less computationally extensive as compared to WVD and radon transform (RT) [19]. It is also used in LPI radar waveform recognition methods to obtain TF images and further classification is done based upon hierarchical Decision Tree (DT) [25].

2.2.1.7 Smooth Pseudo WVD (SPWVD)

The cross terms appearing in WVD need to be suppressed and this idea leads to the generalized version of TFRs also known as Cohen's Class. In SPWVD,

two separate Kernels are used for smoothing WVD in both time and frequency. The drawback of filtering is that the excellent resolution in time and frequency is distorted. SPWVD is not capable to separate closely placed signal components and more computations are required to find the optimal window length for frequency and time domain filtering [65, 66].

2.2.1.8 Gabor Wigner Transform (GWT)

The Gabor-Wigner transform is a technique for time-frequency analysis that reduces cross-term interference and provides a thorough representation of the time-varying frequency content of a signal by combining features of the Gabor transform and the Wigner-Ville distribution. GWT enjoys the benefits of both transforms (GT and WVD): excellent resolution in time and frequency due to WVD and the absence of cross terms due to GT. Due to the non-existence of cross terms in GT, the TFR of GT acts as a filter for filtering cross terms appearing at the output of WVD [65–67]. GWT can be used as a substitute for SPWVD to suppress the cross terms that may appear as noise or interference during analysis . It involves a combination of two TFRs so its computationally extensive.

2.2.1.9 Stockwell Transform (ST)

Basically, S Transform or Stockwell transform (ST) is an STFT using the Gaussian window whose length depends upon the frequency. As a result, varying resolution in time and frequency is obtained similar to the CWT. It shows similarity with CWT if Morlet wavelet is used as an analysis function. In contrast to the GT, the ST offers no cross-terms and thus better clarity of signal is achieved. The computational complexity of the fast ST algorithm is $O[Nlog(N)]$ [69–71].

2.2.1.10 Hilbert Haung Transform (HHT)

It is a nonlinear transform that is used for the analysis of non-stationary signals to extract information about their time and frequency contents. This method

involves two major steps: 1) Initially, a multi-component signal is decomposed into various AM or FM-modulated sine waves using Empirical Mode Decomposition (EMD) method. Demodulation is done and instantaneous frequency and amplitudes of sine waves are extracted. 2) Then the HHT is applied to obtain the time-frequency representation of sine waves. EMD seems to be effective and simple but as compared to SST mode reconstruction is not carried out in an appropriate mathematical framework [71–73].

2.2.1.11 The Choi-Williams Distribution (CWD)

It is a TFR that falls under the category of Cohen's Class. It shows similarity with WVD but the exponential kernel is used that acts as a 2D low pass filter and balances the cross terms appearing due to the presence of multiple components in a signal. Cross terms suppression also results in a high resolution of auto-terms. In LPI radar waveform recognition methods, CWD is used to obtain the TF image [74]. Feature extraction is performed that further leads to the classification of emitters having different intrapulse parameters. It offers better results but it's computationally extensive. In contrast to CWD, frequency reassignment (FR) method provides better visual representation and recognition accuracy is higher for polyphase codes [26, 75, 76].

2.2.1.12 Reassignment Method (RM)

It is used for non-stationary multi-component signals to sharpen their TFR without losing information about temporal localization. In this method, the value of any time-frequency point is obtained by computing the weighted sum of its nearby points in TFR. This averaging may result in cross-term suppression but at the cost of the disturbing location of auto-terms. RM involves the reassignment of coefficients in both time and frequency that allows perfect localization of linear chirps. Instantaneous frequency and group delay are computed to obtain the centroid of distribution. RM then moves the value of the spectrogram towards the centroid [77–80].

2.2.1.13 Synchrosqueezing Transform (SST)

It is a type of reassignment method that sharpens the TFR and is used to separate the components of a multi-component signal. SST differs from EMD in the sense that mode reconstruction is done using an appropriate mathematical background. SST offers dual benefits: It enhances the resolution of auto-components by sharpening the TFR. Additionally, different modes in a multi-component signal can be separated and demodulated. FSST can also be used to estimate the phases when exact phase information is not available [81]. STFT is computed and then the transform values are squeezed so that they concentrate around curves of Instantaneous Frequency (IF) in the time-frequency plane [82–84].

2.2.2 Summary of TFRs

TFRs are compared in terms of different performance measures including multi-component analysis, phase estimation, computational complexity, resolution, cross terms, etc., and are given in Table 2.2.2. In LPI radar waveform recognition techniques, it is very important to choose the appropriate TFR capable of resolving multi-component signals with low computational complexity and high resolution. Phase information is necessary to identify the phase-coded waveforms. Cross-term reduction is also very important because it appears as interference and also limits the resolution of auto-components. Among the linear TFRs, CWT has more computational complexity than STFT, making it hard to directly read the spectral components from its output. While the Gabor transform has a higher resolution than the STFT, there is blurring in the presence of multi-components. Among the quadratic TFRs: CWD, RM, and FSST are observed to be better in terms of performance measures discussed above but they are computationally extensive. In RM, the modes retrieval method is not straightforward as compared to FSST. According to the literature review mentioned above, STFT is discovered to be capable of satisfying the aforementioned requirements for the online recognition of phase-coded waveforms in low SNR environments.

Literature Survey of TFRs

Techniques	Features	Multi-Comp.	Comp. Complexity	Cross Terms	Phase	Resolution	Cons
1. STFT [22, 59–61]	1.Used for non-stationary signals 2.Most widely used, easy interpretation and fast implementation 3.Fixed TF resolution	Not good	Low	No	Yes	Limited	1.Limited and fixed TF resolution 2.Computations required for optimal window length
2. CWT [62–64]	1.Multi-Resolution Analysis (MRA) 2.Gives good TF resolution at high frequencies and vice versa for lower frequencies	Not good	High	No	No	Variable (frequency dependent)	1.Variable TF resolution 2.Impossible to read spectral amplitudes directly from a wavelet spectrum
3. Gabor [62, 63]	1.Variant of STFT with the Gaussian window function 2.Offers better TF resolution than STFT	Not good	Low	No	No	Better than STFT	1.Computations required for optimal length 2.Blurring is observed for multi-components
4. WVD [19, 64–67]	1.Uses an auto-correlation approach to overcome limited resolution of STFT 2.Best energy concentration for LFM signals is observed	Not good	High	Yes	No (Use Cross WVD)	High	1.Cross terms (for multiple quadratic components) 2.Additional low-pass filtering required for cross terms suppression

Techniques	Features	Multi-Comp.	Comp. Complexity	Cross Terms	Phase	Resolution	Cons
5. SPWVD [65, 66]	1.It's a WVD, filtered by two separate kernels. 2. The kernels smooth the WVD in frequency and time	Good	High	Reduced	No	Degraded resolution than WVD	1.Degraded resolution of auto-components 2.Proper selection of windows for time & frequency filtering 3.It can't separates closely placed signal components
6. GW [65–67]	1.Combination of GT and WVD 2.Excellent TF properties (WVD) and lack of cross-terms (GT)	Good	high	Almost eliminated	No	High	1.Computationally extensive
7. ST [70, 71]	1.Generalized STFT with frequency dependant Gaussian window 2.Low frequency comps have good freq resolution and vice versa for high freq comps	Good	Low	No	No	Better than STFT (frequency dependent)	1.Clarity is worse than WVD
8. EMD & HHT [71–73]	1.Initially, the Signal is decomposed into a sum of AM/FM sine waves using an EMD approach 2.The IA and IF of each sine wave can be extracted using analytical signal 3.Finally, TF representation is obtained by using HHT	Good	Lower (than CWT)	No	No	Low	1.Separation of components with close Instantaneous Angular Freq. (IAF) is a common problem

Techniques	Features	Multi-Comp.	Comp. Complexity	Cross Terms	Phase	Resolution	Cons
9. CWD [26, 75, 76]	1.It's a WVD with an exponential kernel 2.Kernel balances cross terms and provide high resolution 3.Used in LPI waveform recognition methods	Good	High	Reduced	No	High	1.Better recognition accuracy is not achieved in case of phase-coded LPI radars waveforms
10. RM [77–80]	1.It aims to sharpen the TFR 2.Reassignment of spectrogram is done both in time and frequency domain	Good	High	No	No	V.High	1.No mode reconstruction technique using the RM is straightforward
11. FSST [81–84]	1.It combines IF estimation and TFR mapping into a complete TF transform 2.The coefficients are reassigned to STFT only for the frequency component 3.Better recognition accuracy is achieved in case of phase-coded waveforms in LPI radars as compared to CWD	Good	Lower than RM	No	No	V.High	1.Computationally extensive 2.It enables mode reconstruction when freqs. of multiple components are well separated
12. FrFT [19, 25, 68]	1.It is the generalization of FT 2.FrFT can be used for detection of cross terns in WVD 3.Can be used to isolate signal components from multi-component signal	Good	Low	No	No	ST-FrFT offers high resolution	1.It is useful to filter noise, but with the condition that it does not overlap with the desired signal in the TF domain

TABLE 2.2: Literature Survey of TFR

2.3 Deep Learning (DL) Techniques for Emitter Recognition

Machine learning and deep learning are the two technologies that are now trending the most. The combinations of these technologies are widely employed. Machine learning (ML) is the subset of Artificial Intelligence (AI) that gives a system the capability to learn from experience and get improve over time without being explicitly programmed.

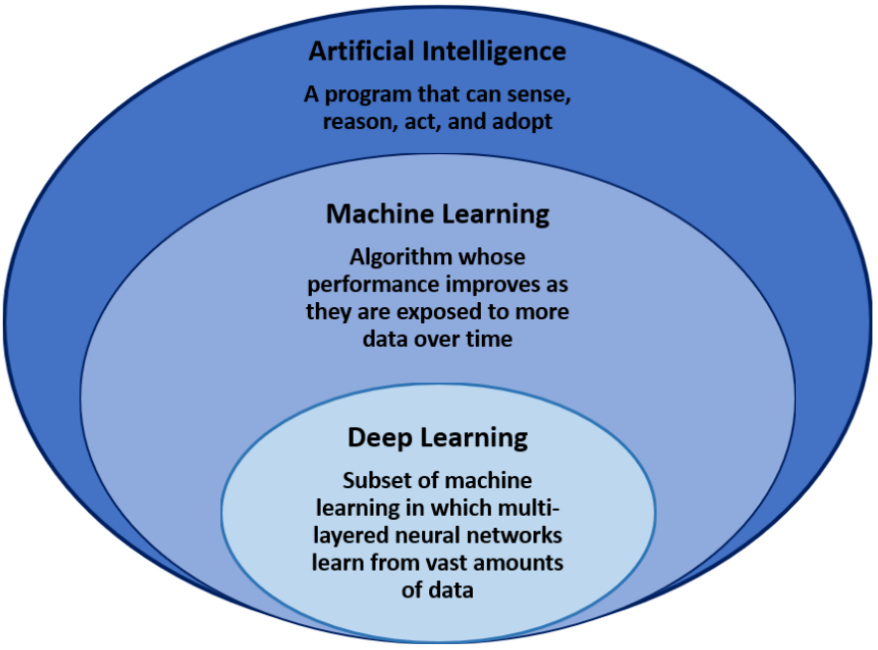

FIGURE 2.3: Relationship of AI and ML

2.3.1 Literature Survey of DL Techniques for Emitter Recognition

Some of the deep neural network (DNN) models used in the literature include:

1. Artificial Neural Networks (ANNs)[21–23, 29, 74]
2. Deep Belief Networks (DBNs) [85]

3. Convolutional Neural Networks (CNNs)[23, 27–29, 85]
4. Recurrent Neural Network (RNN) and [24, 85]
5. Long Short Term Memory (LSTM) [27, 29, 85]

Artificial Neural Networks (ANNs) and Recurrent Neural Networks (RNNs) are associated with deep learning, a subset of machine learning. The algorithms are developed in the same way as machine learning is done, however, there are many more levels of algorithms. Fig. 2.3 depicts the relationship between AI, ML, and DL.

2.3.1.1 Artificial Neural Network (ANN)

An ANN contains the set of neurons in a layer that is interconnected to neurons of the next layer. The weighted sum is computed at the neuron and then the activation function is applied. In ANN, forward propagation is done to obtain the predictions and network parameters (weights) are updated using the Back Propagation (BP) algorithm. Mean Squared Error (MSE) and cross-entropy cost functions are often used in the case of regression and classification, respectively. In ANN, the problems are presented to the network in terms of attributes. ANNs are used for handwriting recognition, prediction of a stock exchange, image compression, etc, and their architecture is shown in Fig. 2.4. In LPI radar waveform recognition methods, different DNNs have been used in the literature that gives better recognition accuracy under different SNR conditions [21–23, 29, 74].

2.3.1.2 Deep Belief Network (DBN)

DBN is a generative model that tries to find out the underlying data distribution using the Bayesian rule. DBN consists of several Restricted Boltzmann Machines (RBMs) that are stacked over each other. Each of them contains a single visible and a hidden layer. The hidden layer of the first RBM acts as a visible layer for the next one. The parameters of the network are then updated using the

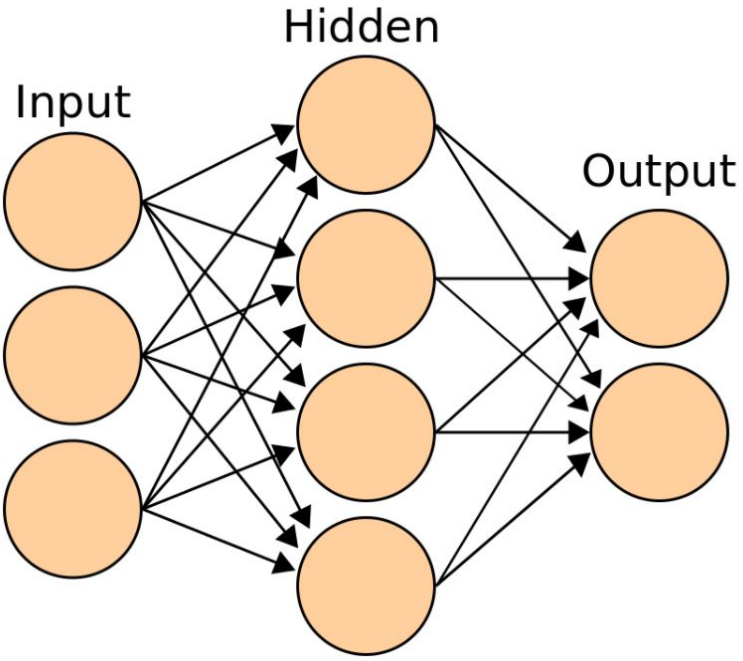

FIGURE 2.4: Artificial Neural Network (ANN) [86]

BP algorithm. Each layer is used to map different features in the training data [85]. They find applications in natural language processing, EEG, drug discovery, etc., and their architecture is shown in Fig. 2.5. In [22], DBN is used to classify the radar waveform modulation schemes, and Energy Cumulant (EC)-STFT is also used to obtain the TFR. DBN requires more time for pre-training and then fine-tuning network parameters is done.

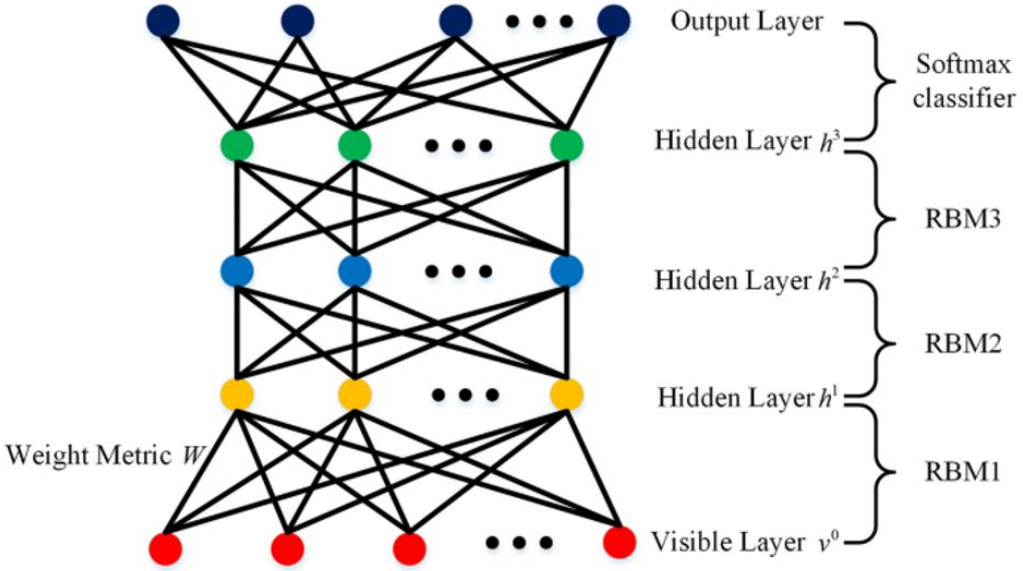

FIGURE 2.5: Deep Belief Network (DBN) [87]

2.3.1.3 Convolutional Neural Network (CNN)

One of the most widely used DL models used for image detection and classification problems is CNN [88]. It offers high accuracy, automatic feature extraction and gives better results as compared to other ML algorithms. CNN involves a convolutional layer where the filter weights are needed to be learned in addition to other network parameters using BP algorithm. The output of the Convolutional layer is fed to the pooling layer to reduce the dimensions. The output from pooling layers is then concatenated and fed to the dense layer to get the output. In CNN, the parameter sharing concept is used where the same filter is used to convolve with image pixels instead of finding weights for every individual pixel [85]. They are used for face and speech recognition, image and text classification, etc., and their architecture is shown in Fig. 2.6.

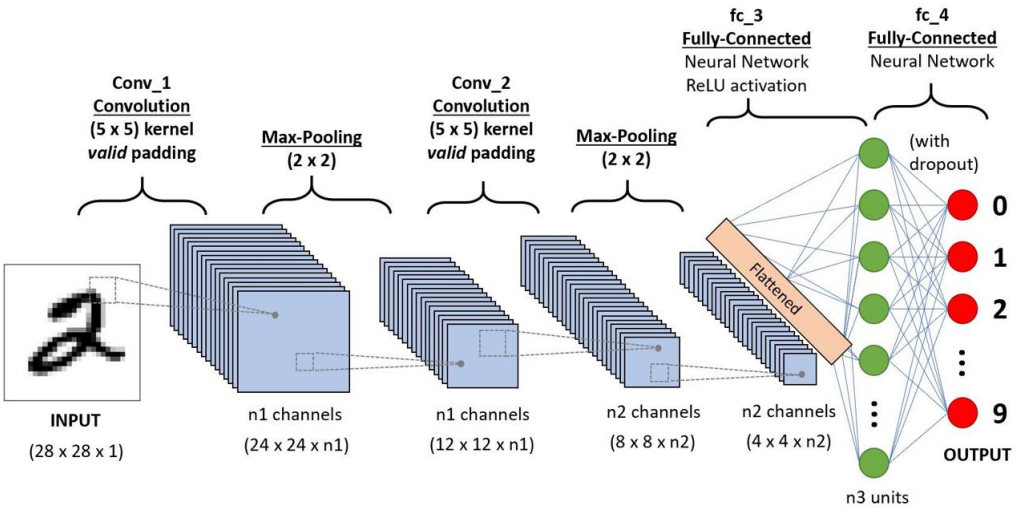

FIGURE 2.6: Convolutional Neural Network (CNN) [89]

In [23], CNN is used with SAT that shows robustness to noise and good recognition accuracy for intrapulse modulation schemes. A combined network containing CNN, LSTM, and DNN is also proposed in [27]. A novel emitter identification method based on PW images and CNN is proposed in [28] that outperforms the existing emitter identification techniques in the literature. In LPI radar waveform recognition methods, CNN is used with LSTM to provide good recognition accuracy [29].

2.3.1.4 Recurrent Neural Network (RNN)

RNN is very popular among Neural Networks (NNs) used for sequential data. In NN, no relationship exists between the current input and the past output. RNN network with the self-loop is used to resolve this issue. It is capable of capturing short-term time dependency in the given sequence using its internal state (memory). RNNs are also used for the classification, prediction, and deinterleaving of pulse streams received at RWRs [90]. RNNs are used for language modeling, sentiment classification, speech recognition, etc [85]. and its architecture is shown in Fig. 2.7.

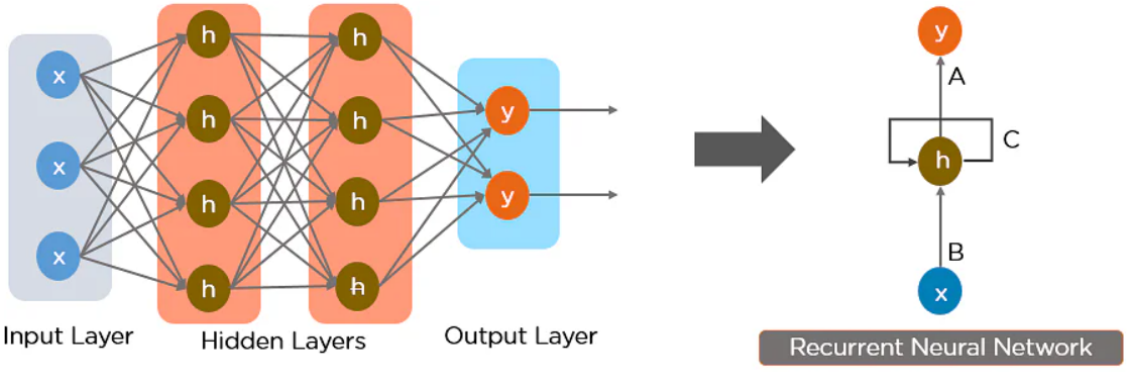

FIGURE 2.7: Recurrent Neural Network (RNN) [91]

In [24], RNN is proposed to solve problems of classification and denoising of pulse streams as it can mine the temporal patterns in the given pulse stream. In RNNs, there exists a problem of vanishing or exploding gradient. The information is carried by the gradient in RNN; the parameter update becomes less significant when the gradient value is very small. Similarly, the gradient may explode resulting in a large parameter update. Poor accuracy is observed and more training time is required in such cases.

2.3.1.5 Long Short-Term Memory Network (LSTM)

The Long Short-Term Memory (LSTM) network is a complicated RNN that permits information persistence. It is capable of resolving the RNN's vanishing gradient issue. The high-level LSTM operations are quite similar to those of an RNN

cell. LSTM first gained popularity in 2014 despite being introduced in 1997. Together with Gated Recurrent Units (GRU), they form the family of RNNs. In the field of Natural Language Processing (NLP) and for the classification of sequential data, LSTMs took the lead as the most advanced model when GPUs became widely available and the first deep learning frameworks emerged. As seen in Fig. 2.8, the LSTM is composed of three gates, each of which has a different function. The first gate decides whether data from the previous time step must be kept or can be discarded. The input gate is used by the cell to learn new information from the input. Finally, the cell uses an output gate to send the updated data from the current time step to the very next time step. LSTM is used in combination with other DNNs for radar emitter recognition problems [92]. A unique recognition method based on CNN-LSTM and STFT is provided in [29]. At an SNR of -2 dB, the proposed approach can identify eight different radar signals with an overall accuracy of 96%. It is suggested in [27] that a hybrid network based on a shallow CNN, LSTM, and DNN can identify six different radar emitter signals with SNRs ranging from -14 dB to 20 dB.

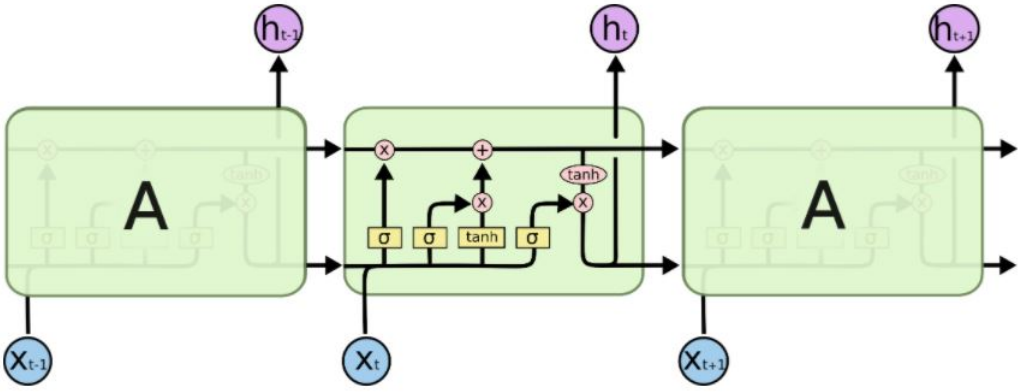

FIGURE 2.8: Long Short Term Memory (LSTM) Network [93]

2.3.2 Summary of DL Techniques

On the basis of the above literature survey, it is concluded that RNNs are considered suitable for sequential or time series data but the gradient can sometimes get too small or too large during training. As a result, in this condition, training an

RNN algorithm becomes quite challenging resulting in low accuracy, poor performance, and long training time. LSTM is utilized to solve this gradient exploding and vanishing problem. As LSTM incorporates gates that control information flow, there is little alteration in the existing information when the new one is added. The use of CNNs is driven by their ability to capture and learn relevant features from an image at several layers.Both of these architectures (BiLSTM and CNN) are selected for this research to test the efficacy of derived phase-based feature vectors. A brief literature survey of some DNNs is given in Table 2.5.

2.4 Gap Analysis

The comprehensive literature review emphasizes that the recognition of phase-coded LPI radar waveforms relies on extracting information from the magnitude spectrum of TFRs. Moreover, the recent research studies have considered the recognition with a minimum reported SNR of -10 dB. However, a unique phase spectrum-based approach is needed to improve recognition accuracy even in lower SNR situations, as phase serves as an important candidate for phase coded waveforms. Additionally, investigating the performance of Barker codes in emitter recognition is crucial. This investigation can assess their effectiveness as well as resistance to noise and interference that might be helpful for the emitter recognition at RWR.

2.5 Problem Statement

Phase-coded LPI radar waveform recognition using amplitude spectrum information from TFRs exhibits low accuracy in low SNR situations. There is a need to explore alternative methods for improved recognition in noisy environments and investigate the effectiveness of Barker codes for emitter recognition, assessing their performance against noise and interference.

Literature Survey of DL techniques

DNN	Input	Generative/ Discriminative	Cost Function	Parameter Estimation Algorithm	Prediction Algorithm	Model Complexity Reduction	Applications	Pros	Cons
1.ANN [21–23, 29, 74]	Features	Discriminative	1.Sum of squared error (regression) 2.Cross entropy (Classification)	BP (SGD is used)	Forward propagation	1.Reduce number of hidden layers 2.Regularization 3.Early stopping	Handwriting recognition, image compression, stock exchange prediction	1.Learning methods are robust to noise 2.Problems are presented by attribute-value pairs	1.Difficulty of showing problem to network 2.No automatic feature extraction
2.DBN [22, 85]	Features	Generative	Log likelihood	1.Contrastive divergence (CD) initializes the network weights 2.BP is done to tune the initialized weights	Forward propagation	1.Reduce the number of hidden layers 2.Reduce the number of neurons per layer 3.Pruning algorithms can be used	Natural language processing, Drug discovery, EEG	1.It is robust and stable even for imbalanced dataset	1.More training time required for pre-training and the tuning of network parameters
3.CNN [23, 27, 28, 85, 88]	Image, 1D data	Both	Cross Entropy	BP (ADAM)	Forward propagation	1.By using 1D data instead of images to reduce the kernel weights	face recognition, image classification, speech recognition, text classification	1.Automatic feature extraction 2.Highest accuracy among all algorithms that predicts images 3.Parameter Sharing	1.Training takes a lot of time if CNN has several layers 2.ConvNet requires a large dataset to train the network 3.Generally bad at handling rotation and scale-invariance

DNN	Input	Generative/ Discriminative	Cost Function	Parameter Estimation Algorithm	Prediction Algorithm	Model Complexity Reduction	Applications	Pros	Cons
4.RNN [24, 90]	Sequential data	Both	Cross entropy	BP	Forward pass in time	1.Number of hidden layers can be reduced 2.Time steps can be reduced	Prediction problems, Language modeling, Sentiment classification, video classification ,and speech recognition	1.Input of any length can be processed without increasing model size 2.Computations takes into account historical information 3.Weights are shared across time	1.Exploding or vanishing gradient 2.Training can be difficult 3.Can't cater long term dependence in data 4.No controlling knobs to control the flow of information across network
5.LSTM [29, 92, 94]	Sequential data	Both	MSE (prediction)	BP	Forward pass in time	1.Drop out LSTM cells to reduce overfitting 2.Number of hidden layers can be reduced 3.Use truncated BPTT	Robot control, time series prediction, speech recognition, rhythm learning, handwriting recognition,etc	1.Can cater long term dependencies 2.LSTM has controlling knobs to control flow of information 3.Can deal with vanishing gradient problem	1.More complexity and operating cost

TABLE 2.3: Literature Survey of DL Techniques

2.6 The Proposed Research Methodology

We have categorized our methodology into three main sections to address the highlighted research issues: Signals Generation, Feature Extraction, and Recognition of phase-coded waveforms using deep learning architectures. Initially, waveform generation using different phase-coded modulation schemes (Barker, Frank, P1, P2, P3, and P4) is done using MATLAB, and baseline simulations are obtained. In the real world, some known emitters can be considered with possible modulation schemes to simulate the training data. Additive White Gaussian Noise (AWGN) is added to the signals for SNR ranging from -16 dB to 8 dB with a step-size of 2 dB to create the data sets for testing and training of deep learning architectures.

In the second part of the research, we aim to design a specific phase-based feature vector/matrix for phase-coded waveforms to analyze them at different SNR values ranging from -16 dB to 8 dB as discussed in Chapter 3. The problem statement states that in order to improve the recognition accuracy for phase-coded LPI radar waveforms, a novel feature vector or matrix based on phase-related information is generated utilizing the phase spectrum of STFT.

The efficacy of derived phase-based feature vectors/matrices is tested for different phase-coded waveforms in the third step. BiLSTM network and deep CNN architectures are chosen based on an extensive literature survey of deep learning techniques given in Chapter 2. Both architectures employ the same data sets and are thoroughly explained in Chapter 3 along with their parameters. In comparison to deep CNN architecture, the SNR values for BiLSTM architecture range from -8 dB to 8 dB. For the deep CNN architecture, the SNR values vary from -16 dB to 8 dB. The optimal training parameters for both architectures are given in Chapter 4 of the dissertation followed by the recognition results. The final goal of this research is to compare the recognition results of phase-coded waveforms obtained from both architectures so the best one can be used for our application. The recognition accuracies obtained from both the architectures (DCNN and BiLSTM) will be compared and the results will be discussed in the simulation part of the dissertation. Fig. 2.9 shows the overall proposed methodology in detail.

2.7 Contributions

The following points describe the main contribution of this work, to the best of our understanding and comparison with certain previous research works:

1. We propose the feature extraction method using the phase spectrum of STFT that yields high recognition accuracies of phase-coded waveforms instead of the magnitude spectrum of TFRs used by state-of-the-art techniques in the literature.

2. We analyze the performance of the derived phase-based features using deep learning architectures (BiLSTM & DCNN).

3. We evaluate the accuracy of phase-coded waveforms at a low SNR level of -16 dB whereas, in other works reasonable accuracies are observed at SNR$\geq$ -10 dB. The purpose of the simulations is to evaluate the performance of the proposed emitter recognition technology and compare it with that of other existing techniques in the literature.

4. The above contributions have been published and submitted in these research works respectively [16, 41].

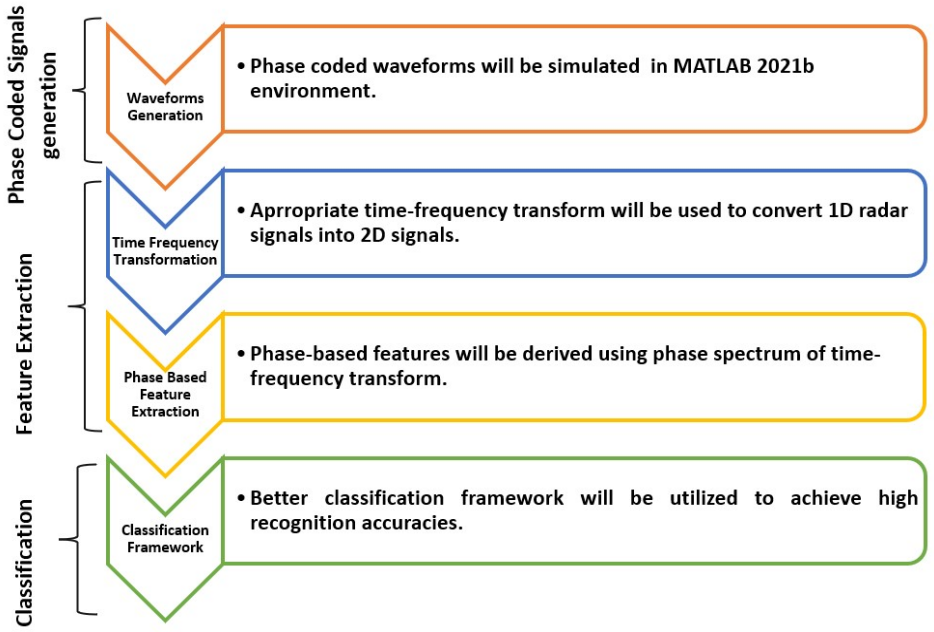

FIGURE 2.9: Proposed Methodology

2.8 Chapter Summary

This chapter begins with a thorough review of the literature on radar emitter recognition methods before comparing TFRs that are used to transform 1D radar signals into a 2D format for phase-based feature extraction. Additionally, many deep learning methods are compared using a variety of parameters to determine which is best for our simulations. A literature survey helps to create a gap analysis, which is then followed by a problem statement and dissertation contributions. The next chapter highlights the main contribution of this research work and explains the phase-based feature extraction method in detail.

Chapter 3

Proposed Solution

The function of an end-to-end Electronic Warfare (EW) system including the interception of threat signals at Radar Warning Receiver (RWR) has been discussed in the Section 3.1. Once the signals are intercepted at RWR, the novel phase spectrum-based feature extraction method employing STFT is performed as discussed in Section 3.2. The detailed steps for 1D and 2D phase-based feature extraction for BiLSTM and DCNN architectures are provided in Sections 3.3 and 3.4, respectively. The two proposed deep learning architectures used to assess the efficacy of the novel phase-based feature extraction method are presented in the Section 3.5, which is followed by a summary of the chapter.

3.1 End-to-End EW System

In order to defend friendly forces against enemy electronic threats, EW systems are an essential part of modern military operations. Its main objectives are to identify, interfere with, and protect against adversary's electronic, radar, and communication equipment. The RWR, a crucial component of EW systems, is responsible for analyzing and identifying the emissions from different hostile emitters present in the environment. Radar signals from possible threats, such as hostile aircrafts, ships, or ground-based radar systems, must be intercepted and recognized by the

RWR. Radar emissions can have their frequency, modulation, pulse-widths, and other parameters analyzed by the RWR. The recognition of the kind of hostile radar system generating the signals is made easier by this method. An end-to-end EW system for intercepting and recognizing different phase-coded radar waveforms emitted by LPI threat emitters is described below:

3.1.1 Waveform Generation

The first step involves the generation of phase-coded waveforms by LPI radars including Barker, Frank, and Polyphase codes (P1, P2, P3, P4). Different type of threat emitters (LPI radars) can generate waveforms using these phase-coding schemes. The purpose of the intended research is to identify these threat emitters based on their intra-pulse modulation schemes.

3.1.2 Transmitter

The function of transmitter is to send out the modulated signals in the EW environment using the antenna. In this research work, the assumption is made that all the threat emitters will be using the same carrier frequency of 50 MHz. The transmitter has high bandwidth and power and should create low-noise transmissions. Target tracking, range measurement, and surveillance are made possible by radar systems owing to the transmitter's ability to illuminate and detect targets in conjunction with the radar antenna.

3.1.3 Duplexer

A duplexer controls when signals are sent into the EW environment by functioning as an on/off switch. In order to reduce the probability of detection, this control is crucial for controlling the transmission of LPI radar signals. It guarantees that the same antenna can be utilized for both purposes and guards against the high-power broadcast signal harming the receiver. Duplexers are often designed using

RF switches or circulators to route signals appropriately, enabling seamless radar operation.

3.1.4 Antenna

The radar antenna helps with signal transmission and reception, which enables the radar system to identify and track targets, compute their range, velocity, and direction, and carry out a number of other radar functions like air traffic control, meteorological tracking, and military surveillance.

3.1.5 EM Environment

The emitted signals in the EW environment are exposed to noise and interference from the outside environment. Additive White Gaussian Noise (AWGN) is used in this research to imitate the noise and interference that are commonly found in the real world.

3.1.6 Signal Interception

The signals from various threat emitters are intercepted at RWR. These signals will be analyzed to identify their intrapulse modulation schemes that might be helpful for EA system to generate the attack against hostile emitters.

3.1.7 Parameter Estimation

For the purpose of analysis, the carrier frequency (F_c) of the signal is identified once it is intercepted at RWR. The computed carrier frequency will be helpful to determine the row in phase spectrum of time-frequency transform that will correspond to phase pattern of a particular phase-coded signal. The details about this are given in the next section. If the (F_c) changes then the corresponding row

in the phase spectrum will also change. The other parameters of emitters can also be estimated based on the requirements.

3.1.8 Time Frequency Transformation

Short Time Fourier Transform (STFT) is used to transform 1D radar signal into 2D for further analysis. STFT has the fast and simple implementations and a suitable window size is required to get the good resolution. The computed window size will have an impact on the analysis's resolution. The steps involved for finding suitable window size are discussed in the next section. For the intercepted signals, the STFT is calculated window-wise. Every window gives a representation of the signal's frequency components during that interval by recording a portion of the signal across time.

3.1.9 Feature Extraction

The phase-based features are extracted from the STFT representation. These features have the ability to record signal phase properties, which are crucial for identifying among various LPI radar phase-coded waveforms as phase is an important candidate for their recognition.

3.1.10 Deep Learning Architectures

We have used two deep learning architectures for waveform recognition: Deep Convolutional Neural Network (DCNN) and Bidirectional Long Short-Term Memory (BiLSTM). In order to classify the phase-coded waveforms, these architectures are trained using the phase-based features and trained networks are then used to classify the phase-coded waveforms. BiLSTM will be given 1D phase-based features as compared to DCNN that performs well on 2D data (images). In some cases, hybrid architectures may be used to leverage the strengths of both approaches. At the end, the recognition accuracies of both the architectures will be compared.

3.1.11 Comparison of Recognition Accuracies

A comparison is made between the recognition accuracies obtained from both the BiLSTM and DCNN architectures. This comparison will aid in assessing how well the deep learning models categorize LPI radar threat emitters. The recognition of the various phase-coded radar waveforms involves the signal generation, transmission, reception, and signal processing techniques are involved throughout the entire process. EW system rely on automated and data-driven waveform recognition, made possible by deep learning models such as BiLSTM and DCNN, to detect possible threats. The most suitable model for the task is selected with the help of a comparison of recognition accuracies. The information obtained from the deep learning architectures can be sent to ESM or EA to generate the attack against the threat emitters. The end-to-end block diagram of the whole method is shown in Fig. 3.1.

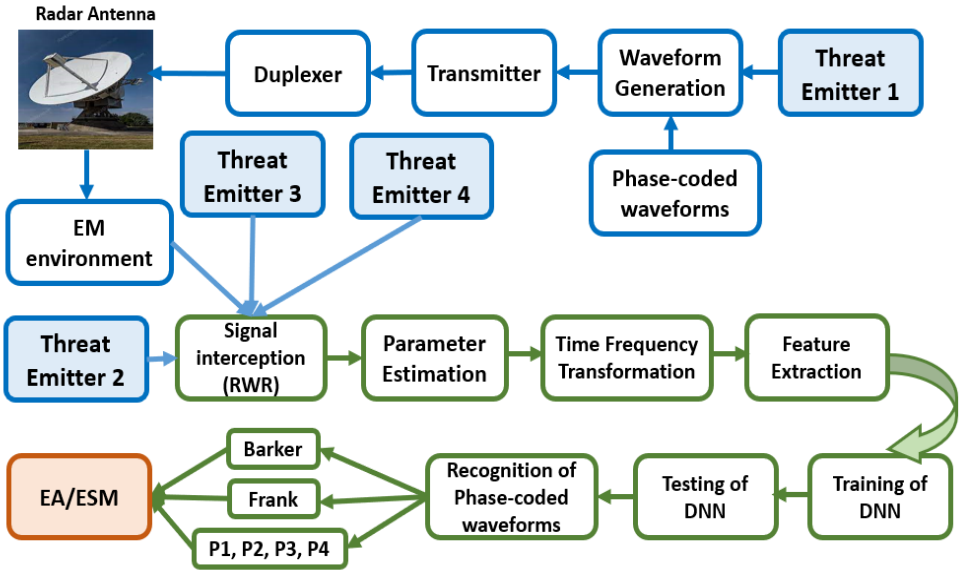

FIGURE 3.1: End-to-End EW System

3.2 Feature Extraction

The significance of using feature extraction techniques lies in their ability to transform raw data into a reduced, meaningful representation that captures the essential

information required for a specific task. In various fields, such as machine learning, pattern recognition, and signal processing, feature extraction plays a crucial role in enhancing performance and reducing computational complexity. By selecting relevant features and discarding irrelevant or redundant information, feature extraction reduces the dimensionality of data, which can lead to faster and more efficient processing. It also helps to mitigate the "curse of dimensionality," a challenge that arises when dealing with high-dimensional data, by improving model generalization and reducing overfitting. [95]. Feature extraction techniques can also lead to other types of advantages such as:

1. Improvement in accuracy.
2. Reduction of overfitting risk.
3. Acceleration of training process.
4. Enhancement of data visualization.

Overall, feature extraction is a powerful tool that enhances data analysis and pattern recognition tasks by transforming complex data into a more manageable and informative representation [96].

3.2.1 Feature Extraction Using STFT

In this work, a novel phase-based feature extraction is presented using STFT. The signal's time-varying characteristics are unfortunately not resolved by the Fourier Transform (FT). In order to solve the problem of time resolution, it is straightforward and obvious to segment the data, taper each segment using the appropriate window function, and then estimate the power spectrum for each windowed segment. This process is known as STFT. It has benefits over FT in that it may be used to examine non-stationary signals and provide information on the temporal localization of spectral components. Assuming that the signals are quasi-stationary inside each window, the stationary requirement is approximately satisfied. The problem is that choosing the window size is not so easy.

The most widely used, easy-to-understand, and quickly implemented technique is STFT [21, 97, 98]. The standard FT provides frequency information averaged across the whole signal time interval, but the STFT provides time-localized frequency information when a signal's frequency components fluctuate over time. The resolution of time and frequency can be a trade-off in STFT. In other words, a narrow-width window produces better resolution in the time domain but less resolution in the frequency domain, and vice versa. The output of the STFT is typically visualized using the spectrogram, which is an intensity map of the STFT magnitude with time. STFT can be expressed as the following relation:

$$X(m,\omega) = \sum_{n=-\infty}^{\infty} x[n]\omega[n-m]e^{-j\omega n} \tag{3.1}$$

In this case, the window utilized to calculate STFT is $w[n]$, and $x[n]$ is the signal. In the literature [26, 29, 34, 40], feature extraction is often performed using magnitude spectrum of TFR as opposed to the phase values employed in this study. The phase-based features will ultimately be given at the input of Deep Neural Networks (DNNs) for classification. The transmission side of the phase-coded waveform deliberately introduces phase offset. The EW receiver finally captures this waveform. Its goal is to measure the phase offsets that the emitter injected into the intercepted waveform during phase coding. These measured offsets will assist in determining the emitter's unidentified phase coding method. The next sub-section describes a unique phase-based feature extraction technique based on the STFT.

3.2.2 Optimal Window Size for STFT

The ideal window size will vary depending on the application. The size of window can be reduced if the application requires more precise time domain information. On the other hand, the size of the window should be increased if the application requires more precise frequency domain information. The two domains (time and frequency) cannot simultaneously have perfect resolutions. In the time and

frequency domains, we can achieve perfect resolution in only one domain at the expense of zero resolution in the other, or we can achieve intermediate resolution in both domains.

The most challenging aspect of the interpretation of the phase features of STFT is determining the optimal window size. In order to guarantee that the phase offset of each sub-pulse is preserved, it is crucial that the window of data samples utilized for phase offset calculation be short enough. The carrier must finish its one cycle within the optimal window size to obtain more exact phase information. Since the sub-pulse often lasts longer than a carrier cycle, the phase offset is constant throughout the measured window. The number of Fast Fourier Transform (FFT) points and window length (samples) are both same for STFT calculations. The calculations for finding the optimal window size of STFT are given in the next section.

Many deep learning algorithms use different feature formats as inputs, such as RNN, BiLSTM, and Gated Recurrent Unit (GRU), which need sequential data to be transformed into numerous 1D feature vectors. Similarly, DCNN can outperform the other deep learning algorithms if 2D data is provided at its input. The effectiveness of the suggested phase-based feature extraction method is assessed in this research work using two deep learning algorithms (BiLSTM & DCNN).

3.3 1D Phase Based Feature Extraction Method for BiLSTM Network

In this study, two deep learning architectures are used to evaluate the efficacy of the proposed phase-based feature extraction technique. The 1D phase-based feature extraction method is described in detail in this section.The BiLSTM architecture ultimately performs the phase-coded waveform recognition using the extracted 1D phase-based features as the input. The input will pass through the hidden layers

to produce the final output. BiLSTM is intended to perform well on sequential data.

3.3.1 Steps for 1D Phase Based Feature Extraction Method

The flowchart in Fig. 3.2 shows the detailed algorithm for 1D phase-based feature extraction used for BiLSTM architecture. The detection problem and recognition problem are the two primary sections of the proposed BiLSTM-based recognition method. The steps listed below are used in the detection problem to calculate the carrier frequency (Fc) of the intercepted noisy signal:

a. Detection Problem

1. The formulas provided in Section 1.7.5 are used to simulate the six different types of phase-coded LPI radar waveforms with SNR levels ranging from -8 dB to 8 dB.

2. The simulated waveforms are split into training and testing data sets to train and evaluate the effectiveness of the suggested architecture.

3. At the RWR receiver, the modulated discrete signal corrupted by Additive White Gaussian Noise (AWGN) is intercepted and its FFT is computed.

4. The absolute value of the FFT result is calculated and the frequency (F_c) that corresponds to the maximum value is then identified.

5. The reciprocal of F_c is calculated to determine the time (T_c) needed by the carrier to complete one cycle:

$$T_c = \frac{1}{F_c}. \tag{3.2}$$

6. The window size in terms of samples is calculated by multiplying (T_c) by a sampling frequency (F_s). T_s represents the sampling time.

$$window\ (samples) = T_c \times F_s \tag{3.3}$$

$$window\ (time) = T_s \times window\ (samples) \tag{3.4}$$

b. Recognition Problem

The recognition problem, which involves the following stages, is encountered after calculating the F_c and optimal window size. The steps involved in the recognition problem are as follows:

1. The window is initially slid over the signal and the output contains a column vector with the length equal to the number of FFT points.
2. The largest value is chosen from the column acquired in the previous step, and its phase is computed that corresponds to the carrier frequency signal's phase offset.
3. The STFT is ultimately computed window-wise after the window has been moved along the complete duration of a signal.
4. The phase value received from each window is stored in a pre-initialized vector in order to create a phase-based feature vector for each corresponding signal.
5. Furthermore, the feature vector is offered to the BiLSTM network as an input for recognition purpose.
6. The efficacy of the trained BiLSTM network is assessed by utilizing the testing data set containing signals of varying SNRs ranging from -8 dB to 8 dB.
7. The improvement in recognition accuracy of the phase-coded waveform is observed considering the recognition accuracies versus SNRs.

   Fig. 3.2 depicts the flowchart detailing the specific procedures for the phase-based feature extraction technique for BiLSTM network. Once the phase-based features are obtained they are ultimately given at the input of BiLSTM architecture for recognition of phase-coded waveforms.

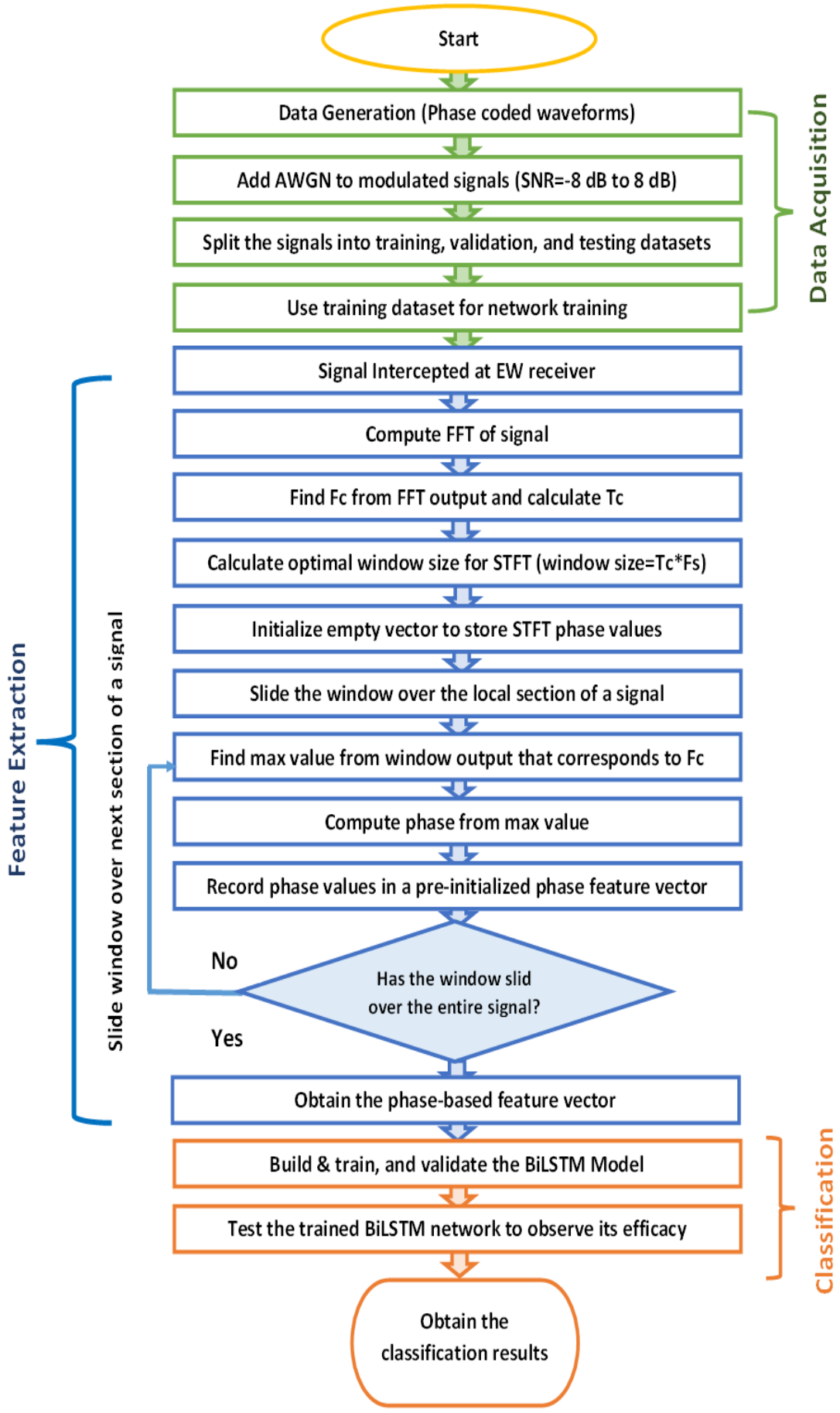

FIGURE 3.2: Flowchart of Phase-based Feature Extraction Algorithm for BiLSTM Network

3.3.2 Phase Feature Plots for BiLSTM Network

In this section, the phase features obtained using the suggested method for particular phase-coded signals at various SNR levels are displayed. Although the phase values recovered using the suggested method are noisy, they are very similar to those of benchmark signals. The signal length (ns) is displayed on the x-axis, and phase values (degree) are displayed on the y-axis.

In Fig. 3.3(a), the phase values of the actual Barker Code (Length= 13) without AWGN are displayed, which acts as a benchmark. The phase is 0° from 0 μs till 5 μs and 180° for 5 μs through 7 μs. From 7 μs to 9 μs, it switches to 0°, its 180° for 9 μs till 10 μs, 0° for 10 μs till 11 μs, 180° for 11 μs till 12 μs, and 0° for 12 μs till 13 μs. The Barker code's extracted phase feature vectors are shown in Fig. 3.3(b) through Fig. 3.3(f) for the corresponding SNR values of 4 dB, 2 dB, 0 dB, -2 dB, and -4 dB. The phase variations of the retrieved Barker code features are very similar to those of the benchmark code but are noisy. The phase of the STFT output is determined using the tangent inverse. Since the period of the tangent is π, wrapping occurs whenever noise causes the phase value to exceed 180° on both the positive and negative sides.

The retrieved phase values of the Frank code at various SNRs are compared to the corresponding benchmark Frank code (L= 4) and are displayed in Fig. 3.4(b) through Fig. 3.4(f). Fig. 3.4(a) acts as a benchmark and displays the phase values of the actual Frank Code (L=4, M=16) without AWGN. The overall length of the signal is 16 μs. From 0 μs till 5 μs, the phase is 0°, and from 5 μs till 6 μs, it shifts to 90°. It switches to 180° from 6 μs through 7 μs, and from 7 μs through 8 μs, it changes to -90°. It is 0° from 8 μs till 9 μs, shifts to 180° from 9 μs till 10 μs, then back to 0° from 10 μs to 11 μs. The phase is 180° again for 11 μs till 12 μs, its 0° for next 1 μs. It changes again to -90° from 13 μs till 14 μs, remains 180° for next 1 μs and then shifts to next 90° 15 μs till 16 μs. The phase values for the entire signal of length 16 μs in Fig. 3.4(a) are compared with those of derived phase features at different SNRs shown in plots from Fig. 3.4(b) till Fig. 3.4(f). The extracted features at low SNR values are noisy but still they resemble a lot

with the benchmark signal showing the efficacy of the proposed feature extraction technique. Similar comparisons are made between the P1 code's derived phases at various SNRs and the accompanying benchmark P1 code (L=4, M=16) are shown in Fig. 3.5(b) through Fig. 3.5(f). As a reference signal, Fig. 3.5(a) shows the phase values of the real P1 code without AWGN. The signal's pulse width is 8 μs and contains 16 sub-pulses (M=16). The phase is 0° from 0 μs till 1 μs, changes to -135° from 1 μs till 2 μs, and it shifts to 90° for next 1 μs. It switches to -45° from 3 μs through 4 μs, and from 4 μs through 5 μs, it changes to -180°. It is 135° from 5 μs till 6 μs, shifts to 90° from 6 μs till 7 μs, then changes to about 45° from 7 μs to 8 μs. The phase is 0° for 8 μs till 9 μs. From 9 μs till 12 μs, the phase values are mirror images of the phases of previous sub-pulses. The phase shifts to 180° from 12 μs to 13 μs, again its close to -45° for 1 μs, shifts to 90°, and then back to -135° for last sub-pulse. The benchmark signal is very similar to the derived features even though they are noisy at low SNR levels, demonstrating the effectiveness of the proposed feature extraction technique. Similarly, the benchmark P2 code (L= 6), P3 code (N= 12), and P4 code (N= 15) are compared to their respective phase-based feature plots derived at different SNRs in Fig. 3.6(b) through Fig. 3.6(f), Fig. 3.7(b) through Fig. 3.7(f), and Fig. 3.8(b) till Fig. 3.8(f) respectively.

3.4 2D Phase Based Feature Extraction Method for DCNN

The 2D phase-based feature extraction method is covered in detail in this section. By providing the DCNN architecture the 2D phase-based features as input, it can recognize the phase-coded waveforms.

3.4.1 Steps for 2D Phase Based Feature Extraction Method

The detailed procedure for 2D phase-based feature extraction for deep CNN (DCNN) architecture is split into two sections and is explained below.

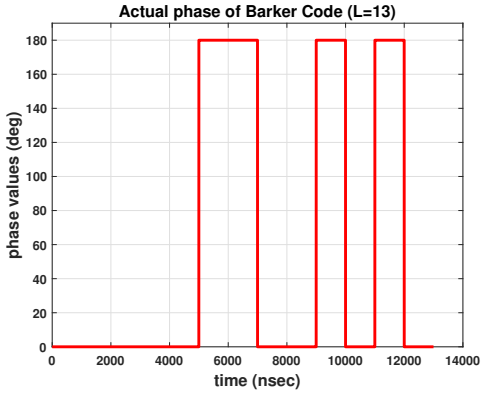

(a) Barker Code (L=13)

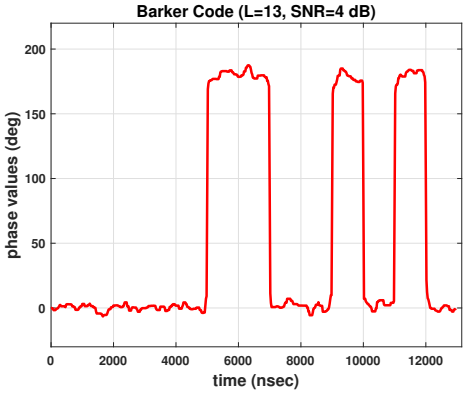

(b) Barker Code (L=13, SNR=4 dB)

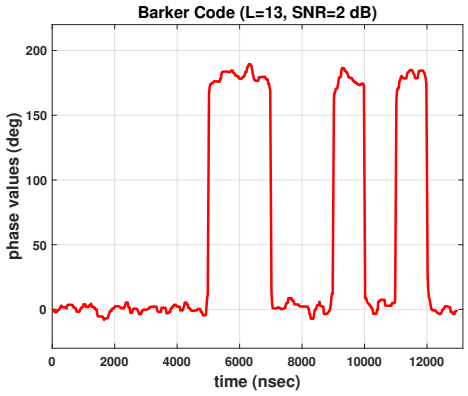

(c) Barker Code (L=13, SNR=2 dB)

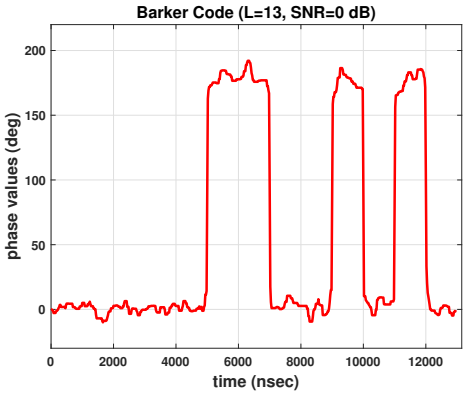

(d) Barker Code (L=13, SNR=0 dB)

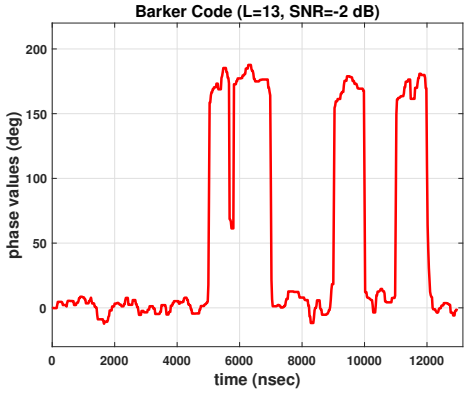

(e) Barker Code (L=13, SNR=-2 dB)

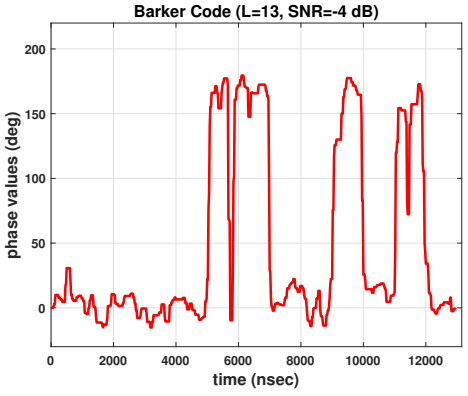

(f) Barker Code (L=13, SNR=-4 dB)

FIGURE 3.3: Phase Feature Plots of Barker Code (Order=13) at different SNRs

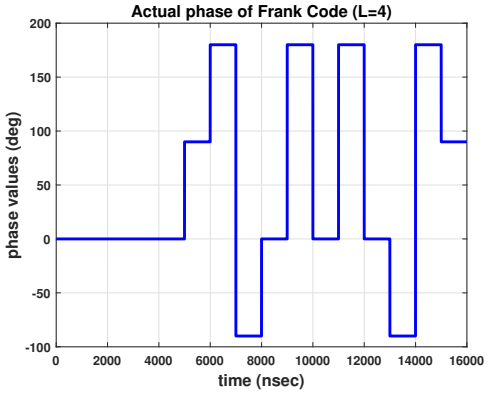

(a) Frank Code (L=4)

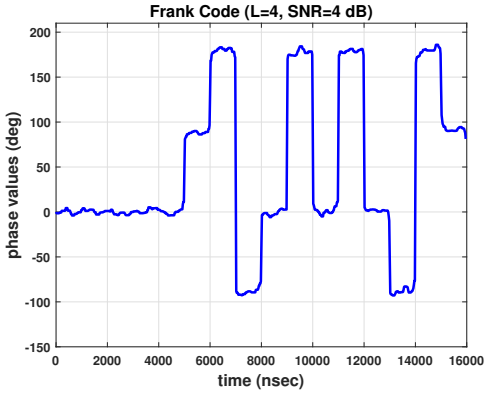

(b) Frank Code (L=4, SNR=4 dB)

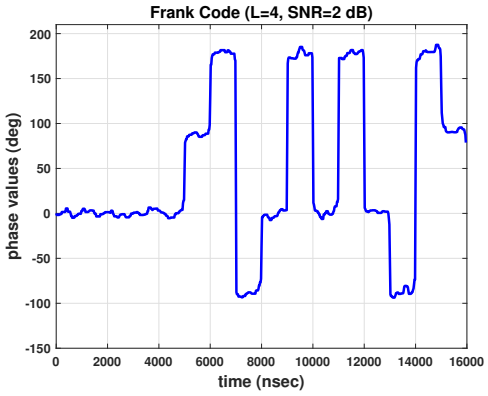

(c) Frank Code (L=4, SNR=2 dB)

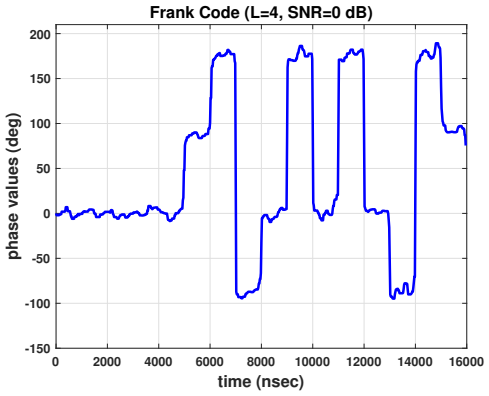

(d) Frank Code (L=4, SNR=0 dB)

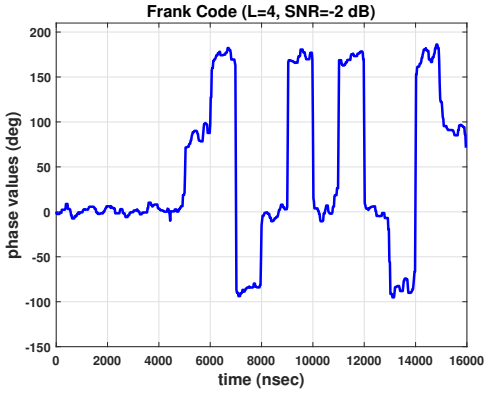

(e) Frank Code (L=4, SNR=-2 dB)

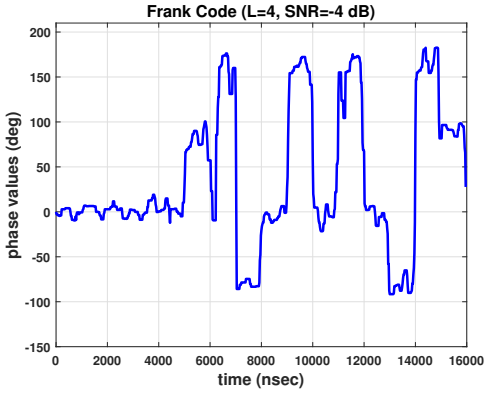

(f) Frank Code (L=4, SNR=-4 dB)

FIGURE 3.4: Phase Feature Plots of Frank Code (L=4) at different SNRs

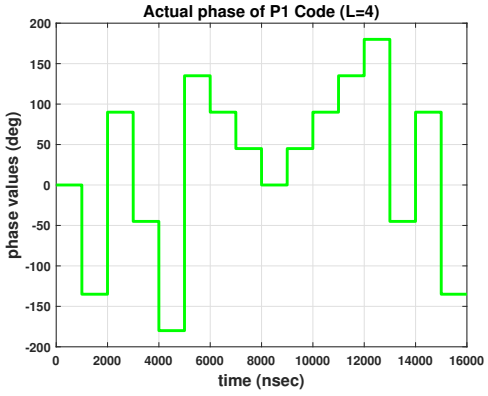

(a) P1 Code (L=4)

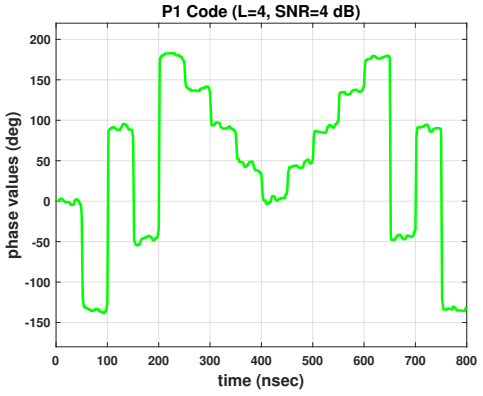

(b) P1 Code (L=4, SNR=4 dB)

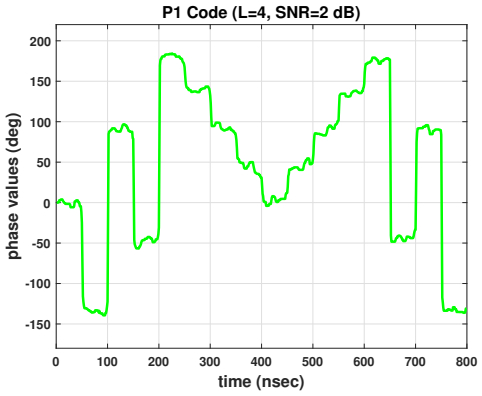

(c) P1 Code (L=4, SNR=2 dB)

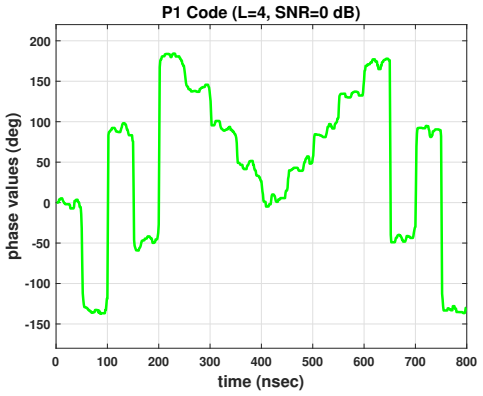

(d) P1 Code (L=4, SNR=0 dB)

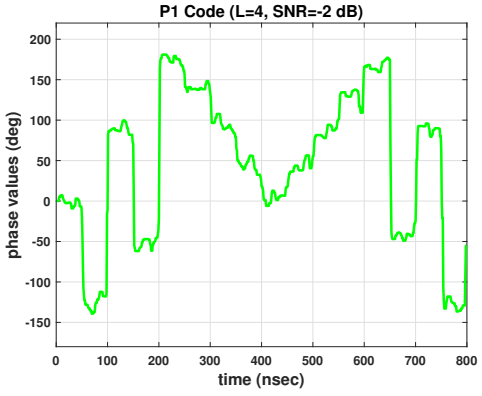

(e) P1 Code (L=4, SNR=-2 dB)

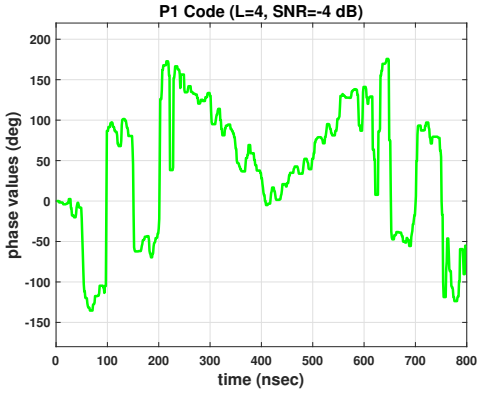

(f) P1 Code (L=4, SNR=-4 dB)

FIGURE 3.5: Phase Feature Plots of P1 Code (L=4) at different SNRs

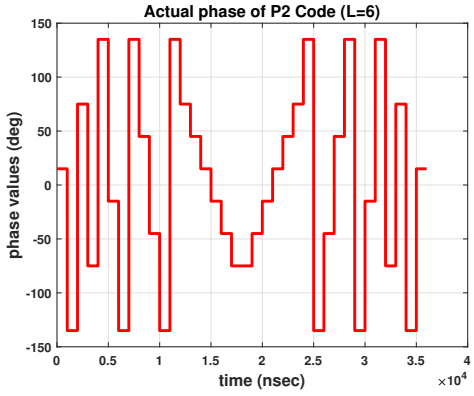

(a) P2 Code (L=6)

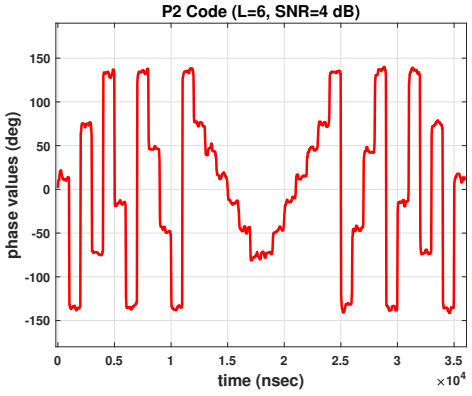

(b) P2 Code (L=6, SNR=4 dB)

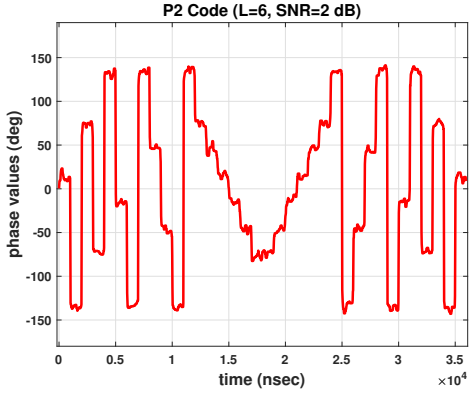

(c) P2 Code (L=6, SNR=2 dB)

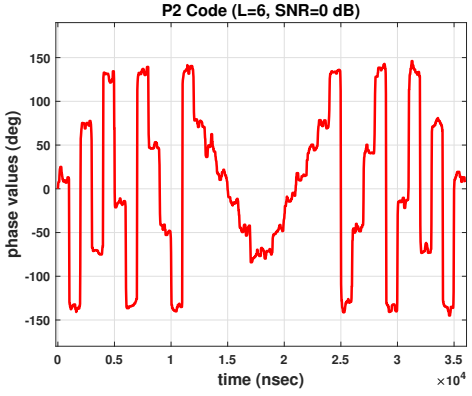

(d) P2 Code (L=6, SNR=0 dB)

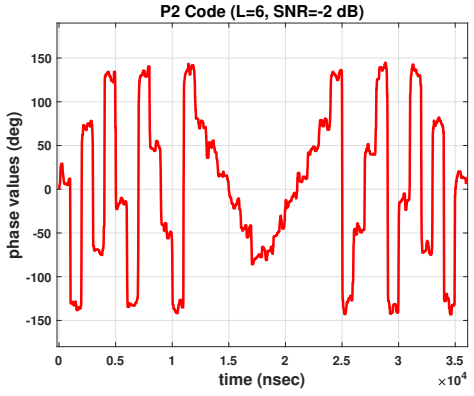

(e) P2 Code (L=6, SNR=-2 dB)

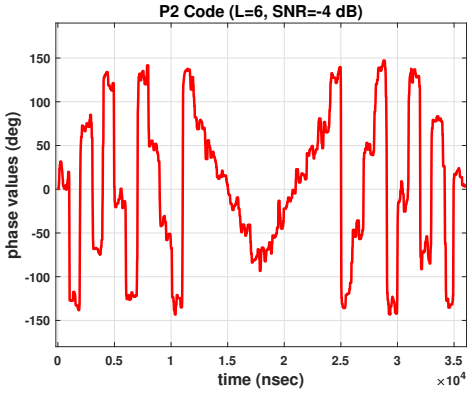

(f) P2 Code (L=6, SNR=-4 dB)

FIGURE 3.6: Phase Feature Plots of P2 Code (L=6) at different SNRs

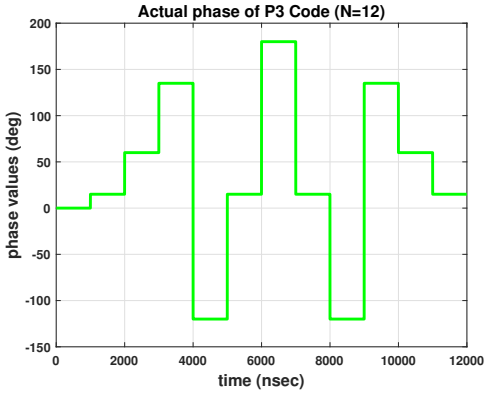

(a) P3 Code (N=12)

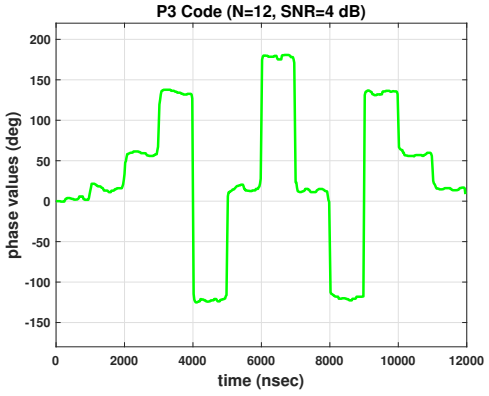

(b) P3 Code (N=12, SNR=4 dB)

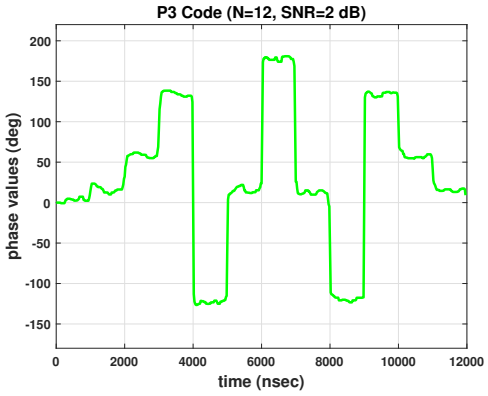

(c) P3 Code (N=12, SNR=2 dB)

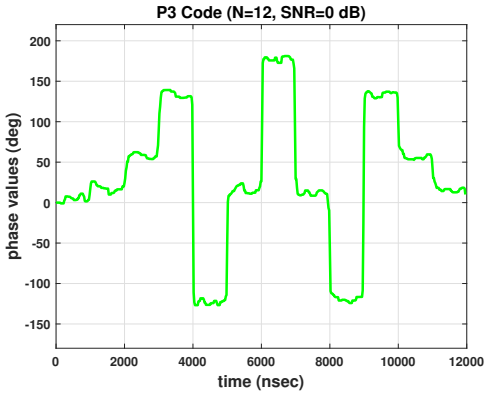

(d) P3 Code (N=12, SNR=0 dB)

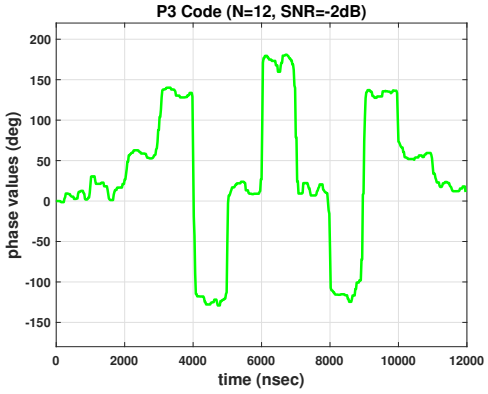

(e) P3 Code (N=12, SNR=-2 dB)

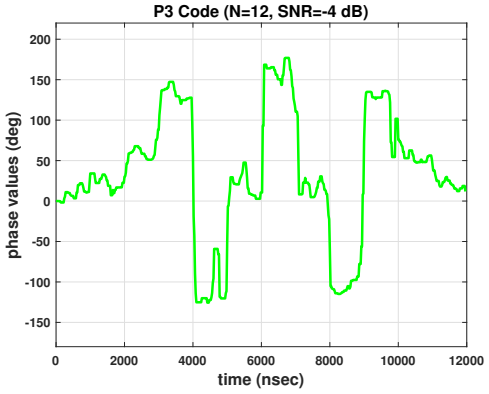

(f) P3 Code (N=12, SNR=-4 dB)

FIGURE 3.7: Phase Feature Plots of P3 Code (N=12) at different SNRs

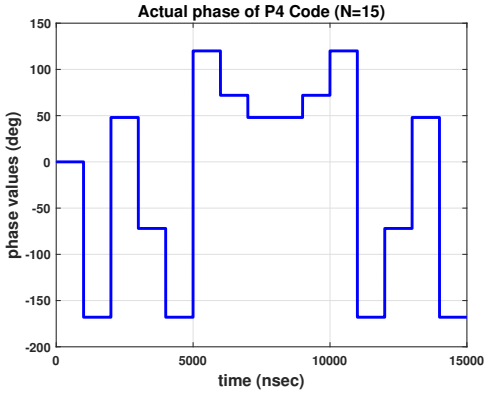

(a) P4 Code (N=15)

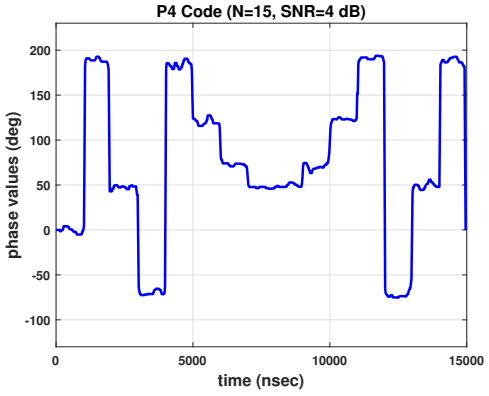

(b) P4 Code (N=15, SNR=4 dB)

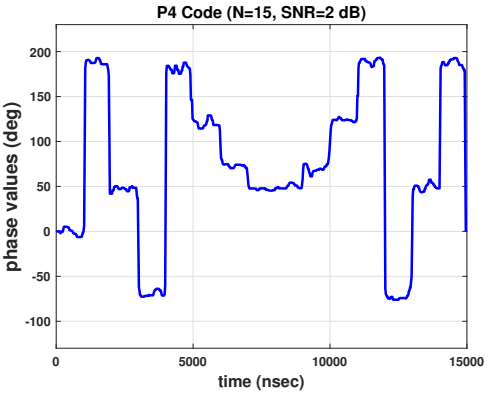

(c) P4 Code (N=15, SNR=2 dB)

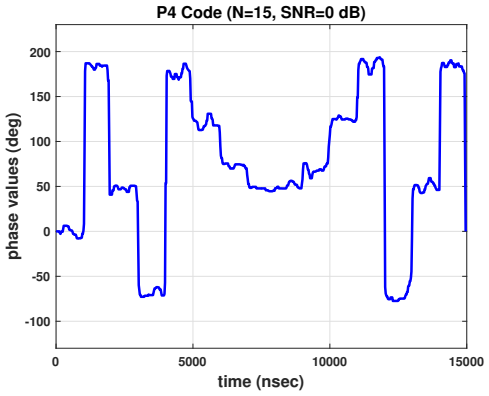

(d) P4 Code (N=15, SNR=0 dB)

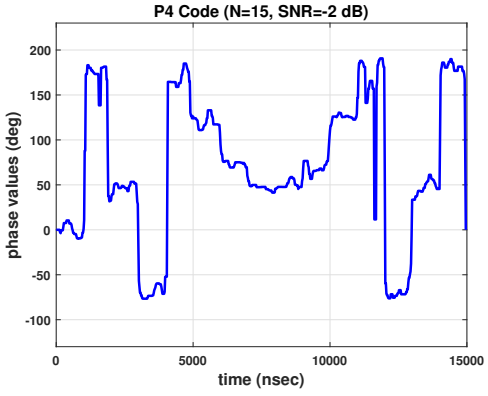

(e) P4 Code (N=15, SNR=-2 dB)

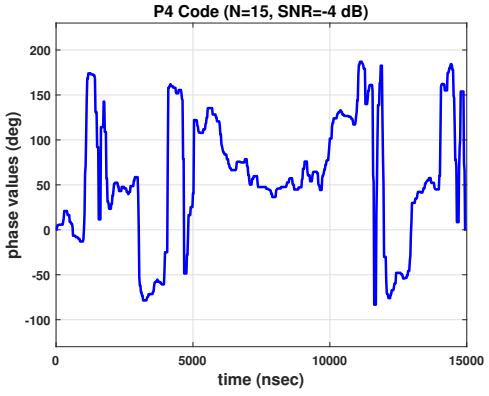

(f) P4 Code (N=15, SNR=-4 dB)

FIGURE 3.8: Phase Feature Plots of P4 Code (N=15) at different SNRs

In the detection part, the F_c of intercepted phase-coded signals is determined using the following steps:

a. Detection Problem

1. The six different types of phase-coded LPI radar waveforms are simulated using the formulas given in Subsection 1.7.5 at the SNR values ranging from -16 dB to 8 dB.

2. The simulated waveforms are divided into test and training datasets to train and validate the efficacy of the suggested architecture.

3. The FFT of the modulated phase-coded signal corrupted by AWGN is calculated intercepted at the EW receiver.

4. The absolute value of the FFT result is used to determine the greatest amplitude value, and the corresponding frequency, known as the carrier frequency (F_c) is determined.

b. Recognition Problem

1. After determining the F_c, the phase-coded signals are classified using the phase spectrum of STFT and DCNN.

2. The appropriate window size of STFT in terms of samples is obtained by taking the product of T_c (inverse of F_c) and sampling frequency (F_s).

3. The window forms a column vector with a length equal to FFT points when it is first slid across the signal and its phase values are computed that are stored in a pre-initialized matrix.

4. STFT is computed window-wise while the window is moved over the entire length of a signal and the phase-based matrix is obtained with the rows equal to FFT points and columns corresponding to the number of sliding windows.

5. The phase-based STFT matrix is then transformed into an image (phase spectrum) where the row corresponding to the F_c contains the phase offset introduced by phase coding schemes.

6. The remaining rows correspond to the AWGN added to the phase-coded signals.

7. Image cropping is done to obtain the seventh row that contains the phase pattern of a particular phase-coded signal. If the F_c shifts then the corresponding row will also change.

8. The seventh row corresponds to the F_c and it is assumed that all the phase coded waveforms are at the same F_c= 50 MHz.

9. Cropped image is then provided at the input of DCNN architecture for recognition purposes.

10. Finally, testing is done to judge the performance of the proposed feature extraction technique and recognition results are displayed in terms of confusion matrix plots.

The flow chart showing the detailed steps for the phase-based feature extraction for DCNN architecture is shown in Fig. 3.9.

3.4.2 Phase Feature Plots for DCNN

The flowchart depicted in Fig. 3.9 provides a detailed explanation of the method used to generate the phase spectrum. The phase values are computed from the output of STFT windows (column-wise) and the columns are stacked horizontally to obtain the phase feature matrix. The specific phase feature matrix is then transformed into phase spectrum.

A distinct phase pattern can be observed in all phase-based spectra that corresponds to the phase offset introduced by the phase coding technique in the carrier signal. The phase patterns can be seen in the seventh row of phase spectra, which

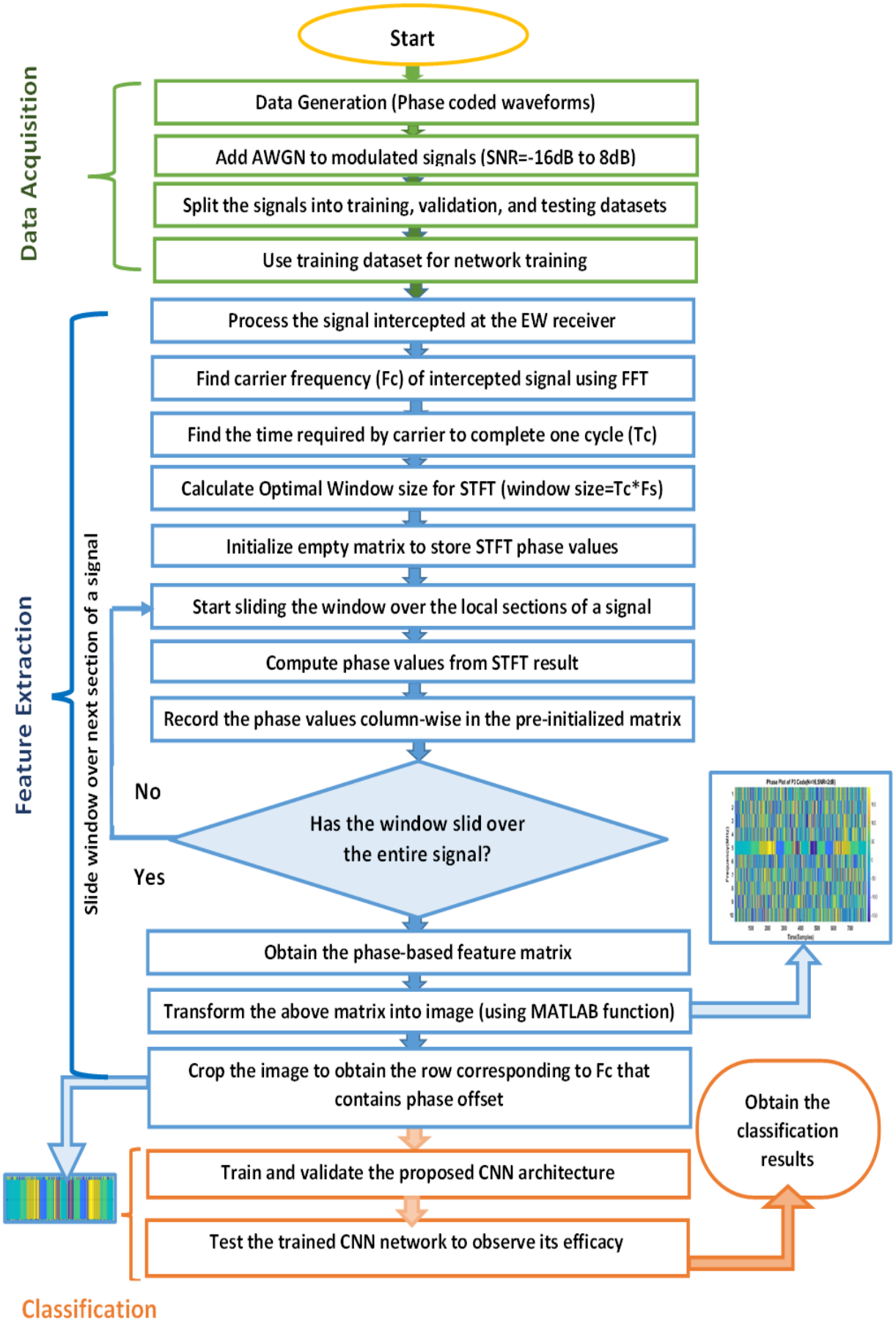

FIGURE 3.9: Flowchart of Phase-based Feature Extraction Algorithm for DCNN Architecture

corresponds to F_c= 50 MHz. It is assumed that all the signals are at the same carrier frequency. The specific phase pattern is going to appear in a different row when the carrier frequency shifts. Whereas, the remaining rows contain noise. The phase spectrum of the phase-coded signal is cropped to reduce the computational complexity of DCNN. Cropping is done to acquire the seventh row, which when provided as the input to the DCNN architecture, will give an idea about the type of phase-coded signals.

The x-axis represents the time duration of the signals (ns) and the y-axis represents the frequency (MHz). The phase values of the actual Barker code (Length=13) without AWGN are presented in Fig. 3.10(a), which serves as a reference. The phase is 0° from 0 μs till 5 μs and 180° for 5 μs through 7 μs. From 7 μs to 9 μs, it switches to 0°, its 180° for 9 μs till 10 μs, 0° for 10 μs till 11 μs, 180° for 11 μs till 12 μs, and 0° for 12 μs till 13 μs. The extracted phase images of Barker code are displayed in Fig. 3.10(b), Fig. 3.10(c), Fig. 3.10(d), Fig. 3.10(e), and Fig. 3.10(f) for SNR values of 4 dB, 0 dB, -4 dB, -8 dB, and -12 dB respectively. While the phase fluctuations of the retrieved Barker code features are basically identical to those of the benchmark code, they are noisy and can be observed in the seventh row (corresponding to Fc) of phase spectra. In Fig. 3.10(b), for the first 5 μs the blue color appears that corresponds to 0° phase, then 5 μs through 7 μs its yellowish color that represents 180° phase value as shown by color bar at the right. Then from 7 μs till 9 μs it's again blue, followed by yellow for the next 1 μs. The last three sub-pulses have blue, yellow, and blue color patterns respectively. If we observe Fig. 3.10(f), for SNR= -12 dB, several lines are appearing in the bluish and yellowish patterns that correspond to the noise. DCNN is chosen for the recognition of phase-coded waveforms with SNR up to -16 dB as it outperforms other DNNs on images.

As a reference, Fig. 3.11(a) presents the phase values of the actual Frank code (L= 4) without AWGN. The phase is 0° from 0 μs till 5 μs and shifts to 90° for the next 1 μs. It changes to 180° from 6 μs to 7 μs, then -90° from 7 μs to 8 μs, 0° from 8 μs to 9 μs, 180° from 9 μs to 10 μs, and 0° from 10 μs to 11 μs. From 11 μs till 12 μs there is 180° phase that again shifts to 0° for next 1 μs. From 13 μs

to 14 μs the phase is -90°. It switches to 180° for the next 1 μs and is 90° from 15 μs to 16 μs. Similarly, Fig. 3.11(b) represents the phase spectrum of Frank code at SNR=4 dB. It is obvious from the figure that for the first 5 μs the phase of 0° is shown by cyan colour. Its yellowish green for the next 1 μs (90°) and yellow from 6 μs to 7 μs (180°). Its blue from 7 μs till 8 μs (-90°). Its again cyan for the next 1 μs, It then follows the pattern as yellow, cyan, yellow, and cyan. It is then blue, yellow, and yellowish green for last 3 μs. Fig. 3.11(b) through Fig. 3.11(f) depict the phase spectrum of Frank code for SNR= 4 dB, 0 dB, -4 dB, -8 dB, and -12 dB respectively. The phase values correspond to different colors shown in the color bar that appears at the right of all phase spectra.

As a reference, Fig. 3.12(a) presents the phase values of the actual P1 code (L= 4) without AWGN. The phase is 0° from 0 μs till 1 μs and shifts to -135° for the next 1 μs. It changes to 90° from 2 μs to 3 μs, then -45° from 3 μs to 4 μs, 180° from 4 μs to 5 μs, 135° from 5 μs to 6 μs, and 90° from 6 μs to 7 μs. From 7 μs till 8 μs there is 45° phase that again shifts to 0° for next 1 μs. From 8 μs to 12 μs, the phase values are mirror images of values appearing from 5 μs to 8 μs. From 12 μs to 13 μs the phase is 180°. It switches to -45° for the next 1 μs and is 90° from 14 μs to 15 μs and is -135° for the last chip. Similarly, Fig. 3.12(b) represents the phase spectrum of P1 code at SNR=4 dB. It is obvious from the figure that for the 1 μs the phase of 0° is shown by cyan colour. Its royal blue for the next 1 μs (-135°) and yellowish green (90°) from 2 μs to 3 μs. Its blue from 3 μs till 4 μs (-45°). Its yellow (180°) for the next 1 μs, It then follows the pattern as orange (135°), yellowish green (90°), bluish green (45°), cyan (0°), bluish green (45°), yellowish green (90°), orange (135°), yellow (180°). It is then blue (-45°), yellowish green (90°), and royal blue (-135°) for last 3 μs. Fig. 3.12(b) through Fig. 3.12(f) depict the phase spectrum of Frank code for SNR= 4 dB, 0 dB, -4 dB, -8 dB, and -12 dB respectively.

Similarly, the benchmark P2 code (L= 6), P3 code (N= 12), and P4 code (N= 15) are compared to their respective derived phase-based feature images at different SNRs in Fig. 3.13(b) through Fig. 3.13(f), Fig. 3.14(b) through Fig. 3.14(f), and Fig. 3.15(b) through Fig. 3.15(f), respectively.

The length of the input signal, the window function, and overlap are some of the variables that affect the time complexity of STFT. Particularly, when parallelization and suitable window functions are used, STFT is computationally efficient. It is easy to implement and computationally fast because it is based on the well-established Fast Fourier Transform (FFT) methods. Because of these characteristic, STFT can be applied to a variety of embedded systems with constrained computational capabilities. As our algorithm involves STFT computations, so it can be easily implemented in real time RWR system as it involves simple and fast STFT implementations.

3.5 Phase-based Emitter Recognition Architectures

This section introduces the phase-based emitter recognition architectures that are utilized in the current research. The research's underlying assumptions are also included in this section. The proposed BiLSTM architecture employed for the recognition of phase-coded waveforms is discussed. Additionally, a detailed explanation of the suggested Deep CNN (DCNN) approach for automatic modulation recognition is also provided by the end of the section.

3.5.1 Assumptions

Several assumptions were taken to carry out the research work and are given below:

1. The type of RWR platform is assumed to be air-based.
2. Different types of threat emitters using specific phase-coded modulation schemes are assumed for detection and classification.
3. It is assumed that all the intercepted signals at RWR will be treated as threat signals.

4. All the phase-coded waveforms are assumed to have the same carrier frequency (Fc) of 50 MHz for the sake of simplicity.

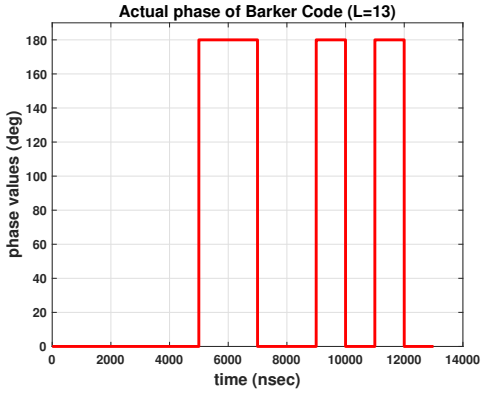

(a) Barker Code(L=13)

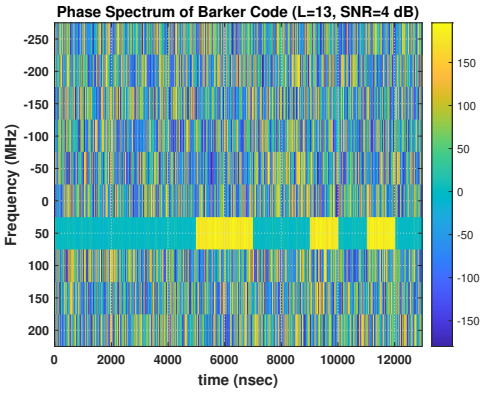

(b) Barker Code(L=13, SNR=4 dB)

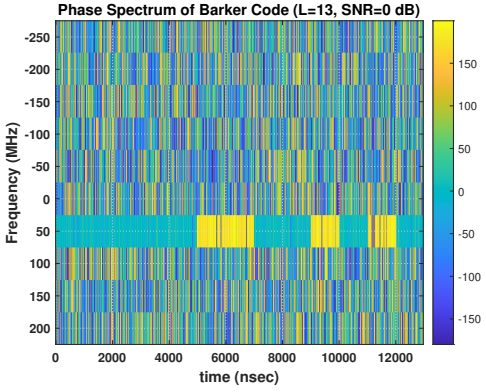

(c) Barker Code(L=13, SNR=0 dB)

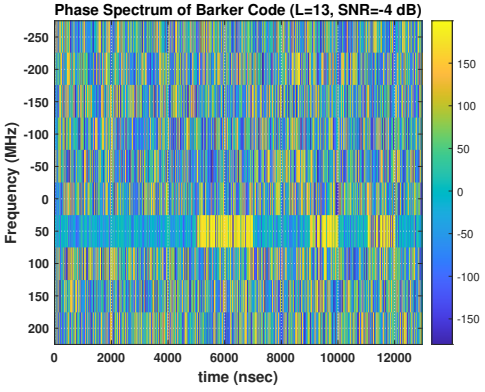

(d) Barker Code(L=13, SNR=-4 dB)

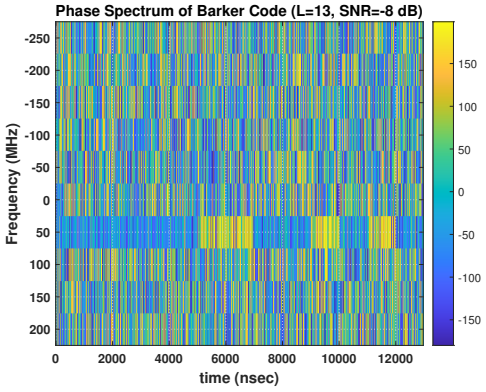

(e) Barker Code(L=13, SNR=-8 dB)

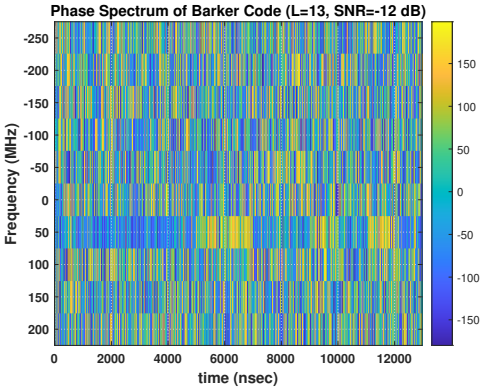

(f) Barker Code(L=13, SNR=-12 dB)

FIGURE 3.10: Phase Feature Images of Barker Code (Order=13) at different SNR Values. In the phase spectrum plots, 180° phase is shown in yellow whereas, cyan indicates the phase value of 0°.

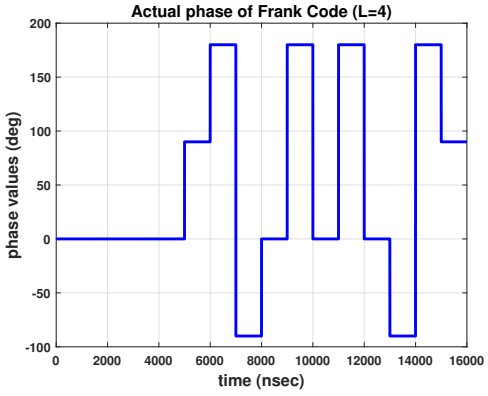

(a) Frank Code(L=4)

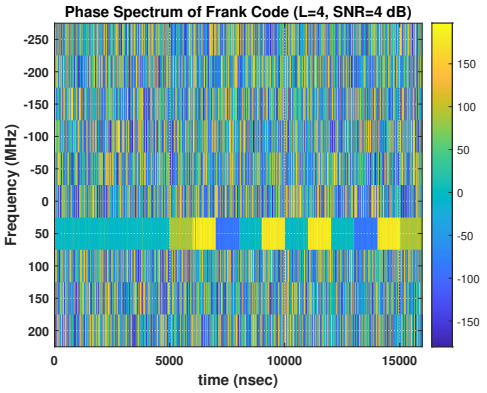

(b) Frank Code(L=4, SNR=4 dB)

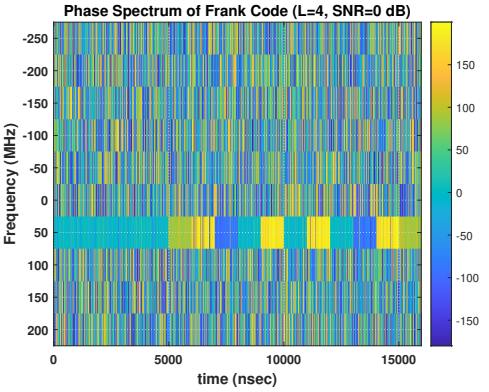

(c) Frank Code(L=4, SNR=0 dB)

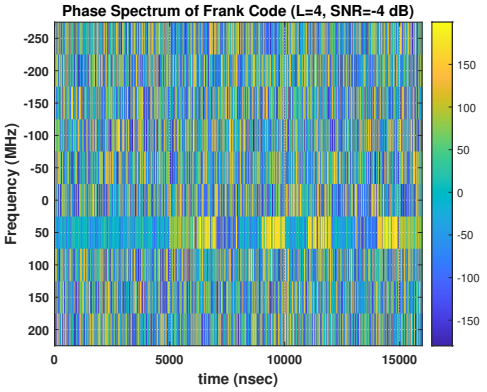

(d) Frank Code(L=4, SNR=-4 dB)

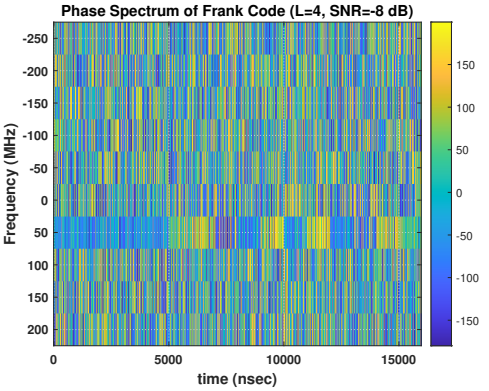

(e) Frank Code(L=4, SNR=-8 dB)

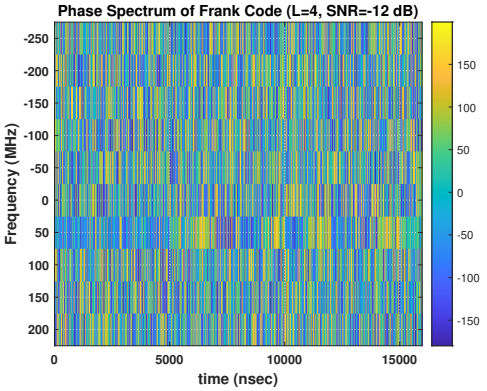

(f) Frank Code(L=4, SNR=-12 dB)

FIGURE 3.11: Phase Feature Images of Frank Code (L=4) at different SNRs. This code has four distinct phase values as shown by phase spectrum plots. The 180° phase is shown here in yellow, yellowish green is for 90°, blue indicates -90°, and cyan depicts the phase value of 0°

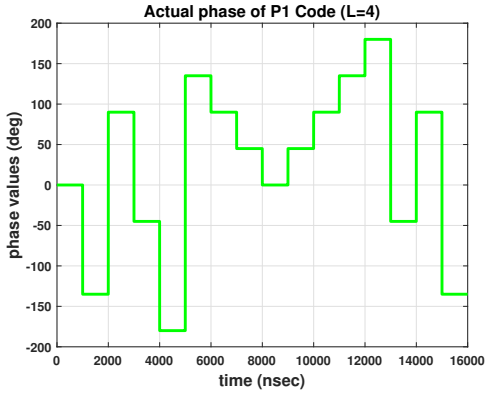

(a) P1 Code(L=4)

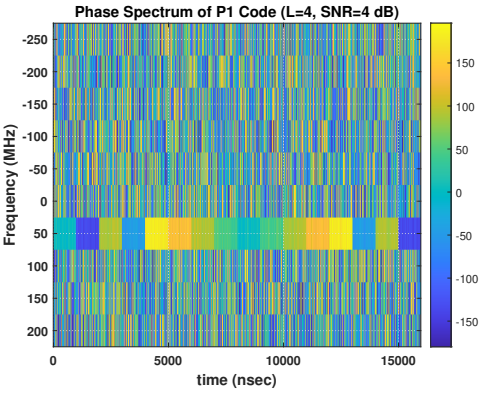

(b) P1 Code(L=4, SNR=4 dB)

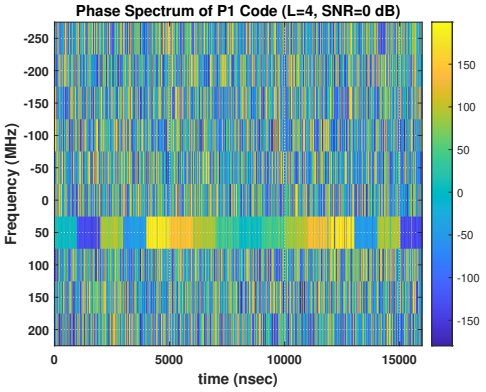

(c) P1 Code(L=4, SNR=0 dB)

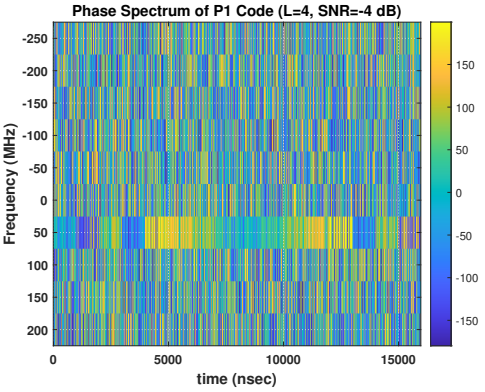

(d) P1 Code(L=4, SNR=-4 dB)

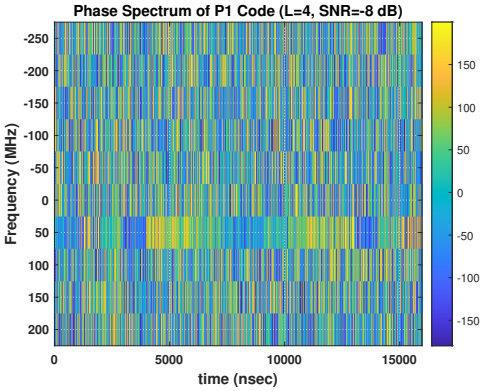

(e) P1 Code(L=4, SNR=-8 dB)

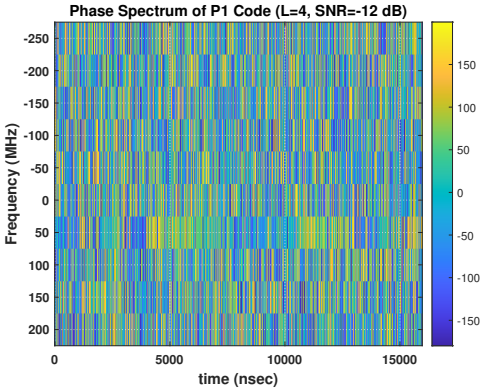

(f) P1 Code(L=4, SNR=-12 dB)

FIGURE 3.12: Phase Feature Images of P1 Code (L=4) at different SNRs. Here, cyan depicts the phase value of 0° as shown in phase spectrum plots, dark blue indicates -135°, yellowish green is for 90°, light blue indicates -45°, 180° phase is shown here in yellow, 135° for orange, bluish green indicates 45° phase.

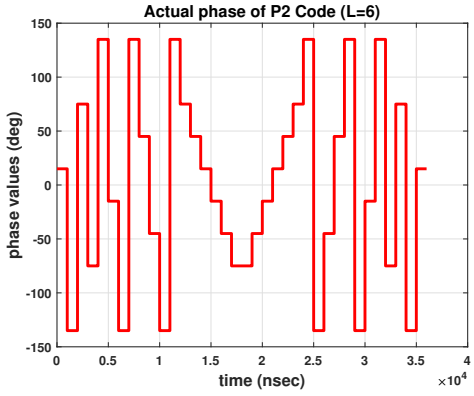

(a) P2 Code(L=6)

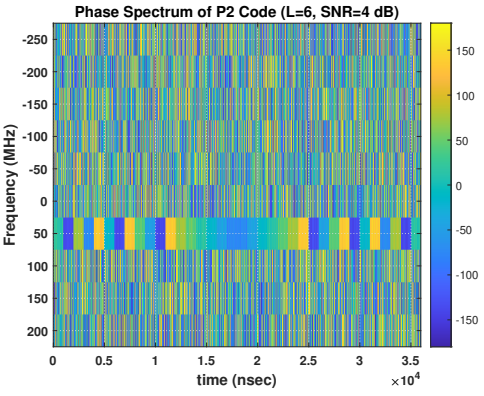

(b) P2 Code(L=6, SNR=4 dB)

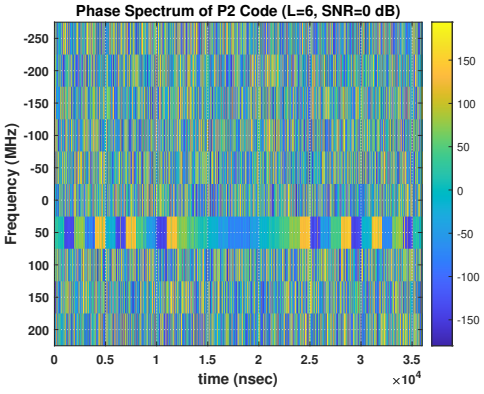

(c) P2 Code(L=6, SNR=0 dB)

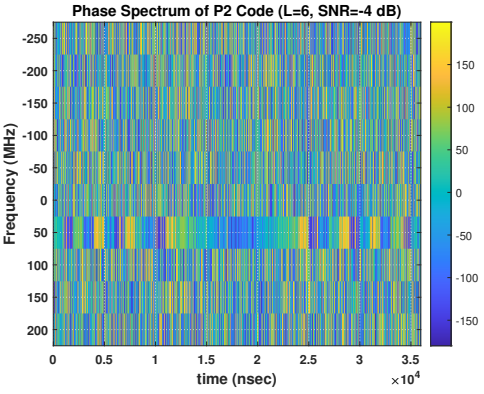

(d) P2 Code(L=6, SNR=-4 dB)

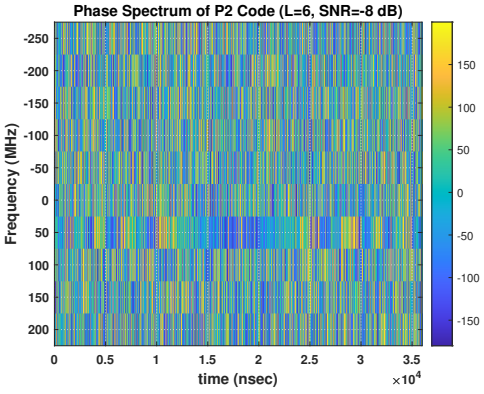

(e) P2 Code(L=6, SNR=-8 dB)

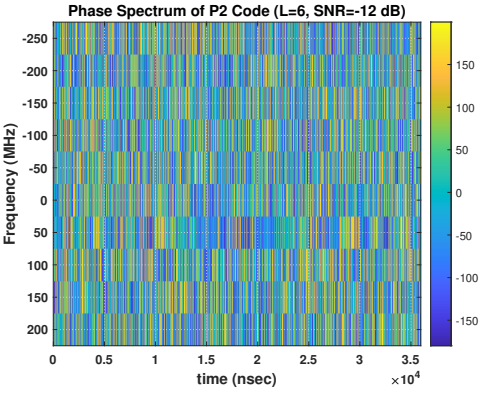

(f) P2 Code(L=6, SNR=-12 dB)

FIGURE 3.13: Phase Feature Images of P2 Code (L=6) at different SNRs. Here, the 1^{st} chip has blue color representing 15° phase, dark blue indicates -135°, 3^{rd} color is for 75°, 4^{th} color indicates -75° phase, 5^{th} indicates 180°, 6^{th} color is for -15°, 9^{th} color refers to 45°, next is for -45°, 14^{th} is for 45° again, 15^{th} is for 15°, followed by -15°, -45°, and -75° phase values. The next half of the code is mirror image of its first part as depicted by phase spectrum plots

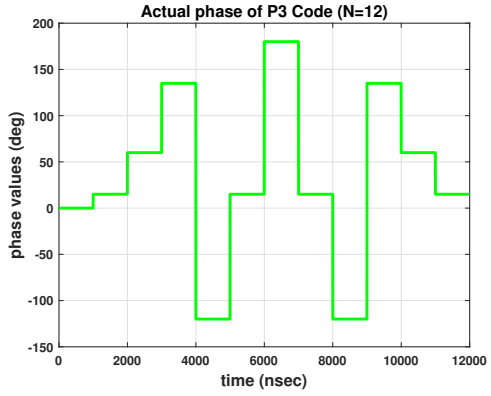

(a) P3 Code(N=12)

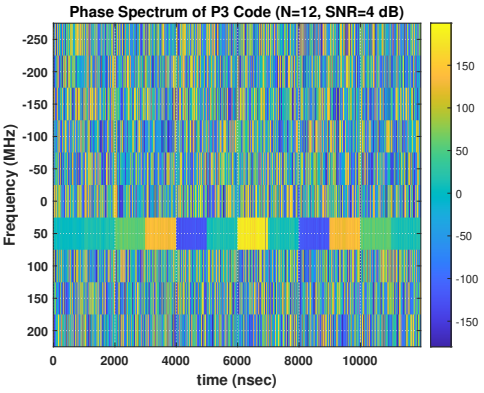

(b) P3 Code(N=12, SNR=4 dB)

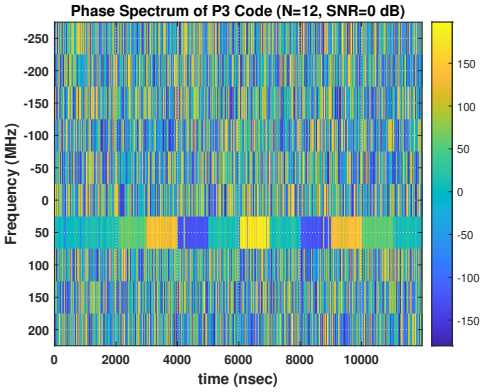

(c) P3 Code(N=12, SNR=0 dB)

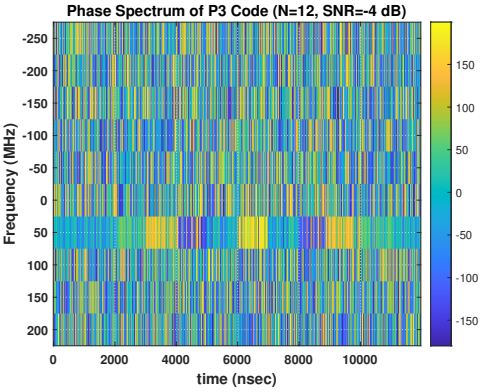

(d) P3 Code(N=12, SNR=-4 dB)

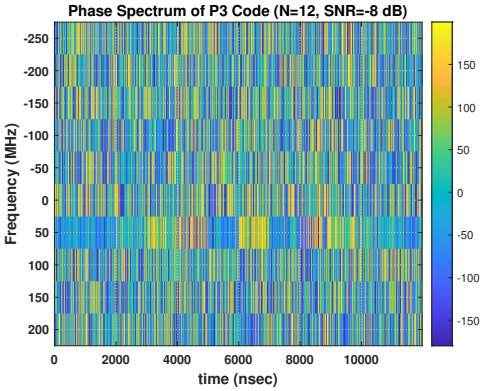

(e) P3 Code(N=12, SNR=-8 dB)

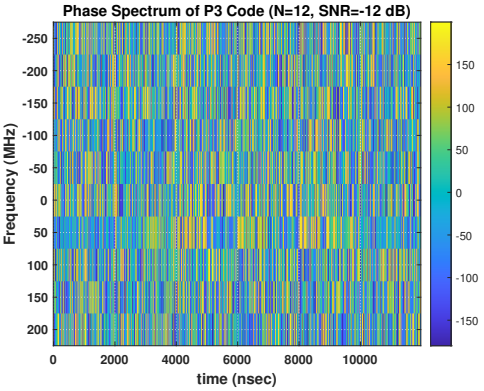

(f) P3 Code(N=12, SNR=-12 dB)

FIGURE 3.14: Phase Feature Images of P3 Code (N=12) at different SNRs. Here, the 1^{st} chip has cyan color representing 0° phase, 2^{nd} chip indicates 15°, 60° for next, followed by 135°, -120°, 0°, 180°, 0°, -120°, 135°, 60°, 15° respectively as shown in phase spectrum plots

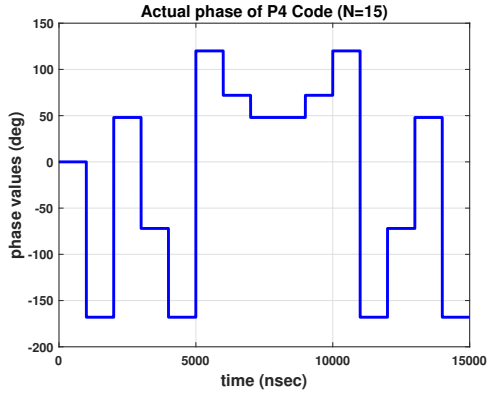

(a) P4 Code(N=15)

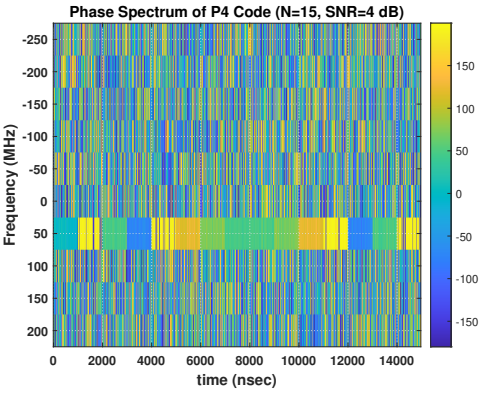

(b) P4 Code(N=15, SNR=4 dB)

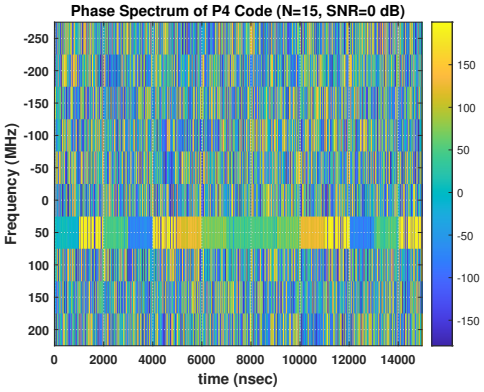

(c) P4 Code(N=15, SNR=0 dB)

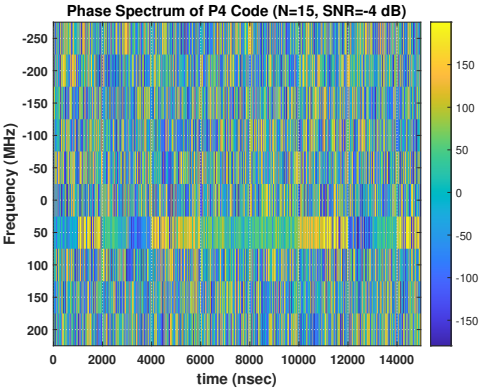

(d) P4 Code(N=15, SNR=-4 dB)

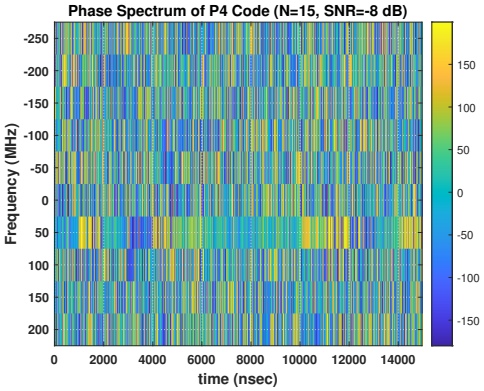

(e) P4 Code(N=15, SNR=-8 dB)

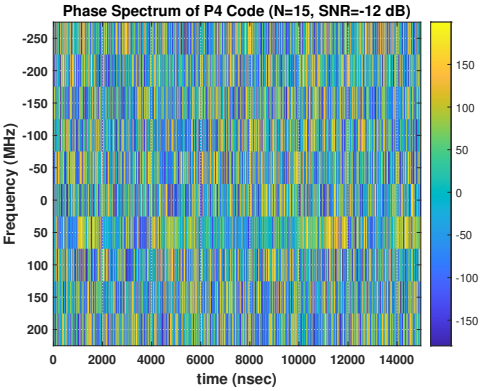

(f) P4 Code(N=15, SNR=-12 dB)

FIGURE 3.15: Phase Feature Images of P4 Code (N=15) at different SNRs. As shown in phase spectrum plots, the 1^{st} chip represents 0° phase, 2^{nd} chip indicates 180° due to wrapping, 48° for next, followed by -72°, 180°, 120°, 72°, 48°, 48°, 72°, 120°, 180°, -72°, 48°, 180° respectively

3.5.2 Phase-based Emitter Recognition Using BiLSTM Architecture

The automatic phase-based emitter recognition architecture employing BiLSTM network is described in this subsection. A detailed explanation of the three steps of the overall method is provided, including Waveform Generation, Phase Based Feature Extraction, and Recognition. The BiLSTM architecture used in this research is also presented.

3.5.2.1 Motivation for Using BiLSTM Architecture

LSTMs were introduced to overcome the limitations of traditional RNNs in handling long-term dependencies in sequential data like audio, video, and text. They use specialized memory cells and gating mechanisms to store and utilize information over extended time intervals, making them effective for tasks with significant temporal gaps [99]. Fig. 3.16 shows percentages of various tasks performed by the LSTM network in terms of a pie-chart. BiLSTM captures information from both past and future context, enhancing its ability to understand dependencies in the data. BiLSTM networks can perform different tasks like classification, language modeling, sentiment analysis, natural language inference, etc.

3.5.2.2 System Overview

The overall recognition technique is explained in great detail in this subsection. The three basic parts of the proposed identification system are the **Waveform Generation**, **Phase-based feature extraction**, and a **Classification network**, as shown in Fig. 3.17. STFT is computed for each waveform in the first step. The phase of the output is determined using the appropriate window size computed for STFT. In the second step, a phase-based feature vector is generated and in the third step, it is fed to the BiLSTM network's input for recognition purposes. Following the first and second sections, the system collects a large amount

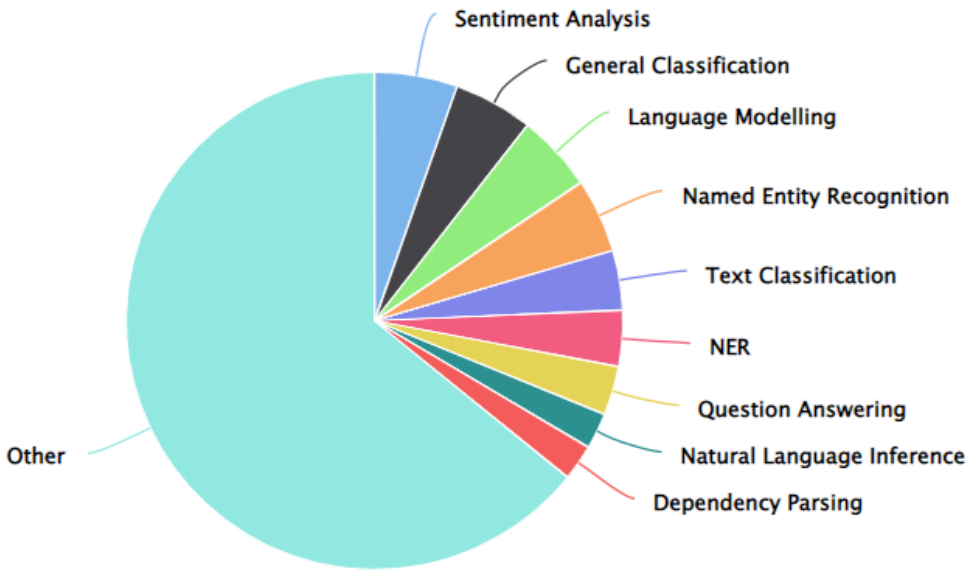

FIGURE 3.16: Tasks Performed by LSTM Network [100]

of information on various kinds of the waveform, and in the third section, all waveforms are finally categorized. Six different phase-coded waveform types, including Barker, Frank, P1, P2, P3, and P4, can be recognized using the BiLSTM model. Training of the BiLSTM network is done using 1D phase-based features. Once the network is trained, testing of the network is performed to judge the efficacy of the proposed phase-based feature extraction method using STFT phase spectrum. Finally, the recognition accuracies of the phase-coded waveforms will be discussed in the simulation part.

3.5.2.3 Design of BiLSTM Architecture

The proposed BiLSTM architecture is directly provided with the 1D phase-based features extracted from the phase of STFT, as discussed in Section 3.3.2. The phase-based features provided at the input of BiLSTM architecture are then processed by LSTM cells present in the LSTM layer. The key components of an LSTM cell are three gates performing different functions. The forget gate determines what information to discard, the input gate controls what new information to add, and the output gate controls what information from the cell state should

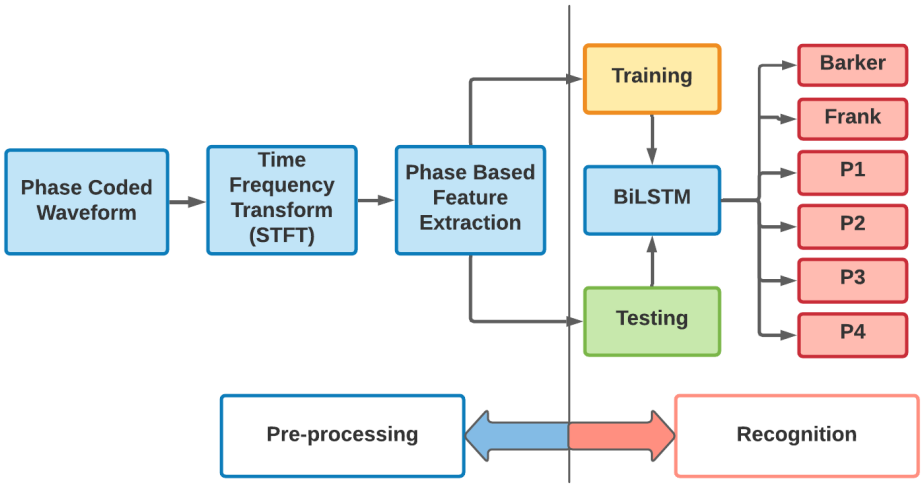

FIGURE 3.17: There are three basic steps in the proposed recognition process. STFT is initially applied to all phase coded waveforms intercepted at RWR. A phase-based feature vector is computed in the second step, and it is then provided as input to the BiLSTM network in the third step to accomplish recognition task

be given at the output. The cell state is basically the memory that retains essential information from previous time steps. This architecture enables the LSTM to effectively handle long-term dependencies and process sequential data. The BiLSTM network consists of two LSTM layers. The Forward LSTM layer processes the sequence from the first time step to the last. Similarly, the Backward LSTM layer processes the sequence in reverse, from the last time step to the first.The outputs of both LSTM layers are combined and the expression for forget gate is:

$$f_t = \sigma(W_f.[h_{t-1}, x_t] + b_f), \tag{3.5}$$

Here, σ is the sigmoid activation function. b_f is the bias term for forget gate and W_f are the weights. h_{t-1} represents the recurrent information at previous time step and x_t is the current input. The expression for input gate is:

$$i_t = \sigma(W_i.[h_{t-1}, x_t] + b_i), \tag{3.6}$$

Where, b_i is the bias term for the input gate and W_i are the corresponding weights. The cell state is updated using the following relations:

$$\tilde{C}_t = \tanh(W_c.[h_{t-1}, x_t] + b_c). \tag{3.7}$$

$$C_t = (f_t * C_{t-1} + i_t * \tilde{C}_t). \tag{3.8}$$

Here, b_c and W_c are the bias term and weights for updating cell state. The expression for output gate is:

$$o_t = \sigma(W_o.[h_{t-1}, x_t] + b_o), \tag{3.9}$$

$$h_t = o_t * \tanh(C_t). \tag{3.10}$$

Here, W_o are the weights; b_o is the bias term for output gate, and h_t represents the current recurrent information. The gate structure was created specifically to deal with the issue of exploding or vanishing gradients in RNN. The final outcome is represented by the symbol y_t, which may be expressed as follows:

$$y_t = [{h_t}^f,\ {h_t}^b]. \tag{3.11}$$

Here, t= 1, 2, 3, ..., n, represents the time steps. Hence, both the forward ${h_t}^f$ and backward activations ${h_t}^b$ are used to calculate the output at any time instant t. The BiLSTM layer contains 100 hidden units. The fully connected layer follows the BiLSTM layer and contains 200 nodes. A softmax layer is used that applies a softmax function to its input. Finally, the classification layer is utilized to accomplish the recognition task. A classification layer computes the cross-entropy loss for multi-class classification problems. The output size of the previous layers is used to determine the number of classes in this layer. At an SNR of -2 dB, the technique proposed in this subsection exhibits an overall recognition accuracy of more than 90%. Back Propagation Through Time (BPTT) is a training technique for RNNs on sequential data, where each time step is unrolled to apply the back-propagation algorithm. Errors are calculated and accumulated for each time step, making it computationally expensive for long sequences, leading to vanishing or exploding gradients. To address this, Truncated Back Propagation Through Time (TBPTT) is used, limiting the number of time steps considered during back-propagation, which helps mitigate the computational cost and gradient issues. The layers' structure in the proposed BiLSTM-based emitter recognition architecture

is also shown in Fig. 3.19. Six phase-coded waveforms are classified using the proposed BiLSTM architecture, and the results of the simulations are given in the following chapter.

3.5.3 Phase-based Emitter Recognition Using DCNN Architecture

In this subsection, the proposed DCNN based automatic modulation recognition architecture used in this research is explained in detail.

3.5.3.1 Motivation for Using DCNN

DCNNs are used for image classification due to their ability to automatically learn hierarchical features, exploit local correlations, and achieve translation invariance. The parameter sharing, non-linear activation, and transfer learning capabilities further enhance their scalability and performance for the image recognition tasks [23, 27, 28, 85, 88].

3.5.3.2 System Overview

We present a DCNN-based radar AMCS in this subsection. The framework of the suggested technique is shown in Figure 3.20. The intercepted LPI radar waveforms are divided into various categories using this recognition method. The proposed method works by transforming the signal modulation recognition problem into a Time-Frequency Image (TFI) recognition problem by using STFT. The approach is divided into three sections, as shown in Fig. 3.20. The first step involves the generation of phase-coded LPI radar signals discussed in Chapter 1. In the next step, the TFI of the intercepted signals is obtained by computing the phase spectrum of STFT, and pre-processing is performed. Cropping of TFI is done

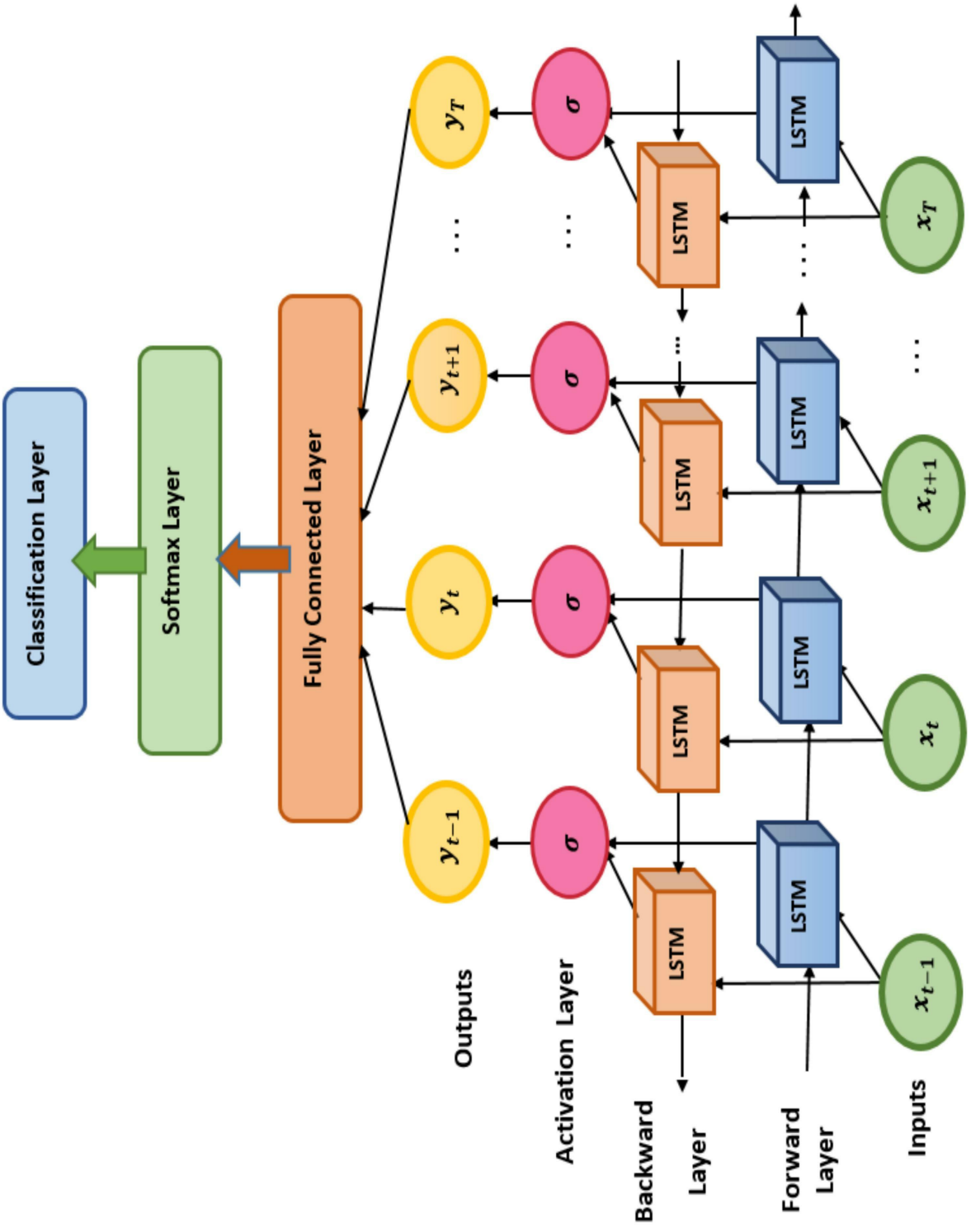

FIGURE 3.18: Phase-coded Signal Recognition using the BiLSTM Architecture

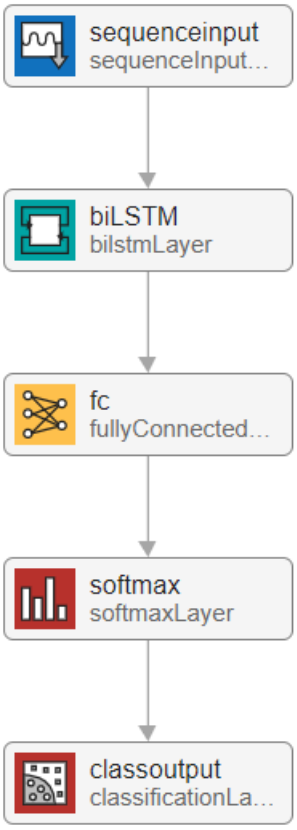

FIGURE 3.19: Hierarchy of Layers in the Proposed BiLSTM-based Emitter Recognition Architecture

to obtain only the segment with the phase information in order to decrease the computational complexity of DCNN.

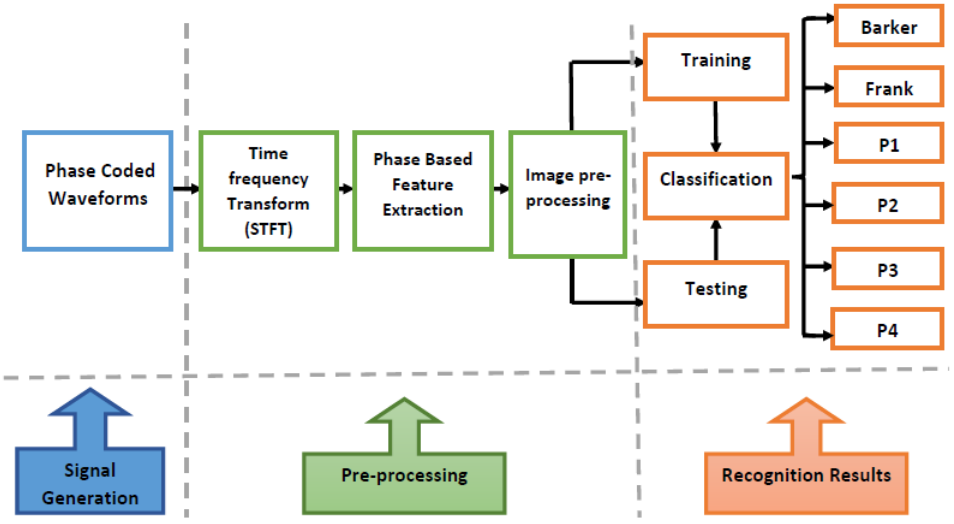

FIGURE 3.20: The proposed AMCS consists of three parts. Initially phase coded signals are generated followed by pre-processing of phase-based TFI obtained from STFT. Finally recognition is done using DCNN architecture

However, in a low SNR situation, the TFI still contains a lot of noise, making the recognition problem more challenging. In the last step, cropped TFIs are fed to DCNN architecture for the classification of phase-coded LPI radar waveforms.

3.5.3.3 Design of Deep Convolutional Neural Network (DCNN)

Fig. 3.21 depicts the DCNN structure used in this work for classification of phase-coded waveforms. The DCNN model includes ten layers in total, including convolutional layers (3), pooling layers (3), a flattening layer (1), a fully connected layer (2), and a single output layer. The sizes and number of filters used for different convolutional layers are also shown in Fig. 3.21. Here is a sequence of the functions that make up the DCNN's structure: Input−Con−ReLU−Pool−dropout−Con−ReLU−Pool−dropout−Con− ReLU− Pool− dropout−FL−FC1−FC2−dropout −OL, where Con denotes the Convolution layer, ReLU is non-linear activation function, Pool represents the pooling layer, FL represents the flattened layer, FC1 and FC2 are two fully connected layers, and to prevent the overfitting dropout layer is used. The OL is the output layer containing 6 neurons that represent 6 different categories of phase-coded waveforms. All the remaining parameters are shown in Fig. 3.21. Assume the convolutional layer's input size is L×M×Q, indicated by I, where Q indicates the number of channels. L is the height and M is the width of the input image. The dimensions of the input image are 46×545×3 pixels for simulations. The convolution kernel K has a size of F×F×Q and a number of R. The convolutional kernel size is chosen 3×3 for all convolutional layers. The convolution stride is 1. The following is a description of the convolution process:

$$C(n,m,R) = \sum_{l=1}^{Q} \sum_{i=0}^{F-1} \sum_{j=0}^{F-1} I(n+i, m+j, l) * K_R(i,j,l) + bias_R, \tag{3.12}$$

where, K_R and $bias_R$ represents the R^{th} convolutional kernel and its bias term respectively. C denotes the output of convolution. n∈[1,O] and m∈[1,P].

$$O = [\frac{L-F}{stride} + 1], \qquad P = [\frac{M-F}{stride} + 1]. \tag{3.13}$$

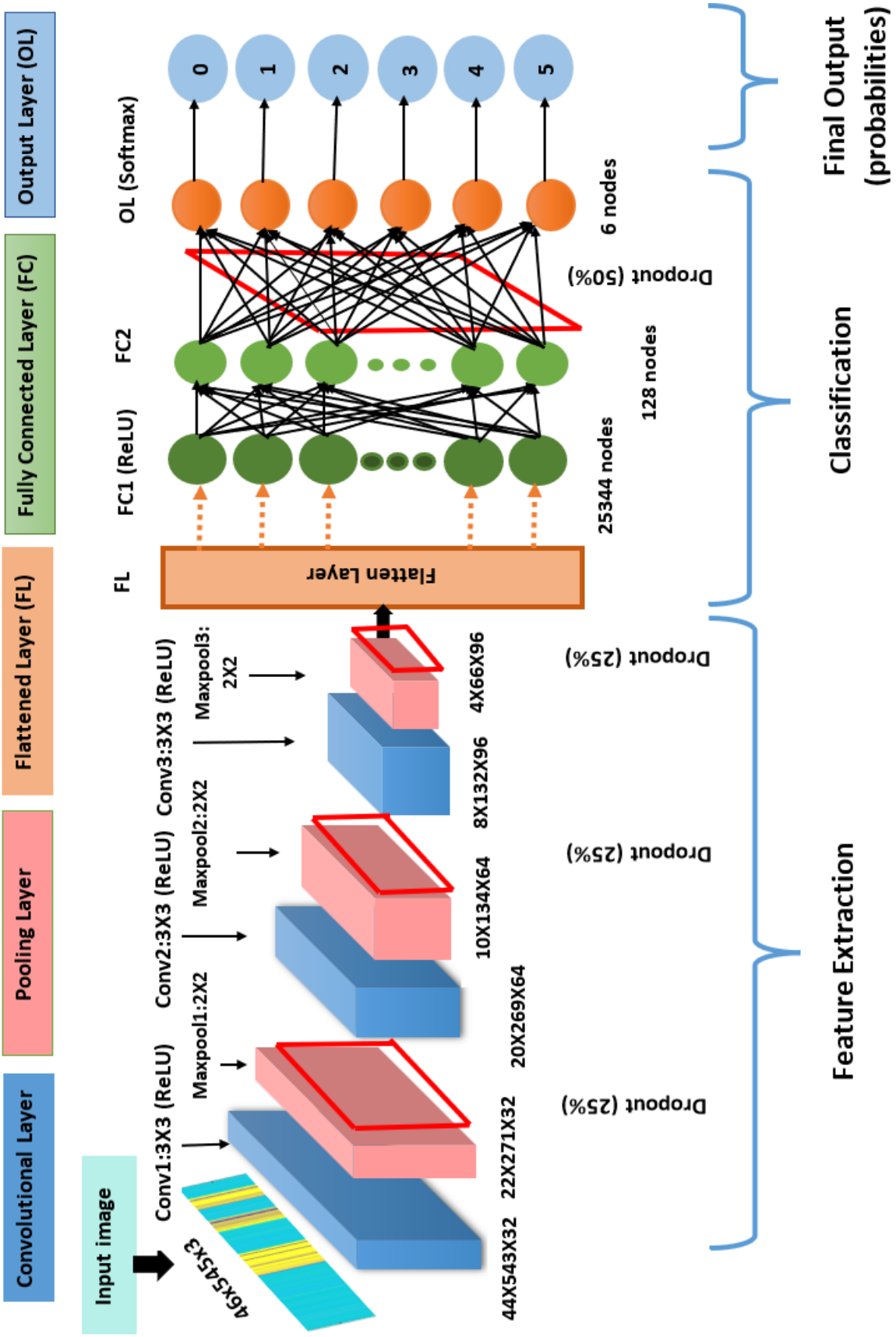

FIGURE 3.21: The Proposed DCNN Architecture is composed of three Convolutional Layers, three Pooling Layers, a Flattening Layer, two Fully Connected Layers, and an Output Layer. For each Convolutional Layer, there are 32, 64, and 96 Feature Maps respectively. The size of the Kernel for each Convolutional Layer is 3 ×3

Modern CNNs frequently use the ReLU activation function since it effectively prevents gradients from vanishing [101]. The ReLU function is written as follows:

$$C_{out}(n, m, R) = max[0, C(n, m, R)]. \tag{3.14}$$

The pooling layer must be utilized to reduce the dimensions and parameters of data to prevent overfitting. We employ maximum pooling with filter size of 2×2 and stride size of 2 in this work.

$$C_d(n, m, R) = \underset{i,j \in \{0,1\}}{max} \{C_{out}(2n + i - 1, 2m + j - 1, R)\}. \tag{3.15}$$

Use equations (3.12), (3.14), and (3.15) to calculate the output of the last convolutional layer which is then fed to FL to convert 2D data into 1D vector. The output of the FL layer is given at the input of FC_1 having 25344 input nodes and 128 output nodes. FC_2 has 128 input nodes and 6 output nodes (corresponding to 6 phase-coded waveforms). All the nodes between FC_1 and FC_2 are fully connected like the dense layers in the NN. h_{FC} denotes the output of the FC_1. Note, W_{FC} is the weight matrix between the FC_1 and FC_2. Similarly, the weight matrix between the FC_2 and the OL is W_{Out}. h_{FL} is the input to the FC_1. The outputs obtained from FC_2 and OL are h_{FC} and Out. b_{FC} and b_{Out} are their bias terms respectively.

$$h_{FC} = f(W_{FC} h_{FL} + b_{FC}), \tag{3.16}$$

$$Out = f(W_{Out} h_{FC} + b_{Out}). \tag{3.17}$$

We use the softmax activation function on the output layer to produce the final results of classification. There is a dropout of 50% between the FC_2 and OL to prevent overfitting and to reduce the computational complexity. The classification output $\hat{y}$ in terms of probability is given as follows:

$$\hat{y_p} = P(y_{act} = p|Out) = \frac{e^{Out_p}}{\sum_{p=1}^{6} e^{Out_p}}, \tag{3.18}$$

where, $\hat{y} = [\hat{y_1}, \hat{y_2}, \hat{y_3}, ..., \hat{y_6}]^T$. Out_p denotes the p^{th} component of the output vector. The probability that the input is assigned to class p is given by $\hat{y_p}$. The DCNN classification result corresponds to the category with the highest $\hat{y_p}$.

$$J(y_{act}, \hat{y}) = \min\{-[y_{act} \log(\hat{y}) + (1 - y_{act}) \log(1 - \hat{y})]\}, \tag{3.19}$$

where, y_{act} is the true label of the class and $\hat{y}$ represents the predicted label. In Fig. 3.22, the DCNN model is shown in terms of the dimensions of input to the layers and the corresponding output dimensions.

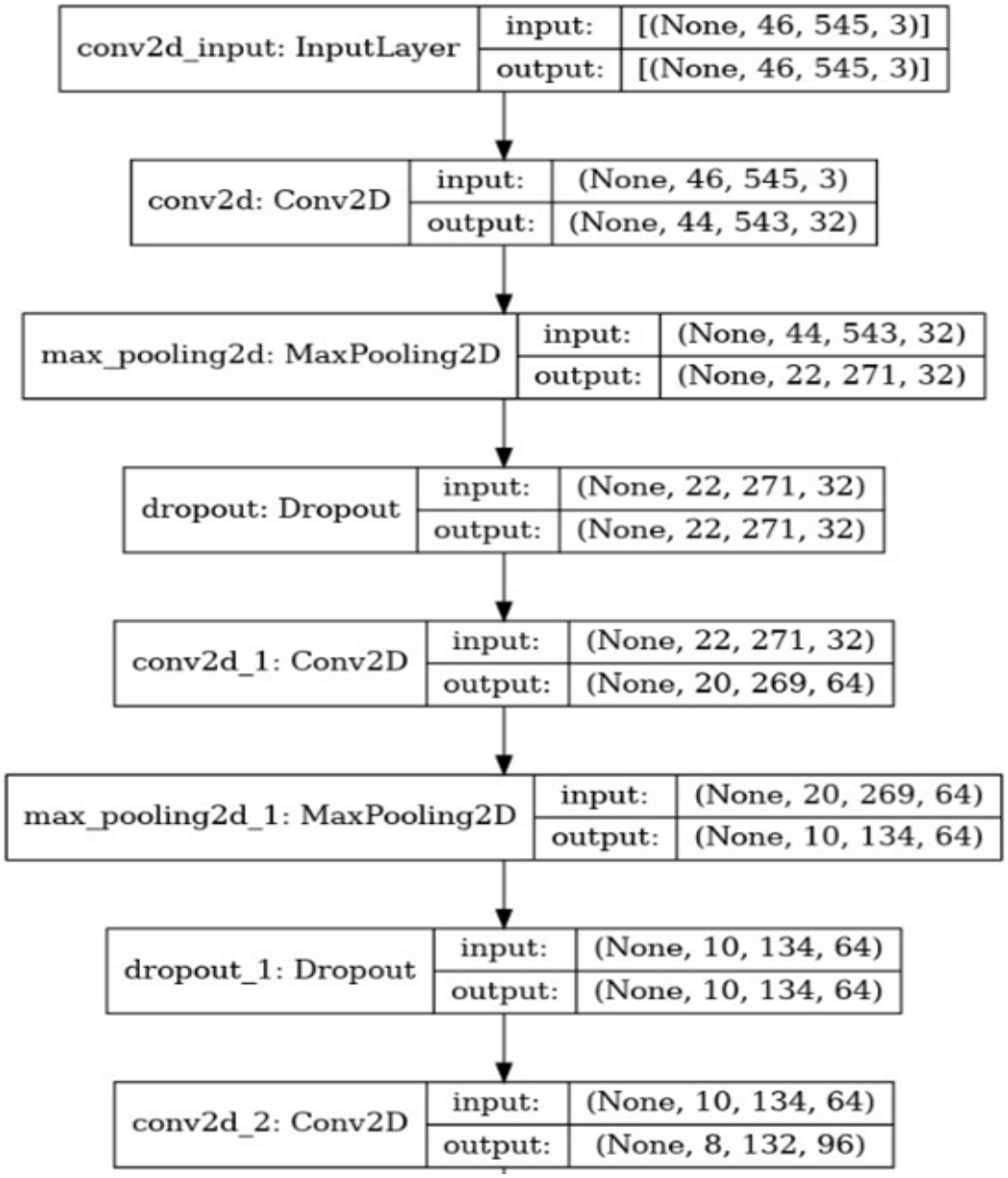

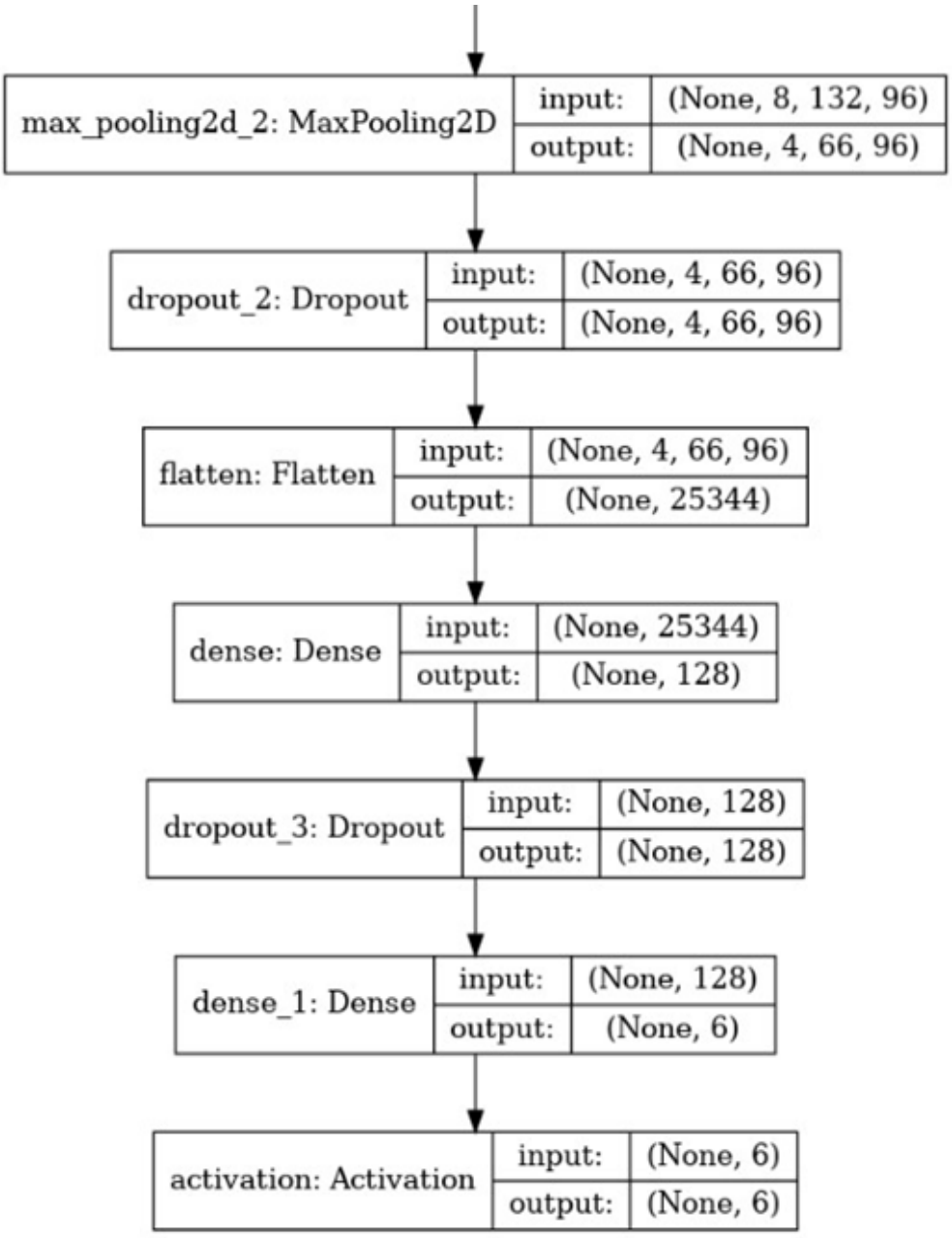

FIGURE 3.22: DCNN Architecture in Terms of Input and Output Dimensions

3.5.4 Algorithms for BiLSTM and DCNN architectures

The algorithms for BiLSTM and DCNN architectures based intrapulse modulation recognition are given in the Table 3.1 and 3.2 respectively.

TABLE 3.1: Algorithm for BiLSTM based Intrapulse Modulation Recognition Architecture

Input:	Testing dataset (features=102×1 cell, at each SNR value), trained BiLSTM network, $\hat{y}$=[]
Output:	Predicted labels= $\hat{y}$
Step 1:	Extracted phase based features are given at the input of "Sequence Input Layer", features dim=1 (phase based vector)
Step 2:	Phase features from sequence input layer are then fed to BiLSTM layer, hidden nodes=100, W_f, b_f, W_i, b_i, W_c, b_c, W_o, b_o, $h_t = 0$, $C_t = 0$: **1. Calculations for Forget Gate:** $f_t = \sigma(W_f.[h_{t-1}, x_t] + b_f)$ **2. Calculations for Input Gate:** $i_t = \sigma(W_i.[h_{t-1}, x_t] + b_i)$ $\tilde{C}_t = \tanh(W_c.[h_{t-1}, x_t] + b_c)$ **3. Calculations for updating Cell state:** $C_t = (f_t * C_{t-1} + i_t * \tilde{C}_t)$ **4. Calculations for Output Gate:** $o_t = \sigma(W_o.[h_{t-1}, x_t] + b_o)$ $h_t = o_t * \tanh(C_t)$
Step 3:	The output y_t is computed from both the forward and backward activations of BiLSTM layer: $y_t = [{h_t}^f,\ {h_t}^b]$
Step 4:	The output of BiLSTM layer is then given to fully connected layer, input nodes= 200, output nodes= 6 $h_{FC} = \sigma(W_{FC} y_t + b_{FC})$, $Out = h_{FC}$
Step 5:	Softmax layer then applies the softmax function to Out, nodes=6 (corresponds to phase-coded waveforms), y_{act} : $\hat{y_p} = P(y_{act} = p \mid Out) = \frac{e^{Out_p}}{\sum_{p=1}^{6} e^{Out_p}}$
Step 6:	Classification Layer is then used that holds the loss function, size of output, and predicted label $\hat{y_p}$ for class p
Step 7:	Append the values of $\hat{y_p}$ in $\hat{y}$: $\hat{y} = [\hat{y};\ \hat{y_p}]$
Step 8:	Repeat the Step 1 till Step 7 for all input feature vectors from testing dataset at different SNR values.

TABLE 3.2: Algorithm for DCNN based Intrapulse Modulation Recognition Architecture

Input:	Testing dataset (images), trained DCNN, $\hat{y}$=[]
Output:	Predicted labels= $\hat{y}$
Step 1:	Perform convolution on input image (I), Num_Fil=32, stride=1, Fil_size=[3×3], Num_Ch=3: $C(n,m,R) = \sum_{l=1}^{Q} \sum_{i=0}^{F-1} \sum_{j=0}^{F-1} I(n+i, m+j, l) * K_R(i,j,l) + bias_R$
Step 2:	Apply ReLU on the obtained feature maps from previous step: $C_{out}(n,m,R) = max[0, C(n,m,R)]$
Step 3:	Perform down-sampling using max pooling, stride=2, size=[2×2]: $C_d(n,m,R) = \underset{i,j\in\{0,1\}}{max}\{C_{out}(2n+i-1, 2m+j-1, R)\}$
Step 4:	Apply 25% dropout on output of max pooling (C_d)
Step 5:	Repeat Step 1 (Num_Fil=64), Step 2, Step 3, and Step 4 on the output of Step 4
Step 6:	Again repeat Step 1 (Num_Fil=96), Step 2, Step 3, and Step 4 on the output of Step 5
Step 7:	Flatten the output obtained from last pooling layer in Step 6: $C_{FL} = reshape\ (C_d^{'}, [1\ \ size\ (C_d, 1) * size\ (C_d, 2)\ ])$
Step 8:	Apply following calculations on all nodes of FC_1, input nodes= 25344, output nodes= 128, W_{FC}, b_{FC}: $h_{FC} = f(W_{FC} C_{FL} + b_{FC})$
Step 9:	Apply following calculations on all nodes of FC_2, input nodes= 128, output nodes= 6, W_{Out}, b_{Out} : $Out = f(W_{Out} h_{FC} + b_{Out})$
Step 10:	Apply 50% dropout on output of FC_2
Step 11:	Compute the output (Out) in terms of probability $\hat{y_p}$ of class p : $\hat{y_p} = P(y_{act} = p \mid Out) = \frac{e^{Out_p}}{\sum_{p=1}^{6} e^{Out_p}}$
Step 13:	Append the values of $\hat{y_p}$ in $\hat{y}$: $\hat{y} = [\hat{y};\ \hat{y_p}]$
Step 14:	Repeat the Step 1 till Step 13 for all input images (I) from testing dataset at different SNR values and plot their recognition accuracies and versus SNR

3.6 Real World Settings

In real-world application, the RER method is employed at RWR to enhance situational awareness and aid in decision-making during various practical scenarios. In EW missions, RER plays a central role in understanding the enemy's electronic emissions. This information is used to develop and implement electronic countermeasures, such as jamming or emitting deceptive signals to disrupt enemy radar and communication systems. It's important to note that RER is often used in conjunction with other sensor systems, such as active ECM and passive ESM, to create a comprehensive EW suite. These systems work together to improve the efficiency of military platforms by delivering precise and immediate information about the electromagnetic environment and potential threats. Here's an outline of the steps involved for implementing the proposed research idea in the real world settings:

3.6.1 Data Collection

Gathering and preparing the training data is a crucial part of this process. The first step is to collect a large dataset of intercepted radar signals, specifically phase-coded waveforms, from various radar emitters. This data can be obtained through real-world measurements, simulations, or a combination of both. For real-world measurements, RWR systems equipped with data recording capabilities can be used to capture intercepted radar signals during military exercises or missions. For simulations, realistic radar signal simulators can generate synthetic data representing different radar emitters.

3.6.2 Signal Preprocessing

Once the dataset is collected, preprocessing is required to extract the phase-based features from the data in order to train the deep learning architectures. Each data

sample in the dataset needs to be labeled with the corresponding radar emitter type.

3.6.3 Data Augmentation

The diversity and generalization of the training data can be enhanced using data augmentation techniques or AWGN can be added at different SNR values to get more realistic dataset.

3.6.4 Model Training

The proposed deep learning architecture is trained on the preprocessed and labeled dataset. During training, the model learns to recognize patterns and features that are indicative of specific radar emitter types.

3.6.5 Model Validation

After the initial training, the performance of model is validated using a validation dataset. Fine-tuning of the model is done based on validation results to improve its accuracy and generalization.

3.6.6 Testing and Evaluation

The trained RER model is evaluated on an independent testing dataset to assess its real-world performance. The model's ability to correctly recognize phase-coded waveforms intercepted at the RWR is critical to its effectiveness in practical scenarios. Evaluation of the trained model is done to judge the performance of the proposed RER method for LPI radar waveform recognition. The recognition accuracies can be observed versus SNR values. In order to be more realistic, the recognition accuracies upto -16 dB can be considered.

3.6.7 Deployment and Continuous Improvement

Once the model is trained and validated, it can be deployed into the RWR system for real-world use. Regular updates and retraining may be necessary to accommodate new radar emitters or improve the model's performance based on real-world feedback.

3.7 Chapter Summary

This chapter starts with a basic notion of feature extraction, which is crucial for various ML models. The merits of the feature extraction method are discussed, and then a novel, STFT-based feature extraction method is proposed. Detailed steps of the proposed feature extraction technique (1D & 2D) given in the form of flow charts for both architectures (BiLSTM & DCNN). The derived phase-based features for particular phase-coded waveforms at various SNR levels are also displayed. The proposed deep learning architectures (BiLSTM & DCNN) employed in this research are also explained in detail. The simulations conducted to assess the effectiveness of the suggested phase-based feature extraction technique are covered in the next chapter.

Chapter 4

Simulations and Results

In this chapter, the RWR platform is simulated for practical consideration. The phase-coded signals are simulated to obtain the baseline simulations.The phase-coded signals considered for the simulations include Barker, Frank, P1, P2, P3, and P4. The simulated phase-coded signals are modulated and AWGN is added to realize different SNR environments. The signals are modulated at the carrier frequency (F_c) of 50 MHz. For threat emitter recognition, it is assumed that all the threat emitters are at the same carrier frequency. The SNR values considered for the BiLSTM-based approach vary from -8 dB to 8 dB with a 2 dB step size, whereas for the DCNN-based emitter recognition method SNR ranges from -16 dB to 8 dB with the same step size. At RWR, the modulated and AWGN-corrupted phase-coded waveforms are intercepted. STFT is used to extract features from the phase spectrum of phase-coded waveforms. By considering the derived phase features at various SNR values, the effectiveness of the proposed phase spectrum-based emitter recognition architectures presented in Chapter 3 can be investigated.

Section 4.1 describes the simulation settings, network parameters, and results for 1D BiLSTM-based RER approach whereas, Section 4.2 includes the simulation setup and recognition results for the proposed 2D DCNN-based RER architecture. The recognition accuracies versus SNR are also given in the tabular form. In Section 4.3, the two RER methods proposed in this research effort are compared to determine which one is more efficient.

4.1 Simulation Results for RER using BiLSTM

This section provides a detailed description of the simulation setup and the findings obtained for the 1D BiLSTM-based RER approach by considering the recognition accuracies of phase coded waveforms versus SNR to evaluate the performance of the proposed architecture.

4.1.1 Simulation Settings

Six distinct forms of phase-modulated signals, including Barker, Frank, P1, P2, P3, and P4 codes, are used to investigate the efficacy of the proposed recognition approach using BiLSTM. There are specific parameters for each waveform that need to be adjusted. The carrier wave frequency (Fc) for all signals is assumed to be 50 MHz, and the sampling frequency is Fs= 500 MHz. There are various phase-coded waveforms, each with a particular pulse width. The simulation uses Barker code elements of length (M= 4, 7, 11, 13) having pulse widths of 2 μs, 14 μs, 11 μs, and 13 μs respectively. P1 codes are generated for lengths (L= 2, 4) with pulse widths of 8 μs, and 16 μs respectively. Similarly, P2 codes are produced for lengths (L= 4, 6) with pulse widths of 16 μs, and 36 μs respectively, using the formula expressed in Section 1.7.5. For (Nc= 4, 12, 16), P3 codes are generated with pulse widths of 8 μs, 12 μs, and 16 μs respectively. P4 codes are used to generate signals for (Nc= 4, 12, 15) having pulse widths of 8 μs, 12 μs, and 15 μs, respectively. There are six main categories of phase-coded waveforms represented by a total of 17 signals. In Table 4.1, the parameters of simulated phase-coded signals are listed. The category labels for various phase-coded waveforms are the model's output. For Barker, Frank, P1, P2, P3, and P4 codes, the total number of samples is 20000, 35000, 12000, 16000, 28000, and 17500, respectively, at each SNR value. The overall sample count goes to 128500 at each SNR value. Signals are subjected to five iterations of AWGN for the generating the training datasets at each SNR value. So, the total number of samples at each SNR is 6,42,500.

From -8 dB to 8 dB, there are nine SNR values with a step size of 2 dB. The total number of training and testing signals is calculated as:

$$\text{Training signals (total)} = 17\times5\times9 = 765 \text{ signals} \tag{4.1}$$

$$\text{Training samples (at each SNR)} = 1{,}28{,}500\times5 = 6{,}42{,}500 \text{ samples} \tag{4.2}$$

$$\text{Total Training samples (for all SNRs)} = 57,\ 82{,}500 \text{ samples} \tag{4.3}$$

$$\text{Testing signals (at each SNR)} = 17\times6 = 102 \text{ signals} \tag{4.4}$$

$$\text{Testing signals (total)} = 17\times6\times9 = 918 \text{ signals} \tag{4.5}$$

$$\text{Testing samples (at each SNR)} = 1{,}28{,}500\times6 = 7{,}71{,}000 \text{ samples} \tag{4.6}$$

$$\text{Total Testing samples (at all SNRs)} = 69{,}39{,}000 \text{ samples} \tag{4.7}$$

The proposed BiLSTM network is trained to utilize 765 signals for six different types of phase-coded waveforms after the various emitter signals are simulated with different phase-coding schemes. We split the labels in half, using 20% for validation and 80% for training. The testing dataset, which contains a total of 918 signals with SNR values ranging from -8 dB to 8 dB, is used to evaluate the BiLSTM network's ability to recognize different phase-coded signals. The recognition accuracies of phase coded waveforms versus SNR are displayed in tabular form to observe how the recognition accuracy drops as the SNR decreases.

4.1.2 Network Parameters

The number of hidden layers, hidden nodes in the BiLSTM layer, activation functions, and other hyper parameters must all be set in order for the classifier model to execute classification tasks. The input and recurrent weights are randomly initialized by using a Gaussian distribution with a zero mean and a standard deviation of σ. The initial bias terms are set zero for all gates. During the learning phase, training epochs are also crucial. In our BiLSTM architecture, just 50

TABLE 4.1: Parameter Setting of Phase-coded Radar Waveforms

Modulation Type	Parameters	Values
1. Barker Code	Length of Code (M)	[4,7,11,13]
2. Frank Code	Frequency Steps(L)	[3,4,6]
	CPP	[100,50,50]
3. P1 Code	Frequency Steps(L)	[2,4]
	CPP	[100,50]
4. P2 Code	Frequency Steps(L)	[4,6]
	CPP	[50,50]
5. P3 Code	Compression Ratio (Nc)	[4,12,16]
	CPP	[100,50,50]
6. P4 Code	Compression Ratio (Nc)	[4,12,15]
	CPP	[100,50,50]

TABLE 4.2: Training Parameters for BilSTM Architecture

SN.	Parameters	Values
1	Number of BiLSTM Layers	1
2	Hidden Units (BiLSTM Layer)	100
3	Activation function	tanh, sigmoid
4	Epochs	50
5	Optimizer	Adam
6	Mini batch size	306
7	Learning rate	0.01
8	Gradient threshold	1
9	Shuffle	Once every epoch
10	Sequence length	According to longest sequence

training epochs are used to train the network, and 100 hidden nodes are selected. The optimal weights are acquired using the ADAM optimizer. For each training iteration, the mini-batch size is fixed at 306 signals, which is half of the total training signals (612). The initial learning rate for training is set at 0.01. The network is validated after 20 training iterations for the validation frequency of

20. The network itself modifies the length of the sequence for a single iteration of the mini-batch while taking the gradient threshold to be 1. The values of the optimal training parameters chosen for simulations are listed in Table 4.2. The training and validation accuracy plots are displayed in Fig. 4.1 for the trained BiLSTM architecture. The plot in blue represents the training accuracy while the black dashed line depicts the validation accuracy. By the end of 50 epochs, the training accuracy is close to 95% whereas validation accuracy is 86%. Similarly, the plots for training and validation loss are also displayed in Fig. 4.2. The plot in red represents the training loss while the black dashed line depicts the validation loss.

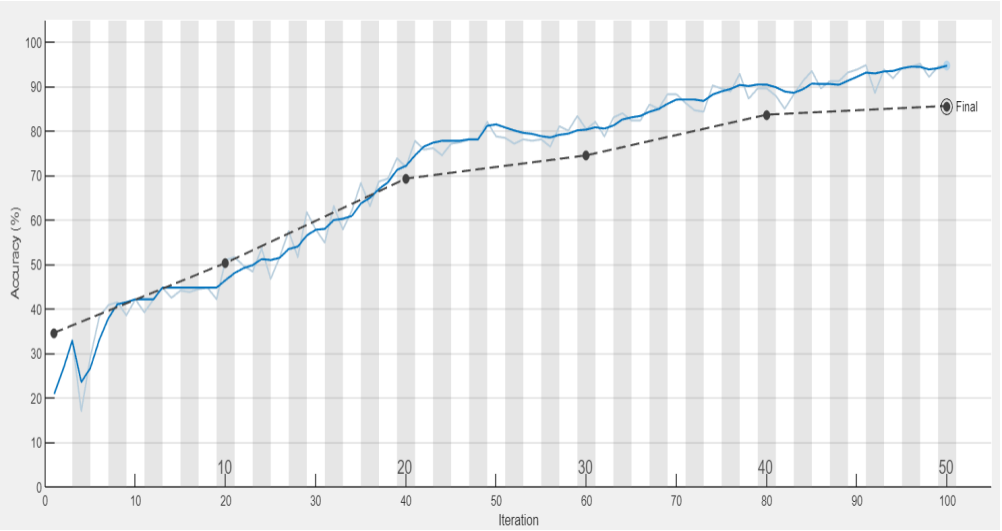

FIGURE 4.1: Training and Validation Accuracy of BiLSTM Architecture

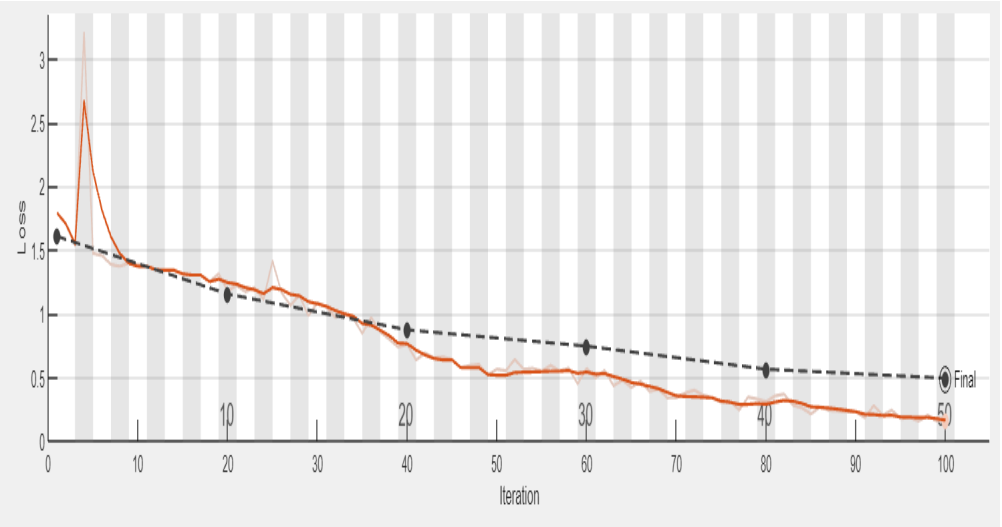

FIGURE 4.2: Training and Validation Loss of BiLSTM Architecture

The validation loss approaches 0.5 whereas the training loss is close to 0 on the completion of 50 epochs which shows the convergence of the trained BiLSTM architecture.

4.1.3 Recognition Results

In this subsection, the recognition accuracies of phase-coded waveforms are given as a function of SNR. Since AWGN is introduced to the signals, the simulations are run at least ten times for each SNR value before the averaged accuracy values are displayed in Table 4.3 for SNR values ranging from -8 dB to 8 dB with a 2 dB step size. Every waveform has a distinct relationship between RERA and SNR. For each waveform in our system, SNR and RERA are positively correlated. For all phase-coded waveforms, RERA significantly rises till the SNR of -2 dB. Almost all waveforms, with the exception of Frank codes, have a RERA of 90% or above at SNR of -2 dB. Barker codes have 80% recognition accuracy at SNR= -8 dB which increases significantly and reaches 100% by 0 dB as shown in Table 4.3. P1 codes have more than 60% recognition accuracy at -8 dB, and by -2 dB, 100% recognition accuracy is achieved. P2 codes have recognition accuracies of more than 80% at -8 dB, whereas P3 codes have accuracies of 72% as displayed in Table 4.3. According to Table 4.3, P4 codes begin out with a recognition accuracy of about 68%, increasing to 91% by -2 dB and then 100% by 6 dB. Frank codes have the lowest recognition accuracy of 50% when compared to the other codes and require additional accuracy improvements. The overall recognition accuracies of phase coded waveforms are also given in the last row of Table 4.3. At -8 dB, the overall recognition accuracy is 70% that increases significantly and ultimately reaches 100% by SNR= 8 dB. The overall recognition accuracies of phase-coded waveforms are also presented in Fig. 4.3. At SNR= -8 dB, the recognition accuracy is 70% which increases significantly from 70% to 96% with the increase in SNR value from -8 dB to -2 dB. After -2 dB, there is a gradual change in accuracy and finally, it reaches 100% at SNR= 8 dB. Precision, recall, and F1 score are important metrics for evaluating classifiers as they provide insights into

TABLE 4.3: Recognition Accuracies Versus SNR Obtained from BiSLTM Network

Signals	-8 dB	-6 dB	-4 dB	-2 dB	0 dB	2 dB	4 dB	6 dB	8 dB
Barker	80	83	94	99	100	100	100	100	100
Frank	50	72	75	81	83	87	89	92	93
P1	62	89	96	100	100	100	100	100	100
P2	84	92	97	100	100	100	100	100	100
P3	72	91	97	99	100	100	100	100	100
P4	68	69	79	91	94	97	99	100	100
Overall	70	82	90	96	97	98	99	99	100

their performance. These metrics are based on the concepts of True Positives (TP), True Negatives (TN), False Positives (FP), and False Negatives (FN). TP represent correct positive predictions. TN represent correct negative predictions, FN occurs when the classifier predicts negative incorrectly, and FP refer to incorrect positive predictions.

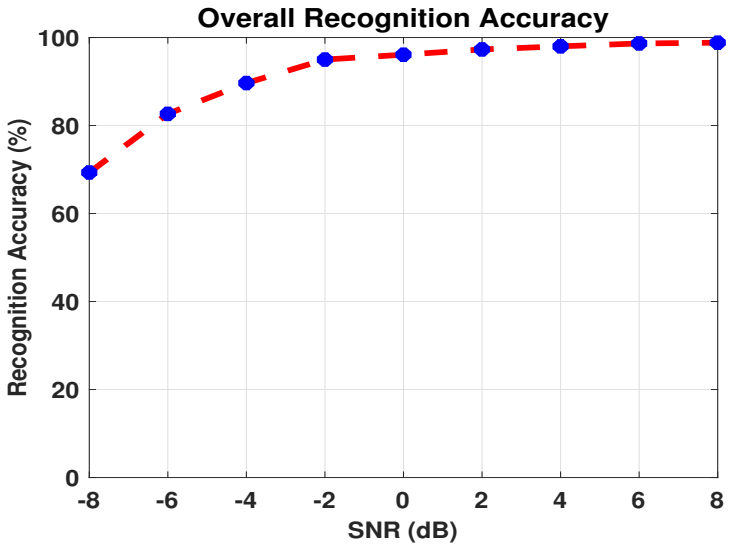

FIGURE 4.3: Overall Recognition Accuracies Versus SNR for BiLSTM Architecture

.

4.1.3.1 Precision

Precision evaluates the correctness of positive predictions by indicating the proportion of predicted positive instances that are accurate. The formula of precision

is given by:

$$Precision = \frac{TP}{TP + FP} \tag{4.8}$$

4.1.3.2 Recall

Recall assesses the classifier's ability to correctly detect positive instances by indicating the proportion of actual positive instances that are successfully identified. The formula of recall is given by:

$$Recall = \frac{TP}{TP + FN} \tag{4.9}$$

4.1.3.3 F1-Score

The F1 score combines precision and recall into a single measure, offering a balanced assessment of the classifier's overall performance. It takes into account both the accuracy of positive predictions and the ability to identify positive instances, providing a comprehensive evaluation metric. The formula of F1 score is given by:

$$F1\text{-}Score = 2 \times \frac{Precision \times Recall}{Precision + Recall} \tag{4.10}$$

The recognition accuracies of most of the phase coded waveforms are 90% at SNR$\geq$ -2 dB except the Frank codes as shown in Table 4.3. The precision, recall, F1 score, and accuracy of phase coded waveforms are given at SNR values of -4 dB, -6 dB and -8 dB in the Table 4.4, 4.5, and 4.6, respectively.

4.2 Simulation Results for RER using DCNN

In this section, the simulation results for the RER method using DCNN architecture are given. Signal generation and simulation settings are the same as in the

TABLE 4.4: Precision, Recall, F1 score, and Accuracy at SNR= -4 dB

Signals	Precision	Recall	F1 Score	Accuracy
Barker	81.74	92.16	86.63	94
Frank	90.36	79.8	84.75	75
P1	78.69	96.97	86.87	96
P2	100	96.04	97.98	97
P3	93.27	97.98	95.56	97
P4	97.53	73.83	84.04	79

TABLE 4.5: Precision, Recall, F1 score, and Accuracy at SNR= -6 dB

Signals	Precision	Recall	F1 Score	Accuracy
Barker	75.45	78.3	76.84	83
Frank	80	77.4	78.67	72
P1	70.1	91.75	79.4	89
P2	96.84	92	94.35	92
P3	87.5	91.9	89.64	91
P4	87.34	62.7	73	69

TABLE 4.6: Precision, Recall, F1 score, and Accuracy at SNR= -8 dB

Signals	Precision	Recall	F1 Score	Accuracy
Barker	63	75.47	68.67	80
Frank	81.97	55.56	66.23	50
P1	62.63	70.45	66.31	62
P2	95.45	86.6	90.8	84
P3	69.23	75	72	72
P4	63.55	62.39	62.96	68

previous section. However, SNR values ranging from -16 dB to 8 dB with a 2 dB step size are considered.

4.2.1 Simulation Settings

Barker, Frank, P1, P2, P3, and P4 codes are among the six types of simulated radar signals. After several emitter signals have been simulated using various phase

coding techniques, STFT is utilized to determine the phase spectrum. The phase spectra are cropped to acquire the specific portion that corresponds to the carrier signal's phase offset according to the details given in Chapter 3. The dataset includes 674 images for all 6 types of phase-coded signals with SNRs varying from -16 dB to 8 dB with a 2 dB step size. We split the training data into two parts, using 80% for training and 20% for validation of the proposed architecture. The ability of the DCNN network to differentiate among phase-coded signals is analyzed using a testing dataset of 102 signals at each SNR value. The test dataset contains 1326 images in total for all 13 SNR values. Signals are subjected to six iterations of AWGN for the generating the testing dataset at each SNR value. The value of SNR can be computed by using the following expression:

$$SNR = 10log_{10}\frac{{\sigma_s}^2}{{\sigma_n}^2}, \tag{4.11}$$

where, ${\sigma_s}^2$ and ${\sigma_n}^2$ are signal and noise power, respectively. The calculations for training and testing signals are given below:

$$\text{Training signals (total)} = 674\,\text{images}, \tag{4.12}$$

$$\text{Testing signals (at each SNR)} = 17\times6 = 102\,\text{images}, \tag{4.13}$$

$$\text{Testing signals (total)} = 17\times6\times13 = 1326\,\text{images}. \tag{4.14}$$

4.2.2 Network Parameters

The hyper-parameters, including the size of the input, the number of convolution feature maps, the size of the convolution and pooling filters, number of Fully Connected (FC) layers, the neurons in the FC layers, etc. are selected using series of Monte Carlo simulations to identify the optimal structure for DCNN. The optimal input size is chosen as $[46 \times 545 \times 3]$. The first, second, and third layers have 32, 64, and 96 convolution filters, respectively. The optimal filter size of $[3\times3]$ is chosen for all three convolution layers. The stride size= 1 is considered for the convolutional layers. The maximum pooling filter size of $[2\times2]$ and stride size=

2 without zero-padding is considered. Table 4.7 demonstrates that the proposed technique performs well when the fully connected layers contain 25344 and 128 neurons respectively. To prevent a possible overfitting problem, there is a Dropout layer (25% rate) after all pooling layers and a 50% rate between the FC2 and the OL. The network is trained with only 50 epochs. The Adam optimizer is used to obtain the best-learned weights. The mini-batch size is fixed at 40 for each training iteration. The initial learning rate is kept at 0.01 during training. The optimal training parameters computed for simulation are listed in Table 4.7 along with their values. In Table 4.7, CL is for Convolutional Layer, FC is for the Fully Connected Layer, PL is for Pooling Layer, and OL represents Output Layer.

TABLE 4.7: Training Parameters for DCNN Architecture

SN	Parameters	Values
1	No of CL	3
2	No of kernels in each CL	32, 64, 96
3	CL kernel size	[3×3] for all layers
4	Pooling filter size	[2×2] after all CL
5	Activation function	ReLU (after all CL)
6	No of FC layers	2
7	Neurons in FC layers	Layer 1 (25344)
		Layer 2 (128)
8	Dropout	25% after all PL
		50% between FC2 and OL
9	Batch size	40
10	Learning rate	0.01
11	Optimizer	Adam
12	Epochs	50

The training and validation accuracy plots are displayed in Fig. 4.4 for the trained DCNN architecture. Similarly, the plots for training and validation loss are also displayed in Fig. 4.5. The reason why validation data accuracy > training data accuracy is a situation that might be viewed as good is because hyper-parameters

may have been tuned pretty well in the training data, which would have eventually led to an improved prediction in the validation data.

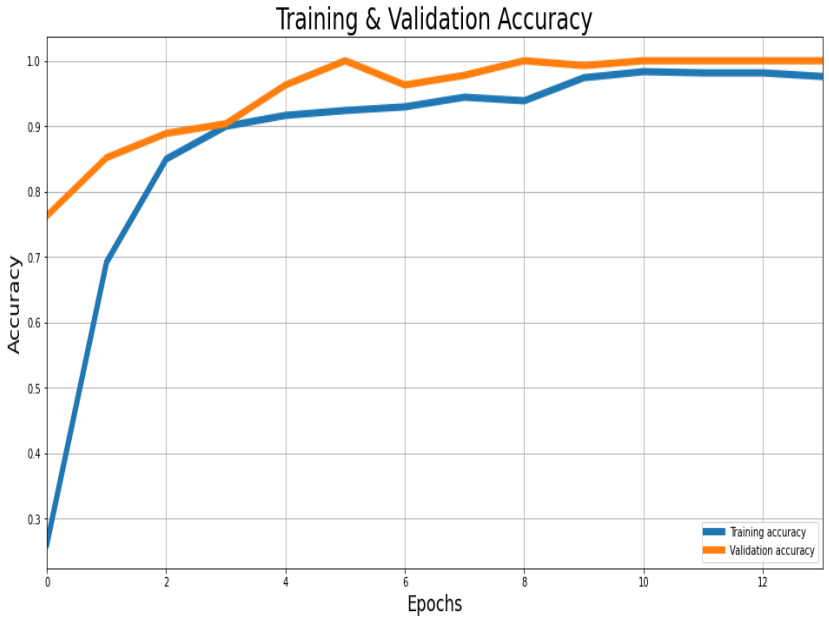

FIGURE 4.4: Training and Validation Accuracy of DCNN Architecture

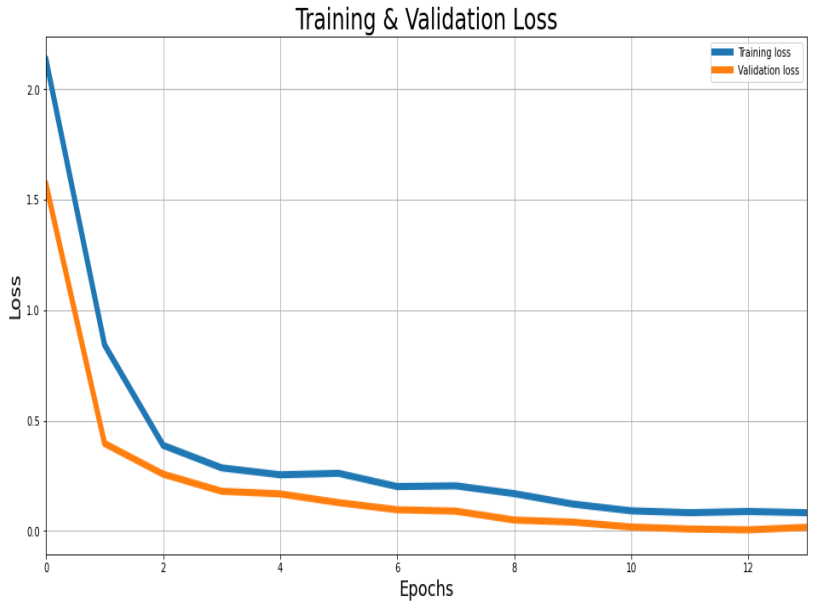

FIGURE 4.5: Training and Validation Loss of DCNN Architecture

The training and validation losses both converge to zero as the number of epochs increases. Similarly, with the increase in number of epochs, both the training and validation accuracies approach close to 100%.

4.2.3 Recognition Results

For the DCNN-based RER architecture, the recognition accuracies of all phases-coded waveforms are displayed in this subsection as a function of SNR. For SNR ranging from -16 dB to 8 dB, RER accuracies for six phase-coded signals are displayed in Table 4.8. A positive correlation can be seen between both variables, and each waveform has a distinct relation between SNR and recognition accuracy. After the simulations have been conducted at least ten times for each SNR value, the averaged accuracy values are given since the AWGN is added to the signals.

According to Table 4.8, the recognition rate of Barker codes is observed to be 88% at -16 dB and reaches 100% at -4 dB. Frank codes have 99% recognition accuracy at SNR of -16 dB and becomes 100% by SNR= -12 dB. P1 codes have an accuracy of 57%, which increases dramatically with the increase in SNR and becomes 100% at SNR= -8 dB as shown in Table 4.8, For all SNR values between -16 dB and 8 dB, P2 codes achieve a 100% recognition rate. P3 codes also have good recognition accuracies for all SNR values considered for the simulations. The suggested phase spectrum-based DCNN recognition is shown to be effective for P4 codes as 93% accuracy is observed at even low SNR of -16 dB and increases to 100% by -8 dB. The last row of Table 4.8 depicts the overall recognition accuracies of all phase-coded waveforms versus SNR.

The overall recognition rate for all phase-coded waveforms is also shown in Fig. 4.6 as a function of SNR. The recognition rate is 89% at SNR= -16 dB and rises until -8 dB. The fluctuations in SNR from -16 dB to -12 dB and from -12 dB to -8 dB sequentially result in an increase in recognition accuracy from 89% to 94.6% and ultimately reaches 99%. At even low SNR of -16 dB, a 89% recognition accuracy is achieved that shows the efficacy of proposed phase-based RER architecture using DCNN. The recognition accuracies of all phase coded waveforms are 100% at SNR$\geq$ -4 dB as shown in Table 4.8. The precision, recall, F1 score, and accuracy of phase coded waveforms are given at SNR values of -8 dB, -12 dB and -16 dB in the Table 4.9, 4.10, and 4.11, respectively.

TABLE 4.8: Recognition Accuracies Versus SNR

Signals	-16 dB	-12 dB	-8 dB	-4 dB	0 dB	4 dB	8 dB
Barker	88	93	97	100	100	100	100
Frank	99	100	100	100	100	100	100
P1	57	77	100	100	100	100	100
P2	100	100	100	100	100	100	100
P3	97	99	100	100	100	100	100
P4	93	99	100	100	100	100	100
Overall	89	94.6	99	100	100	100	100

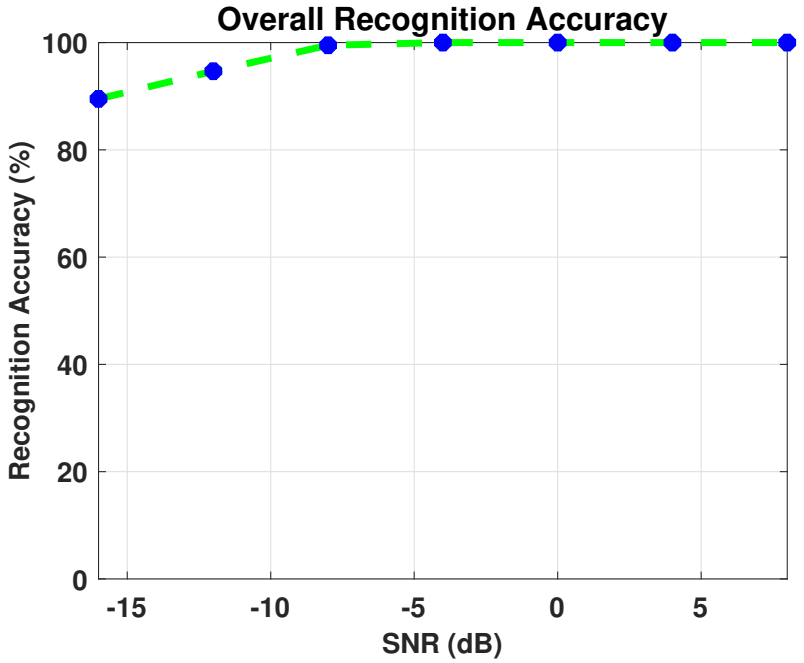

FIGURE 4.6: Overall Recognition Accuracies Versus SNR for DCNN Architecture

TABLE 4.9: Precision, Recall, F1 score, and Accuracy at SNR= -8 dB

Signals	Precision	Recall	F1 Score	Accuracy
Barker	100	97.5	98.7	97
Frank	100	100	100	100
P1	100	100	100	100
P2	100	100	100	100
P3	96.8	100	98.4	100
P4	100	100	100	100

TABLE 4.10: Precision, Recall, F1 score, and Accuracy at SNR= -12 dB

Signals	Precision	Recall	F1 Score	Accuracy
Barker	94.9	92.5	93.7	93
Frank	100	100	100	100
P1	88.5	76.7	82.1	77
P2	98.4	100	99.2	100
P3	96.7	98.9	97.8	99
P4	90.8	98.9	94.7	99

TABLE 4.11: Precision, Recall, F1 score, and Accuracy at SNR= -16 dB

Signals	Precision	Recall	F1 Score	Accuracy
Barker	98.1	87.9	92.7	88
Frank	97.3	99.4	98.4	99
P1	76.7	57.5	65.7	57
P2	100	100	100	100
P3	92.1	97.2	94.6	97
P4	76	93.3	83.8	93

4.3 Discussion and Comparison

The two RER methods discussed in this research effort are compared in this section to determine which is more efficient for recognizing phase-coded waveforms in low SNR environments.

4.3.1 Comparison of both RER Approaches

The proposed BiLSTM and DCNN-based emitter recognition approaches used in this research effort are compared in terms of the SNR requirements. The phase-based feature vector is extracted using STFT and directly fed into the BiLSTM for recognition in the first architecture [16]. However, in the second method [41], the phase spectrum of the phase-coded signal is transformed into an image and cropped before it is ultimately given at the input of DCNN architecture. The same dataset is utilized for both approaches by splitting it into test and training

datasets. In [41], very low SNR is considered ranging from -16 dB to 8 dB whereas, in [16] SNR ranges from -8 dB to 8 dB. The comparison is done for SNR values ranging from -8 dB to 8 dB. The recognition accuracies obtained by using both

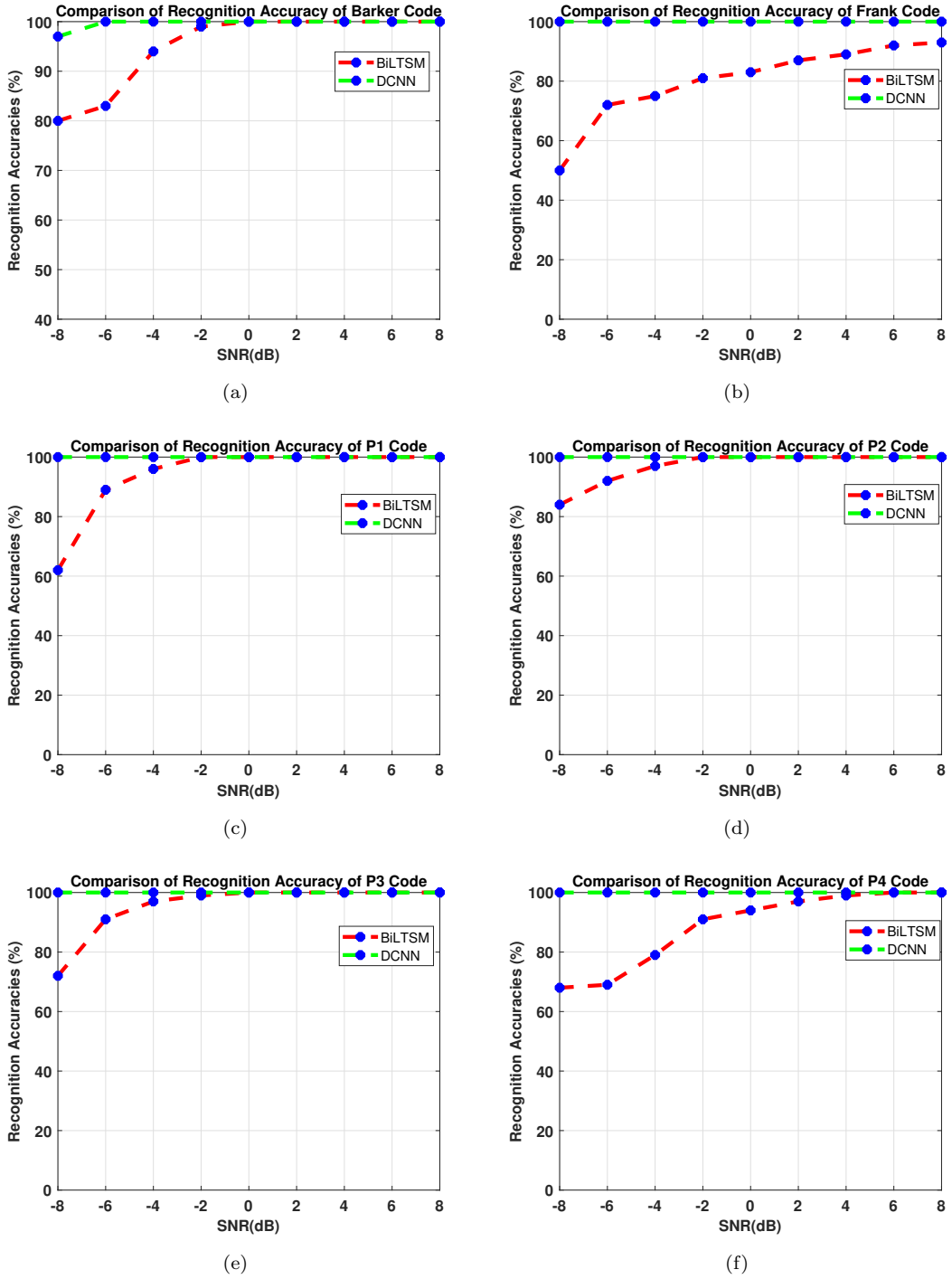

FIGURE 4.7: The Comparison of Recognition Accuracies of Phase coded Waveforms for BiLSTM and DCNN (a) Barker, (b) Frank, (c) P1, (d) P2, (e) P3, (f)P4

proposed architectures for all phase-coded waveforms are displayed in Fig. 4.7(a)

through Fig. 4.7(f). At -8 dB, the BiLSTM-based approach has 80% recognition accuracy for Barker codes as compared to DCNN architecture having 97% as shown in Fig. 4.7(a). The recognition accuracy for Barker code reaches 100% for DCNN at -6 dB whereas for BiLSTM it reaches 100% by -2 dB. The recognition accuracy achieved for Frank codes using the BiLSTM method is quite low as compared to the DCNN method and is shown in Fig. 4.7(b). The recognition rate of Frank codes using BiLSTM increases from 50% to 90% as the SNR varies from -8 dB to 4 dB. Similarly, from -4 dB to 8 dB, the recognition accuracy varies from 90% to 93%. For P1 codes, the recognition rate is 62% at -8 dB and increases significantly to 100% by -2 dB for the BiLSTM method whereas for DCNN its 100% for all SNR values as shown in Fig. 4.7(c). Similarly, in the case of P2 codes, the recognition rate varies from 84% to 100% as SNR varies from -8 dB to 8 dB using the BiLSTM technique whereas DCNN has 100% accuracy throughout even at low SNR of -8 dB. P3 codes have a recognition rate of 72% and increase significantly till it reaches 100% by -2 dB for the BiLSTM technique as compared to the DCNN method having 100% accuracy throughout all SNR values as depicted by Fig. 4.7(e). P4 codes have less recognition rate at low SNR values obtained from the BiLSTM approach as depicted by Fig. 4.7(f) but DCNN has 100% accuracy for all SNR values. The overall recognition accuracies of phase-coded signals are compared for both proposed architectures discussed in [16] and [41] as depicted by the Fig. 4.8.

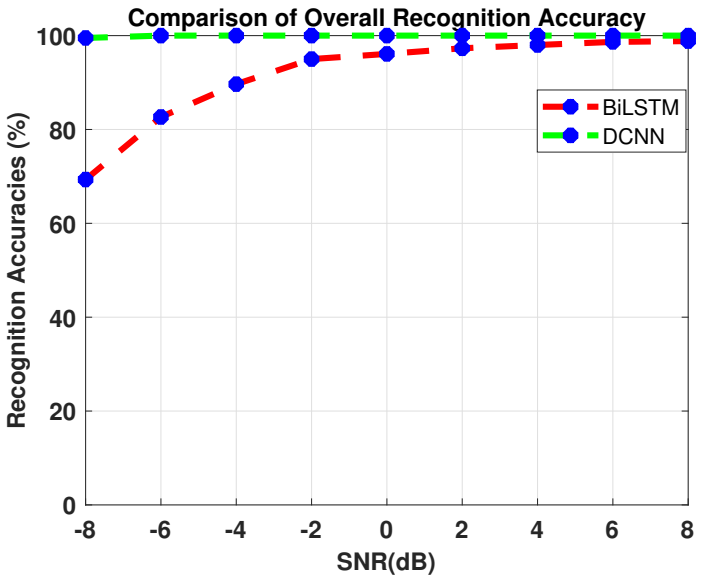

FIGURE 4.8: The Comparison of Overall Recognition Accuracies for BiLSTM and DCNN

In [41], 99.5% recognition rate is observed at -8 dB for DCNN architecture that reaches 100% by -6 dB and remains 100% for next SNR values till 8 dB. However, in the case of BiLSTM, the recognition rate starts from 69.33% and reaches 82.67% by -6 dB SNR, it then goes on increasing and ultimately reaches 100% by SNR=8 dB. Hence, the overall comparison depicts that DCNN-based architecture has outperformed the BiLSTM approach and very good recognition accuracies are observed even at very low SNR values.

4.3.2 Comparison of Proposed DCNN Architecture with Other Methods

The proposed RER methodology using DCNN is compared to other extensively used state-of-the-art methodologies published in the literature in this sub-section. The suggested strategy is compared to the other methods in [21, 30, 38, 102] in terms of the SNR requirements and recognition results for phase-coded waveforms are compared. The comparison of the proposed work with the existing works is not possible because the datasets used in the existing works are not easily accessible. Moreover, it is also difficult to run the existing methods on the dataset used in our approach as the information provided about them is not sufficient to reproduce such methods.

4.3.2.1 Comparison with [21]

In [21], an ABC technique is used to optimize SVM for detecting eight different types of radar waveforms. According to the simulation results, the total recognition rate is observed to be 92% when the SNR is -4 dB. The comparison of the two methods reveals that the recognition accuracy of phase-coded signals has improved when phase-based images are recognized using the DCNN architecture proposed in this study. Table 4.12 shows a comparison between the two recognition methods where all the phase-coded waveforms have 100% recognition accuracies even at low SNR= -4 dB. Moreover, Barker codes also have 100% recognition accuracy

obtained from our proposed architecture (DCNN) whereas they are not discussed in [21].

4.3.2.2 Comparison with [30]

A MFIJD model is described in [30]. It fully extracts the pixel feature to obtain the pre-classification results of each feature image for the non-stationary features of the majority of LPI radar signals. This model has two different feature extraction structures. The approach achieves a total recognition accuracy of 87.7% at an SNR of -6 dB. At SNR=0 dB, the confusion matrix is displayed separately for both structures. In comparison to [30], the total recognition accuracy of all phase-coded signals is seen to be 100% in our suggested approach as shown in Table 4.12.

4.3.2.3 Comparison with [102]

In [102], a Neural Architecture Search (NAS) algorithm is proposed to identify the best classifier of radar waveforms for the very first time, eliminating the dependency on transfer learning and achieving good generalization ability. The accuracy rate for 15 types of radar waveforms may reach 79.2% under the SNR= -9 dB. The simulations demonstrate that the model based on flexible differentiable architecture search has a better performance. According to recognition plots given in Fig. 14(a) through Fig. 14(f) in [102] at SNR= -6 dB, the recognition accuracy of BPSK/Barker codes is 100% whereas Frank, P2, and P3 codes have more than 95% recognition accuracies. P1 codes have 80% recognition accuracy as compared to P4 codes having the least accuracy of 78%. Whereas, all phase-coded waveforms, including Barker codes, have a recognition rate of 100% in our proposed DCNN-based architecture, confirming the effectiveness of our suggested architecture at an SNR of -6 dB. Table 4.13 gives the comparison of both techniques in tabular form. The comparison shows that our proposed method performs well as compared to other methods in [102] and [38].

4.3.2.4 Comparison with [38]

In [38], a novel strategy based on feature fusion and a dual-channel CNN for the LPI radar signal detection method is proposed. It consists of three main modules: the preprocessing module, the feature extraction module, and the recognition module. The CM plot is given in [38] at SNR= -6 dB. The comparison of both techniques is given in Table 4.13 which depicts that the recognition accuracy of P1 codes has improved to 100% in our research work as compared to 80% in this [38].

TABLE 4.12: Comparison of Radar Emitter Recognition Accuracy (RERA) with [21] and [30] at SNR of -4 dB and 0 dB respectively.

Phase Coding Types	[21] (-4 dB)	Proposed Method (-4 dB)	[30] (0 dB)	Proposed Method (0 dB)
Barker	Not given	100%	Not given	100%
Frank	85%	100%	Not given	100%
P1	84%	100%	96%	100%
P2	99%	100%	100%	100%
P3	84%	100%	100%	100%
P4	86%	100%	93%	100%

TABLE 4.13: Comparison of Radar Emitter Recognition Accuracy (RERA) with [102] and [38] at SNR of -6dB

Phase Coding Types	[102] (-6 dB)	Proposed Method (-6 dB)	[38] (-6 dB)	Proposed Method (-6 dB)
Barker	100%	100%	Not given	100%
Frank	99%	100%	Not given	100%
P1	80%	100%	80%	100%
P2	98%	100%	100%	100%
P3	99%	100%	100%	100%
P4	78%	100%	93%	100%

4.3.3 Computational Complexity

The computational complexity is computed for both the proposed architectures.

4.3.3.1 Computational Complexity of BISLTM

The computational complexity of the proposed BILSTM network can be calculated as:
Let, I=Input Nodes, H=Hidden Nodes, M=Output Nodes.

Forward Pass:

1. Time complexity for input-to-hidden computation in one time step: $O(H \times I)$.
2. Time complexity for hidden-to-hidden computation in one time step: $O(H^2)$.
3. Time complexity for hidden-to-output computation: $O(M \times H)$.
4. Total time complexity for one input sequence and T time steps in the forward pass: $T \times (H \times I + H^2 + M \times H)$.
5. Total time complexity for one mini-batch containing 306 input sequences : $1 \times T(H \times I + H^2 + M \times H)$.
6. Total time complexity for 2 mini-batches of 612 input sequences: $2 \times T \times (H \times I + H^2 + M \times H)$.

Backward Pass:

1. Time complexity for output-to-hidden computation: $O(H \times M)$.
2. Time complexity for hidden-to-hidden computation in one time step: $O(H^2)$.
3. Time complexity for hidden-to-input computation in one time step: $O(I \times H)$.

4. Total time complexity for one input sequence and T time steps in the backward pass: $T \times (H \times M + H^2 + I \times H)$.

5. Total time complexity for one mini-batch containing 306 input sequences: $1 \times T \times (H \times M + H^2 + I \times H)$.

6. Total time complexity for 2 mini-batches of 612 input sequences $2 \times T \times (H \times M + H^2 + I \times H)$.

7. Considering both the forward and backward passes: $4 \times T \times (H \times I + H^2 + M \times H)$.

8. Overall= $O(T \times H \times I + T \times H^2 + T \times M \times H)$.

4.3.3.2 Computational Complexity of DCNN

To compute the computational complexity of a DCNN model, we need to consider the operations performed in each layer and their relationship to the input size. Here's how we can calculate the complexity for the given model:

1. **Input Layer**

   The input shape is (46, 545, 3), so the total number of input units is $46 \times 545 \times 3 = 75210$.

2. **First Convolutional Layer**

   This layer has 32 filters of size $3 \times 3 \times 3$, so the number of parameters is $32 \times (3 \times 3 \times 3 + 1) = 896$. The output feature map size will be $(46 - 3 + 1) \times (545 - 3 + 1) \times 3 \times 32 = 44 \times 543 \times 3 \times 32$. Each output unit is computed by a dot product of a filter with the input image, resulting in $(32 \times 3 \times 3 \times 3 \times 44 \times 543) = 20,642,688$ multiplications and $(32 \times (3 \times 3 \times 3 + 1) \times 44 \times 543) = 21,407,232$ additions.

3. **ReLU Activation**

   ReLU operation does not change the computational complexity, as it only involves element-wise comparisons and assignments.

4. **First Max-pooling Layer**

   The filter size is 2×2 and the output feature map size will be $22 \times 271 \times 32$.

5. **Second Convolutional Layer**

   The layer has 64 filters of size $3 \times 3 \times 3$, similar to the first convolutional layer. The number of parameters is $64 \times (3 \times 3 \times 3 + 1) = 1792$. The output feature map size will be $(22 - 3 + 1) \times (271 - 3 + 1) \times 64 = 20 \times 269 \times 64$. The number of multiplications is $(64 \times 3 \times 3 \times 3 \times 20 \times 269) = 9,296,640$ and additions is $(64 \times (3 \times 3 \times 3 + 1) \times 20 \times 269) = 9,640,960$.

6. **ReLU Activation and Maxpooling Layer**

   Similar to previous layers, they do not change the computational complexity. The size of output after max-pooling will be $10 \times 134 \times 64$.

7. **Third Convolutional Layer**

   This layer has 96 filters of size $3 \times 3 \times 3$. The number of parameters is $96 \times (3 \times 3 \times 3 + 1) = 2688$. The output feature map size will be $(10 - 3 + 1) \times (134 - 3 + 1) \times 96 = 8 \times 132 \times 96$. The number of multiplications is $(96 \times 3 \times 3 \times 3 \times 8 \times 132) = 2,737,152$ and additions is $(96 \times (3 \times 3 \times 3 + 1) \times 8 \times 132) = 2,838,528$.

8. **ReLU Activation and Max-pooling Layer**

   These layers do not affect the computational complexity. The size of output after max-pooling will be $4 \times 66 \times 96$.

9. **Flatten Layer**

   The flatten layer does not involve any additional computations; it reshapes the input.

10. **Dense Layer**

    The number of parameters in this layer is $(n+1) \times 128$, where the "+1" is for the bias term. Assuming that the previous layer size is n. The computational complexity of a dense layer is typically considered to be proportional to the number of parameters, so the complexity here is $O(n \times 128)$.

11. **Dense Layer:**

    Similar to the previous dense layer, the number of parameters here is $(128 + 1) \times 6$. The complexity of this dense layer is $O(128 * 6)$.

12. **Sigmoid Activation**

    The sigmoid activation function is applied element-wise to the outputs of the previous layer and doesn't affect the computational complexity.

13. **Overall Complexity**

    To calculate the overall complexity, we need to consider the cumulative complexity of all the layers. Since each layer's complexity is determined by the number of parameters, we can approximate the overall complexity by summing up the number of parameters in all layers.

14. The overall complexity can be expressed as:
    $O(42,049,920 + 18,937,600 + 5,575,680 + n \times 128 + 128 \times 6)$.

4.4 Chapter Summary

This chapter contains the simulation findings for the two proposed phase spectrum-based emitter recognition architectures. The first section provides the simulation setup, optimal network parameters selected for the simulations, and CM plots displaying the phase-coded waveform recognition rates at various SNR levels. The ideal parameters used and the CM plots for the DCNN-based architecture are both included in the other section. Finally, in the last section, a comparison of the two suggested architectures is carried out to ascertain which approach is more efficient for phase spectrum-based feature extraction for the recognition of radar emitters. DCNN has achieved better recognition accuracies as compared to the BiLSTM approach hence, some comparison of the proposed DCNN method is performed with other techniques in the literature.

Chapter 5

Conclusion and Future Work

Section 5.1 of this chapter provides a brief summary of the dissertation. In Section 5.2, the conclusion is discussed followed by suggested future work based on the research work presented in the dissertation.

5.1 Summary of Dissertation

Chapter 1 covers the fundamentals of radar systems and their historical background. The classification of radar systems according to waveform types and functions is also discussed. The explanation of EW and its subcategories is followed by a discussion of LPI radar waveforms. The key contribution is highlighted at the chapter's end, along with an overview of the entire thesis.

In Chapter 2, a thorough review of the literature on RER methods is given before the comparison of TFRs that are used to transform 1D radar signals into a 2D format for phase-based feature extraction. Based on the extensive literature survey, the suitable TFR is chosen for our application. STFT is considered as it has fast implementations due to FFT. Additionally, many DL methods are compared using a variety of parameters to determine which is best for our simulations. A literature survey helps to create a gap analysis, which is then followed by a problem statement and dissertation contributions.

Chapter 3 starts with a basic notion of feature extraction, which is crucial for various ML models. The merits of the feature extraction method are discussed, and then a novel, STFT-based feature extraction method is proposed. Detailed steps of the proposed feature extraction technique (1D and 2D) are listed and the generated phase-based feature plots for various phase-coded waveforms at various SNR levels are also displayed. Along with a system description, a detailed overview of both phase-based emitter recognition architectures (BiLSTM and DCNN) is also included.

In Chapter 4, the simulation setup, optimal network parameters selected for the simulations, and recognition accuracies for phase coded signals are given at various SNR levels. The two techniques put forward in this research effort are compared at to decide which approach is more effective. A comparison of the two proposed emitter recognition architectures with other state-of-the-art techniques found in the literature is also performed.

5.2 Conclusion and Future Work

The overall dissertation is concluded as follows :

5.2.1 Conclusion

One of the key tasks performed by EW systems is the quick and efficient recognition of LPI radar waveforms. Automatic radar waveform recognition is a crucial survival skill for an intercept receiver (RWR) that identifies radar emitters and recognizes threats. Intercept receivers must have an automatic LPI radar waveform identification function that offers precise detection and recognition capabilities in order to detect the presence of LPI radar signals. A few LPI radar recognition approaches that use feature extraction and classification methods have been mentioned in the literature that extracts features from the intercepted signal and categorizes the signal utilizing the derived features. The recognition of

phase-coded waveforms at a low Signal-to-Noise ratio (SNR) and feature extraction is still challenging, despite the recent breakthrough of DNNs along with time frequency transforms for emitter recognition.

In order to recognize phase-coded waveforms with high recognition accuracies at low SNR levels, it is recommended to apply an AMCS technique based on the phase spectrum rather than the amplitude spectrum used in recent research studies. The simulation findings obtained for this research also depict that phase is a crucial parameter for the better identification of phase-coded waveforms. This research has investigated an AMCS approach for phase-coded waveforms based on the novel features derived from the phase spectrum of STFT. Six different types of noisy emitter signals including Barker, Frank, and Polyphase codes (P1-P4) intercepted at the RWR have been recognized. Since phase features can be expressed as a 1D vector or 2D matrix, both techniques (BiLSTM and CDNN) seem like good candidates for automatic modulation classification of phase-coded waveforms. They have been used to verify the effectiveness of a novel phase-based feature extraction method which is the major contribution of this research work.

The BiLSTM network receives the STFT-derived phase-based feature (1D) vectors directly at the input. There is no need for intricate pre-processing because the feature extraction is carried out on the phase-coded and modulated signals received at RWR. The efficacy of the proposed phase-spectrum based BiLSTM model has been investigated and simulations are performed using a simulated dataset with waveforms having SNR ranging from -8 dB to 8 dB. The CM plots are presented to judge the performance of the newly proposed phase-based feature vector at different SNR values. The suggested method is competitive with other methods mentioned in the literature in terms of SNR and requires no pre-processing, which makes it attractive for applications requiring quick and efficient online recognition of phase-coded waveforms. The proposed method works effectively well in practice, achieving 70% overall identification accuracy at an SNR of -8 dB.

The STFT-derived phase-based images (2D) are cropped and fed to the DCNN network for recognition. The DCNN-based recognition system has performed very

well in contrast to BiLSTM on the same dataset and the following are the details: It has high recognition accuracies even at a low SNR value of -16 dB. The overall recognition rate is 89% when SNR is as low as -16 dB. Secondly, it has a low level of computational complexity when compared to recent approaches discussed in the literature in terms of SNR requirements. The simulations take far less time to complete as no complex pre-processing is there. Additionally, it is found that Barker codes, even at low SNR levels, have acceptable recognition accuracy when utilizing both approaches; yet, they are rarely discussed in the literature. In a nutshell, it has been concluded that the proposed phase spectrum-based automatic modulation recognition approaches using the newly proposed feature extraction method have outperformed the other notable techniques in the literature attaining high recognition accuracies for phase-coded waveforms at low SNR environments while also requiring less pre-processing.

5.2.2 Future Work

The research findings presented in this thesis can be extended in the following ways as future work.

1. **Recognition of Phase-Coded Waveforms at different Carrier Frequency (Fc)**

   The proposed AMCSs pave the way for the development of cutting-edge emitter recognition methods that will produce high recognition accuracies in extremely low SNR environments. For simplicity, the carrier frequency in this research work has been assumed to be the same for all intercepted phase-coded waveforms. Therefore, it is recommended that this research may be expanded to detect various phase-coded waveforms with different carrier frequencies to realize more realistic EW scenarios.

2. **Denoising**

   The process of de-noising an image has become vital to image pre-processing. Its purpose is to reduce background noise and highlight the unique image

data that is stored inside it. In the field of image processing and computer vision, the issue of image denoising poses a very fundamental challenge. Therefore, it has a significant impact in a variety of fields where retrieving the original image is crucial for reliable performance. The identification accuracies of phase-coded waveforms simulated in this research can be improved further even in low SNR environments by adding a denoising method in the image pre-processing step which appears to be an appealing future work.

3. **Recognition of Poly-time Codes along with Phase-Coded Waveforms**

   The proposed research includes the recognition of polyphase-coded signals that are mostly used by LPI radars to prevent them from being intercepted at RWRs. In order to evaluate the effectiveness of suggested algorithms, this research effort might be broadened by using poly-time codes in addition to Barker and polyphase codes.

4. **Recognition of Overlapping or mixed phase coded waveforms**

   The development of AMCS that can identify various phase-coded waveforms that have been mixed or overlapped can be accomplished through the extension of this research. In an electromagnetic environment that is growing more and more complex, many LPI radar emitters may simultaneously transmit distinct signals on similar bands, causing receiving signals to overlap in both the time domain and the frequency domain. Recognizing the various modulation patterns of these signals is crucial if we intend to recover the original signals while preserving useful information.

5. **Object Detection**

   Future research may incorporate objection detection as a fundamental part of the proposed phase-based feature extraction method in replacement of the recognition problem, where the Fc of the signal is determined to estimate the optimal window size for STFT. In order to achieve a more realistic radar

environment, it will also be useful when the various phase-coded waveforms are at distinct carrier frequencies.

6. **Recognition of Unknown Number of Radar Signals**

   Future research can assess how well advanced deep learning techniques perform when determining the modulation schemes of an unknown number of radar signals in a more realistic situation. This problem appears to be challenging when there are few samples available and in an environment with poor SNR.

Bibliography

[1] M. I. Skolnik, B. Guatemala, H. Lisbon, L. Madrid, M. New, D. Panama, P. San, P. Singapore, S. Tokyo, B. Guatemala, and J. Sao, *Introduction to Radar Systems*. McGraw-Hill Education, 2nd ed., 1980.

[2] R. Casale, "The life of nikola tesla." [Accessed: June 28, 2022].

[3] N. Science, "Tour of the electromagnetic spectrum." [Accessed: June 22, 2022].

[4] N. Science, "History of radar." [Accessed: May 15, 2022].

[5] R. C. W. Jr, *Radar Origins Worldwide: History of Its Evolution in 13 Nations Through World War II*. Trafford Publishing, 1st ed., 2009.

[6] Wikipedia, "History of radar." [Accessed: Sep 16, 2022].

[7] W. F. Althoff, *Sky Ships: A History of the Airship in the United States Navy*. Naval Institute Press, 2016.

[8] M. Vance, "What is ground penetrating radar?." [Accessed: May 28, 2020].

[9] D. Cooper, "Multiple target tracking with radar applications," *Electronics and Power*, vol. 33, no. 6, pp. 407–416, 1987.

[10] D. Adamy, *EW 101: A first course in electronic warfare*. Artech house, 1st ed., 2001.

[11] H. H. Griffiths, C. Baker, D. Adamy, and G. W. Stimson, *Stimson's introduction to airborne radar*. The Institution of Engineering and Technology, 3rd ed., 2014.

[12] P. E. Pace, *Detecting and Classifying Low Probability of Intercept Radar Second Edition.* Artech house, 2nd ed., 2009.

[13] N. Levanon and E. Mozeson, *Radar signals.* John Wiley Sons, 2004.

[14] H. Hassan, "A new algorithm for radar emitter recognition," in *3rd International Symposium on Image and Signal Processing and Analysis, ISPA 2003*, vol. 2, pp. 1097–1101.

[15] G. Zhang, "Intra-pulse modulation recognition of advanced radar emitter signals using intelligent recognition method," in *International Conference on Rough Sets and Knowledge Technology, 2006*, pp. 707–712.

[16] S. G. Bhatti and A. I. Bhatti, "Radar signals intrapulse modulation recognition using phase-based STFT and BiLSTM," *IEEE Access*, vol. 10, pp. 80184–80194, 2022.

[17] B. Wu, S. Yuan, P. Li, Z. Jing, S. Huang, and Y. Zhao, "Radar emitter signal recognition based on one-dimensional Convolutional Neural Network with attention mechanism," *Sensors (Basel, Switzerland)*, vol. 20, pp. 1–13, 11 2020.

[18] J. Wang, X. Wang, Y. Tian, Z. Chen, and Y. Chen, "A radar emitter recognition mechanism based on Ifs-Tri-Training Classification processing," *Electronics*, vol. 11, p. 1078, 3 2022.

[19] T. R. Kishore and K. D. Rao, "Automatic intrapulse modulation classification of advanced LPI radar waveforms," *IEEE Transactions on Aerospace and Electronic Systems*, vol. 53, pp. 901–914, 4 2017.

[20] M. Zhang, M. Diao, L. Gao, and L. Liu, "Neural networks for radar waveform recognition," *Symmetry*, vol. 9, no. 5, p. 75, 2017.

[21] L. Liu, S. Wang, and Z. Zhao, "Radar waveform recognition based on time-frequency analysis and Artificial Bee Colony-Support Vector Machine," *Electronics*, vol. 7, p. 59, 4 2018.

[22] X. Wang, G. Huang, Z. Zhou, W. Tian, J. Yao, and J. Gao, "Radar emitter recognition based on the energy cumulant of Short Time Fourier Transform and Reinforced Deep Belief Network," *Sensors*, vol. 18, no. 9, p. 3103, 2018.

[23] S. H. Kong, M. Kim, L. M. Hoang, and E. Kim, "Automatic LPI radar waveform recognition using CNN," *IEEE Access*, vol. 6, pp. 4207–4219, 12 2017.

[24] Z. M. Liu and P. S. Yu, "Classification, Denoising, and De-interleaving of pulse streams with Recurrent Neural Networks," *IEEE Transactions on Aerospace and Electronic Systems*, vol. 55, pp. 1624–1639, 8 2019.

[25] T. Alrubeaan, K. Albagami, A. Ragheb, S. Aldosari, M. Altamimi, and S. Alshebeili, "An investigation of LPI radar waveforms classification in ROF channels," *IEEE Access*, vol. 7, pp. 124844–124853, 2019.

[26] G. Kong and V. Koivunen, "Radar waveform recognition using Fourier-Based Synchrosqueezing Transform and CNN," *IEEE 8th International Workshop on Computational Advances in Multi-Sensor Adaptive Processing, CAMSAP 2019 - Proceedings*, pp. 664–668.

[27] S. Wei, Q. Qu, H. Su, M. Wang, J. Shi, and X. Hao, "Intra-pulse modulation radar signal recognition based on CLDN network," *IET Radar, Sonar Navigation*, vol. 14, pp. 803–810, 6 2020.

[28] X. Wang, G. Huang, C. Ma, W. Tian, and J. Gao, "Convolutional Neural Network applied to specific emitter identification based on pulse waveform images," *IET Radar, Sonar Navigation*, vol. 14, pp. 728–735, 5 2020.

[29] R. Guoqing, Y. Wang, S. Wang, Y. Zheng, Q. Guo, and S. Shulga, "Automatic recognition of radar signal types based on cnn-lstm," *Telecommunications and Radio Engineering*, vol. 79, pp. 305–321, 01 2020.

[30] Z. Ma, Z. Huang, A. Lin, and G. Huang, "Lpi radar waveform recognition based on features from multiple images," *Sensors 2020, Vol. 20, Page 526*, vol. 20, p. 526, 1 2020.

[31] S. H. Kim, J. W. Kim, V. S. Doan, and D. S. Kim, "Lightweight deep learning model for automatic modulation classification in cognitive radio networks," *IEEE Access*, vol. 8, pp. 197532–197541, 2020.

[32] K. Chen, S. Zhang, L. Zhu, S. Chen, and H. Zhao, "Modulation recognition of radar signals based on adaptive singular value reconstruction and deep residual learning," *Sensors (Switzerland)*, vol. 21, pp. 1–18, 1 2021.

[33] S. Yuan, B. Wu, and P. Li, "Intra-pulse modulation classification of radar emitter signals based on a 1-d selective kernel Convolutional Neural Network," *Remote Sensing*, vol. 13, p. 2799, 7 2021.

[34] S. Zhang, J. Pan, Z. Han, and L. Guo, "Recognition of noisy radar emitter signals using a one-dimensional deep residual shrinkage network," *Sensors (Basel, Switzerland)*, vol. 21, 12 2021.

[35] X. Zhang, J. Zhang, T. Luo, T. Huang, Z. Tang, Y. Chen, J. Li, and D. Luo, "Radar signal intrapulse modulation recognition based on a Denoising-Guided Disentangled Network," *Remote Sensing*, vol. 14, p. 1252, 3 2022.

[36] Z. Jing, P. Li, B. Wu, S. Yuan, and Y. Chen, "An adaptive focal loss function based on transfer learning for Few-Shot radar signal Intra-pulse modulation classification," *Remote Sensing*, vol. 14, p. 1250, 4 2022.

[37] S. Yuan, P. Li, B. Wu, X. Li, and J. Wang, "Semi-supervised classification for intra-pulse modulation of radar emitter signals using Convolutional Neural Network," *Remote Sensing*, vol. 14, 5 2022.

[38] D. Quan, Z. Tang, X. Wang, W. Zhai, and C. Qu, "Lpi radar signal recognition based on Dual-Channel CNN and feature fusion," *Symmetry*, vol. 14, p. 570, 3 2022.

[39] S. Wei, Q. Qu, X. Zeng, J. Liang, J. Shi, and X. Zhang, "Self-attention BiLSTM networks for radar signal modulation recognition," *IEEE Transactions on Microwave Theory and Techniques*, vol. 69, pp. 5160–5172, 11 2021.

[40] S. G. Bhatti and A. I. Bhatti, "Adaptive measurement noise covariance matrix r for JPDAF based Multitarget tracking," *1st International Conference on Electrical, Communication and Computer Engineering, ICECCE 2019*, 7 2019.

[41] S. G. Bhatti and A. I. Bhatti, "Phase-based intrapulse modulation recognition of radar waveforms," *Journal of Signal Processing Systems (Submitted).*

[42] R. Vellanki, "Modeling and analysis of LPI radar signal," *IOSR Journal of Electronics and Communication Engineering*, vol. 8, pp. 19–26, 2013.

[43] R. Tian, G. Zhang, R. Zhou, and W. Dong, "Detection of Polyphase codes radar signals in low SNR," *Mathematical Problems in Engineering*, vol. 3, p. 3253, 2016.

[44] C. Y. Mei, A. Z. Sha'ameri, and B. Boashash, "Efficient phase estimation for the classification of digitally phase modulated signals using the cross-WVD: A performance evaluation and comparison with the S-transform," *Eurasip Journal on Advances in Signal Processing*, vol. 5, p. 5123, 2012.

[45] M. Shyamsunder and K. S. Rao, "Time frequency analysis of LPI radar signals using modified S transform," *International Journal of Electronics Engineering Research*, vol. 9, pp. 1267–1283, 2017.

[46] L. B. Yang, S. S. Zhang, and B. Xiao, "Radar emitter signal recognition based on time-frequency analysis," *IET Conference Publications, 2013*, p. 676.

[47] Z. Liu, Y. Shi, Y. Zeng, and Y. Gong, "Radar emitter signal detection with Convolutional Neural Network," *IEEE 11th International Conference on Advanced Infocomm Technology, ICAIT 2019*, pp. 48–51.

[48] C. Wang, J. Wang, and X. Zhang, "Automatic radar waveform recognition based on time-frequency analysis and Convolutional Neural Network," *ICASSP, IEEE International Conference on Acoustics, Speech and Signal Processing, 6 2017*, pp. 2437–2441.

[49] M. Zhu, X. Zhang, Y. Qi, and H. Ji, "Compressed sensing mask feature in Time-Frequency domain for civil flight radar emitter recognition," *ICASSP, IEEE International Conference on Acoustics, Speech and Signal Processing, 4 2018*, pp. 2146–2150.

[50] M. Zhu, Z. Feng, X. Zhou, R. Xiao, Y. Qi, and X. Zhang, "Specific emitter identification based on Synchrosqueezing Transform for civil radar," *Electronics*, vol. 9, p. 658, 4 2020.

[51] Z. Yang, W. Qiu, H. Sun, and A. Nallanathan, "Robust radar emitter recognition based on the three-dimensional distribution feature and Transfer Learning," *Sensors*, vol. 16, p. 289, 2 2016.

[52] K. Li, "Radar emitter identification based on improved convolutional neural network," *Proceedings of 2019 IEEE 3rd Advanced Information Management, Communicates, Electronic and Automation Control Conference, IMCEC 2019*, pp. 118–121.

[53] A. Kawalec and R. Owczarek, "Radar emitter recognition using intrapulse data," *15th International Conference on Microwaves, Radar and Wireless Communications, MIKON 2004*, pp. 435–438.

[54] R. Mingqiu, C. Jinyan, and Z. Yuanqing, "Classification of radar signals using time-frequency transforms and fuzzy clustering," *2010 International Conference on Microwave and Millimeter Wave Technology, ICMMT 2010*, pp. 2067–2070.

[55] A. Madhu, P. Prajeesha, and A. S. Kulkarni, "Radar emitter identification using signal noise and power spectrum analysis in deep learning," in *2022 Fifth International Conference of Women in Data Science at Prince Sultan University (WiDS PSU)*, pp. 52–57, IEEE, 2022.

[56] K. Chen, J. Zhang, S. Chen, S. Zhang, and H. Zhao, "Automatic modulation classification of radar signals utilizing x-net," *Digital Signal Processing*, vol. 123, p. 103396, 2022.

[57] P. He, Y. Zhang, X. Yang, X. Xiao, H. Wang, and R. Zhang, "Deep learning-based modulation recognition for low signal-to-noise ratio environments," *Electronics*, vol. 11, no. 23, p. 4026, 2022.

[58] J. Nussbaumer Henri, "Fast Fourier Transform and Convolution algorithms," 1982.

[59] Y. Hong-hai, Y. Xiao-peng, L. Shao-kun, L. Ping, and H. Xin-hong, "Radar emitter multi-label recognition based on residual network," *Defence Technology*, vol. 18, pp. 410–417, 3 2022.

[60] M. Kong, J. Zhang, W. Liu, and G. Zhang, "Radar emitter identification based on deep Convolutional Neural Network," *7th International Conference on Control, Automation and Information Sciences, ICCAIS, 12 2018*, pp. 309–314.

[61] A. Gupta and A. A. B. Rai, "Feature extraction of Intra-Pulse Modulated LPI Waveforms Using STFT," *4th IEEE International Conference on Recent Trends on Electronics, Information, Communication and Technology, RTEICT 2019*, pp. 742–746.

[62] S. V. Bozhokin and I. M. Sokolov, "Comparison of the Wavelet and Gabor Transforms in the Spectral Analysis of Non-Stationary Signals," *Technical Physics*, vol. 63, pp. 1711–1717, 12 2018.

[63] D. A. Andreev, S. V. Bozhokin, I. D. Venevtsev, and K. T. Zhunusov, "Gabor transform and Continuous Wavelet transform for model pulsed signals," *Technical Physics*, vol. 59, pp. 1428–1433, 10 2014.

[64] S. Scholl, "Fourier, Gabor, Morlet or Wigner: Comparison of Time-Frequency Transforms," *arXiv preprint arXiv:2101.06707*, 1 2021.

[65] I. Shafi, J. Ahmad, S. I. Shah, and F. M. Kashif, "Techniques to obtain good resolution and concentrated Time-Frequency Distributions: A Review," *EURASIP Journal on Advances in Signal Processing*, vol. 2009, pp. 1–43, 6 2009.

[66] M. Szmajda, K. Górecki, and J. Mroczka, "Gabor transform, SPWVD, Gabor-Wigner transform and Wavelet Transform - Tools for power quality monitoring," *Metrology and Measurement Systems*, vol. 17, p. 6, 2010.

[67] S. H. Cho, G. Jang, and S. H. Kwon, "Time-frequency analysis of power-quality disturbances via the Gabor-Wigner transform," *IEEE Transactions on Power Delivery*, vol. 25, pp. 494–499, 1 2010.

[68] D. H. Bailey and P. N. Swarztrauber, "The Fractional Fourier Transform and applications," *SIAM review*, vol. 33, no. 3, pp. 389–404, 1991.

[69] H. Zhu, "A Brief Overview of the S-transforms (Signal analysis and time-frequency analysis," *Interiors*, vol. 103, pp. 329–336, 2018.

[70] P. T. Krishnan and P. Balasubramanian *IEEE International Conference on Computational Intelligence and Computing Research, ICCIC 2016*, pp. 380–384.

[71] B. Liu, Y. Feng, Z. Yin, and X. Fan, "Radar Signal Emitter Recognition Based on Combined Ensemble Empirical Mode Decomposition and the Generalized S-Transform," *Mathematical Problems in Engineering*, vol. 5, p. 2346, 2019.

[72] N. E. Huang, *Hilbert-Huang transform and its applications*. World Scientific, 2nd ed., 2014.

[73] Y. Ji and H. Wang, "A Revised Hilbert–Huang Transform and its application to Fault Diagnosis in a Rotor System," *Sensors*, vol. 18, p. 4329, 12 2018.

[74] M. Zhang, M. Diao, and L. Guo, "Convolutional Neural Networks for Automatic Cognitive Radio Waveform Recognition," *IEEE Access*, vol. 5, pp. 11074–11082, 6 2017.

[75] W. Gongming, C. Shiwen, H. Xueruobai, and Y. Junjian, "Radar emitter sorting and recognition based on time-frequency image union feature," *IEEE 4th International Conference on Signal and Image Processing, ICSIP 2019*, pp. 165–170, 7.

[76] Y. Liu, P. Xiao, H. Wu, and W. Xiao, "LPI radar signal detection based on radial integration of Choi-Williams time-frequency image," *Journal of Systems Engineering and Electronics*, vol. 26, pp. 973–981, 10 2015.

[77] F. Auger, P. Flandrin, Y. T. Lin, S. McLaughlin, S. Meignen, T. Oberlin, and H. T. Wu, "Time-frequency Reassignment and Synchrosqueezing: An overview," *IEEE Signal Processing Magazine*, vol. 30, pp. 32–41, 2013.

[78] H. Jiang, K. Zhan, and L. Xu, "Joint tracking and classification with constraints and Reassignment by radar and ESM," *Digital Signal Processing*, vol. 40, pp. 213–223, 5 2015.

[79] D. L. Stevens, "Detection and Parameter Extraction of Low Probability of Intercept Radar Signals Using the Reassignment Method and the Hough Transform," Ph.D. dissertation, 2010.

[80] A. Roy, N. Gale, and L. Hong, "Automated traffic surveillance using fusion of Doppler radar and video information," *Mathematical and Computer Modelling*, vol. 54, pp. 531–543, 7 2011.

[81] L. Li, H. Cai, H. Han, Q. Jiang, and H. Ji, "Adaptive Short-Time Fourier Transform and Synchrosqueezing Transform for non-stationary signal separation," *Signal Processing*, vol. 166, p. 107231, 1 2020.

[82] M. Zhu, Z. Feng, and X. Zhou, "A novel data-driven specific emitter identification feature based on Machine Cognition," *Electronics*, vol. 9, p. 1308, 8 2020.

[83] K. Abratkiewicz and P. Samczyński, "Radar Pulse Signal Filtering Using Vertical Synchrosqueezing," in *2022 IEEE Radar Conference (RadarConf22) 2022*, pp. 1–6.

[84] N. U. Nathaniel, E. C. Ashigwuike, A. U. Sadiq, and N. A. Obadiah, "Modeling, Simulation and Analysis of Automotive radar signal using Wavelet Transform Technique," *15th International Conference on Electronics, Computer and Computation, ICECCO,12 2019*, pp. 125–129.

[85] P. Lang, X. Fu, M. Martorella, J. Dong, R. Qin, X. Meng, and M. Xie, "A comprehensive survey of machine learning applied to radar signal processing," *arXiv preprint arXiv:2009.13702*, 2020.

[86] B. S. Journal, "How Artificial Neural Networks work, from the math up." [Accessed: June 25, 2022].

[87] W. Hongmei and L. Pengzhong, "Image recognition based on improved Convolutional Deep Belief Network model," *Multimedia Tools and Applications*, vol. 80, pp. 2031–2045, 1 2021.

[88] M. Ramasubramanian, C. Banerjee, D. Roy, E. Pasiliao, and T. Mukherjee, "Exploiting Spatio-Temporal Properties of I/Q Signal Data Using 3D Convolution for RF Transmitter Identification," *IEEE Journal of Radio Frequency Identification*, vol. 5, pp. 113–127, 6 2021.

[89] P. Ratan, "Convolutional Neural Network Architecture." [Accessed: Aug 25, 2022].

[90] M. Du, X. He, X. Cai, and D. Bi, "Balanced Neural Architecture Search and Its Application in Specific Emitter Identification," *IEEE Transactions on Signal Processing*, vol. 69, pp. 5051–5065, 2021.

[91] A. Biswal, "Recurrent neural network (rnn) tutorial: Types and examples [updated]." [Accessed: Dec 15, 2022].

[92] B. He and F. Wang, "Cooperative Specific Emitter Identification via Multiple Distorted Receivers," *IEEE Transactions on Information Forensics and Security*, vol. 15, pp. 3791–3806, 2020.

[93] "An Overview on Long Short Term Memory (LSTM) - Analytics Vidhya." [Accessed: Sep 16, 2022].

[94] J. Zhu, Y. Zhao, and J. Tang, "Automatic recognition of radar signals based on time-frequency image character," *IET Conference Publications*, pp. 105–109, 2013.

[95] I. Guyon and A. Elisseeff, "An introduction to feature extraction," in *Feature extraction*, pp. 1–25, Springer, 2006.

[96] I. Guyon, S. Gunn, M. Nikravesh, and L. A. Zadeh, *Feature extraction: Foundations and Applications*, vol. 207. Springer, 2008.

[97] L. Durak and O. Arikan, "Short-Time Fourier Transform: Two fundamental properties and an Optimal implementation," *IEEE Transactions on Signal Processing*, vol. 51, pp. 1231–1242, 2003.

[98] R. Tao, Y. L. Li, and Y. Wang, "Short-time fractional fourier transform and its applications," *IEEE Transactions on Signal Processing*, vol. 58, pp. 2568–2580, 5 2010.

[99] S. Hochreiter and J. Schmidhuber, "Long Short-Term Memory," *Neural Computation*, vol. 9, pp. 1735–1780, 11 1997.

[100] D. T. Learning, "BiLSTM Explained." [Accessed: Feb 26, 2023].

[101] Z. Qu, X. Mao, and Z. Deng, "Radar Signal Intra-Pulse Modulation Recognition Based on Convolutional Neural Network," *IEEE Access*, vol. 6, pp. 43874–43884, 8 2018.

[102] Z. Ma, W. Yu, P. Zhang, Z. Huang, A. Lin, and Y. Xia, "LPI Radar Waveform Recognition Based on Neural Architecture Search," *Computational Intelligence and Neuroscience*, vol. 4, p. 4235, 2022.